Title
Ultrafast Nonlinear Spectroscopy Study of Interfaces and Surfaces

Author
Li, Yingmin

Publication Date
2019

UNIVERSITY OF CALIFORNIA SAN DIEGO

Ultrafast Nonlinear Spectroscopy Study of Interfaces and Surfaces

A dissertation submitted in partial satisfaction of the requirements for the

degree Doctor of Philosophy

in

Materials Science and Engineering

by

Yingmin Li

Committee in charge:

Professor Wei Xiong, Chair
Professor Vicki Helene Grassian
Professor Andrew C. Kummel
Professor Ying Shirley Meng
Professor Francesco Paesani

2019

This dissertation of Yingmin Li is approved, and it is acceptable in quality and form for publication on microfilm and electronically:

Chair

University of California San Diego

2019

DEDICATION

To my family, especially to my grandfather.

Yingmin Li

TABLE OF CONTENTS

LIST OF FIGURES

LIST OF TABLES

ACKNOWLEDGEMENTS

Firstly, I would like to thank my academic advisor, Prof. Wei Xiong, for giving me this great opportunity to work with lasers and ultrafast spectroscopy. He offered me continuous help in forming good research habits and establishing scientific methodologies. He sets me an excellent example of being an enthusiastic researcher, supportive mentor and knowledgeable scholar which would benefit me not only for my PhD work, but also for my future career.

I also would like to acknowledge my thesis committee: Prof. Vicki Grassian, Prof. Shirley Meng, Prof. Francesco Paesani, and Prof. Andrew Kummel, for their insightful comments, encouragement and hard questions along my PhD career. I had many great discussions with Prof. Vicki Grassian and Prof. Francesco Paesani on our collaborative projects. I really appreciate their guidance and suggestions for my research.

It is my great pleasure to have the opportunity to work on multiple collaborations which help me to broaden my experimental skills and expand my knowledge in different research field. I want to thank Dr. Huy Pham and Dr. Ongun Ozcelik from Prof. Francesco Paesani's group for their help on theoretical calculations. I learned the simulation principles from those wonderful theorists which I didn't familiar with as an experimentalist. Our collaboration led to the successful publication on charge dynamics of P3HT/metal interfaces.

I should also thank Dr. Mona Shrestha and Man Luo from Prof. Vicki Grassian's group for their support on our great collaborations on understanding proteins at air/aqueous interface. The projects couldn't be finished without their intelligent help and hard works.

My sincere thanks also go to Dr. Shen Wang from Prof. Shirley Meng's group. I couldn't forget the great discussions we had and how much I learned from him about nano characterization. Shen, as an expert in perovskite solar cells, gave me a lot of insightful suggestions regarding our charge transfer project. I will remember the efforts we spent on optimizing perovskite samples.

Our collaboration with Prof. Zhaowei Liu's group on characterizing the pulse limiter turned out to be very successful. I would like to thank Dr. Haoliang Qian who's an expert on nanofabrication and photonics.

I would like to thank all the members in the Xiong group, especially Bo Xiang, Jiaxi Wang, Haoyuan Wang, Wenfan Chen, and Jackson Wagner for all the discussions we had on science. They also created a competitive yet pleasant working environment, which makes the laser dark room not hard to stay in. At last, I would like to give my special thanks to my family: my father, Yalin Li, my mother, Guizhi Sun and my wife, Ran Wei for being so supportive throughout my whole PhD career. I couldn't have achieved as much without my wonderful family. It has been a wonderful journey for me to complete the challenging but exciting projects. I will remember what I learned from UC San Diego.

This research is founded by the University of California, San Diego start-up founding, a Defense Advanced Research Projects Agency grant (government grant number D15AP000107), an AFSOR grant (FA9550-13-1-0020), a National Science Foundation grant through the Centers of Chemical Innovation Pragram (CHE1305427), a National Science Foundation grant (CHE-1808111), two U. S. Department of Energy Grants under Office of Science (DE-FG02-13ER16387 and DEAC02-05CH11231).

Chapter 3, in part, is a reprint of the material as it appears in Yingmin Li, Jiaxi Wang, Wei Xiong. *"Probing Electronic Structures of Organic Semiconductors at Buried Interfaces by Electronic Sum Frequency Generation Spectroscopy".* The Journal of Physical Chemistry C, 119(50), 28083-28089. The dissertation author is the first author of this work.

Chapter 4, in part, is a reprint of the material as it appears in Bo Xiang,* Yingmin Li,* C. Huy Pham, Francesco Paesani, Wei Xiong. "*Ultrafast direct electron transfer at organic semiconductor and metal interfaces*". Science advances, 3(11), e1701508. The dissertation author is the co-first author of this work.

Chapter 5, in part, is a reprint of the material as it appears in Yingmin Li, Bo Xiang, Wei Xiong. "*Heterodyne Transient Vibrational SFG to Reveal Molecular Responses to Interfacial Charge Transfer*". The Journal of chemical physics, 150(11), 114706. The dissertation author is the first author of this work.

Chapter 6, in part, is a reprint of the material as it appears in Yingmin Li, Jiaxi Wang, Melissa L. Clark, Clifford P. Kubiak, Wei Xiong. "*Characterizing Interstate Vibrational Coherent Dynamics of Surface Adsorbed Catalysts by Fourth-order 3D SFG Spectroscopy*". Chemical Physics Letters, 650, 1-6. The dissertation author is the first author of this work.

Chapter 7, in part, is being prepared for publication of the materials. Yingmin Li, Mona Shrestha, Man Luo, Meishi Song, Vicki Grassian, Wei Xiong will be the coauthors. The dissertation author is the first author of this work.

VITA

2013 ***Bachelor of Engineering*****,** Materials Science and Engineering, Shandong University, China

2014 ***Master of Science*****,** Materials Science and Engineering, University of California San Diego, USA

2019 ***Doctor of Philosophy,*** Materials Science and Engineering, University of California San Diego, USA

PUBLICATIONS

Dissertation Related

Y. Li, J. Wang, W. Xiong, (2015). *Probing Electronic Structures of Organic Semiconductors at Buried Interfaces by Electronic Sum Frequency Generation Spectroscopy.* The Journal of Physical Chemistry C, 119(50), 28083-28089.

Y. Li, J. Wang, M. L. Clark, C. P. Kubiak, W. Xiong, (2016). *Characterizing interstate vibrational coherent dynamics of surface adsorbed catalysts by fourth-order 3D SFG spectroscopy*. Chemical Physics Letters, 650, 1-6.

B. Xiang,* **Y. Li**,* C. H. Pham, F. Paesani, W. Xiong, (2017). *Ultrafast direct electron transfer at organic semiconductor and metal interfaces.* Science advances, 3(11), e1701508. *Co-first author*

Y. Li, B. Xiang, W. Xiong, (2019). *Heterodyne transient vibrational SFG to reveal molecular responses to interfacial charge transfer.* The Journal of chemical physics, 150(11), 114706.

Y. Li, M. Shrestha, M. Luo, M. Song, V. H. Grassian,* W. Xiong,* (2019). *Salting up of proteins at the air/water interface.* Under Review,

Others

J. Wang, M. L. Clark, **Y. Li**, C. L. Kaslan, C. P. Kubiak, W. Xiong, (2015). *Short-range catalyst–surface interactions revealed by heterodyne two-dimensional sum frequency generation spectroscopy.* The journal of physical chemistry letters, 6(21), 4204-4209.

Z. Li,* J. Wang,* **Y. Li**, W. Xiong, (2016). *Solving the "magic angle" challenge in determining molecular orientation heterogeneity at interfaces*. The Journal of Physical Chemistry C, 120(36), 20239-20246.

M. Shrestha,* M. Luo,* **Y. Li**, B. Xiang, W. Xiong, V. H. Grassian, (2018). *Let there be light: stability of palmitic acid monolayers at the air/salt water interface in the presence and absence of simulated solar light and a photosensitizer*. Chemical science, 9(26), 5716-5723.

B. Xiang, R. F. Ribeiro, A. D. Dunkelberger, J. Wang, **Y. Li**, B. S. Simpkins, B. S. Simpkins, J. C. Owrutsky, J. Yuen-Zhou, W. Xiong, (2018). *Two-dimensional infrared spectroscopy of vibrational polaritons*. Proceedings of the National Academy of Sciences, 115(19), 4845-4850.

S. Wang, Z. Huang, X. Wang, **Y. Li**, M. Gunther, S. Valenzuela, P. Parikh, A. Cabreros, W. Xiong,* Y. S. Meng*, (2018). *Unveiling the Role of TBP–LiTFSI Complexes in Perovskite Solar Cells*. Journal of the American Chemical Society, 140(48), 16720-16730.

T. M. Porter,* J. Wang,* **Y. Li**, B. Xiang, C. Salsman, J. S. Miller, W. Xiong,* C. P. Kubiak, (2019). *Direct observation of the intermediate in an ultrafast* isomerization. Chemical science, 10(1), 113-117.

V. O. Ozcelik, **Y. Li**, W. Xiong, F. Paesani, (2019). *Modeling the morphology effects on the charge transfer process at metal/organic interfaces.* Under Review

H. Qian, S. Li, **Y. Li**, J. Chen, S. E. Bopp, Y. Lee, W. Xiong, Z. Liu, (2019). *Nanoscale optical pulse limiter enabled by refractory metallic quantum wells*. Under Review

ABSTRACT OF THE DISSERTATION

Ultrafast Nonlinear Spectroscopy Study of Interfaces and Surfaces

by

Yingmin Li

Doctor of Philosophy in Materials Science and Engineering

University of California San Diego, 2019

Professor Wei Xiong, Chair

Interfaces and surfaces are ubiquitous in people's daily life and they play a pivotal role in many research fields such as molecular electronics, photovoltaics, and environmental chemistry. However, due to the lack of interface-specific probes, there are plenty of questions remain unsolved for interfaces. During the past few decades, thanks to the development of ultrafast pulsed laser technology, nonlinear spectroscopy has merged to be a powerful technique to characterize the properties of interfaces. In this dissertation, several novel nonlinear spectroscopic methods will be discussed and used to perform static as well as kinetic study of interfaces.

First, the major emphasis of this dissertation is to understand the electronic structure and charge transfer dynamics at the interface formed by an organic semiconductor – poly(3-hexylthiophene-2,5-diyl) (P3HT) and a metal – gold or an inorganic semiconductor – silicon. Using the interface specific sum frequency generation spectroscopy (SFG), a method of measuring the band gap of buried interfaces is established. The result demonstrates that the electronic structure at buried interface differs from that of the bulk. By combining the transient absorption spectroscopy and vibrational sum frequency generation (VSFG) spectroscopy, the first dynamical electric-field-induced VSFG signal is observed and for the first time, a spectroscopic evidence of direct electron transfer at complex polymer/metal interfaces is presented. Aided by heterodyne detection, a phase rotation approach has been established to disentangle the pure molecular response from the electronic nonresonance to interfacial charge transfer.

The first fourth order three-dimensional SFG spectroscopy (3D SFG) is introduced and used to measure the interstate vibrational coherences from a Re(diCN-bpy)$(CO)_3Cl$ monolayer adsorbed on gold surface. It is learned that the surface attachment induces both homogeneous and inhomogeneous dephasing dynamics of the vibrational mode. However, the coherence is preserved upon surface attachment.

Other than applying to air/solid and solid/solid interfaces, nonlinear spectroscopy is also powerful to learn air/aqueous interfaces. VSFG is used to explore the protein adsorption kinetics at air/salt water interface under environmentally relevant conditions. In combination of surface pressure measurement, a novel "salting up" phenomenon is proposed, and the role of ions is discussed. Moreover, a critical surface coverage needs to be satisfied to induce the conformational change of proteins at the surface.

Overall, nonlinear spectroscopy has been proved to be an ideal candidate for non-destructive and interface specific characterization method. By choosing the appropriate method, both static and kinetic information can be achieved.

Chapter 1 Introduction

1.1 Motivation

In 2000, Professor Herbert Kroemer coined the famous phrase that "the interface is the device" on his Nobel Lecture which implies the importance of understanding the properties of interfaces in heterostructures such as optoelectronic devices and light-emitting devices.[1] An interface, in most cases, is referred to the boundary formed by two different matters that have either the same or different physical states. The interface composed by matter and air is called surface. In the past few decades, interfaces and surfaces have attracted tremendous interest from researchers in different fields, including molecular electronics,[2,3] photovoltaics,[4] surface catalysts[5,6] and environmental chemistry.[7,8]

Why surfaces and interfaces are interesting to study and pivotal to understand? Unlike in the bulk, materials at interfaces have unique properties that are induced by the anisotropic molecular ordering and structuring.[9,10] In addition, upon the contact to a different material, the new created interface would exhibit totally different electrical,[11–13] optical,[9,14] as well as magnetic properties from the material on either side of the interface.[15,16] Therefore, fully understanding and controlling interfaces have great potential to improve the performance of a variety of devices. For example, during the past few decades, p-n junction, a classic device in semiconductor industry which is essential to many electronics, has been extensively studied. It is found that the interfacial area formed by two semiconductors (one n-type and one p-type) is critical to device performance. Recent studies on p-n junctions in photovoltaics suggest that by engineering the interface, the potential difference across the interface can be optimized and higher charge separation efficiency can be accomplished.[4] Other research efforts were spent on developing transparent conductive oxides to make transparent p-n junction devices such as UV-light emitting diodes (LEDs) with abrupt interfaces.[17] Two-dimensional transition metal dichalcogenides (2D TMDs) are applied to develop lateral p-n junctions with atomically sharp interface including WS_2/MoS_2 and $MoSe_2/WSe_2$ to achieve high on-off current ratios and distinctive electro-optical properties.[18] This indicates that choosing a right interface will greatly enhance a device performance in many aspects. In recent years, the efforts to engineer interfaces have extended to molecular electronics which introduce modifications to the surface and interface in traditional electronic devices by adding a molecular monolayer which can significantly alter the band structure and charge behavior at interface.[2,19–21] The emergence of this exciting research topic has brought the importance of interfaces to an unprecedented molecular level and characterization methods are in great need to uncover the missing molecular knowledge about surfaces and interfaces.

In recent years, many techniques have been discovered to detect surfaces and interfaces where different types of probes are applied. Scanning probe microscopies (SPM), such as atomic force microscopy (AFM) and scanning tunneling microscopy (STM), are utilized to study the morphology of surfaces.[22–25] By scanning a physical probe around the sample, images with atomic level resolution are obtained. However, SPM doesn't have the access to buried interfaces including liquid/solid and solid/solid systems. Electron is also a powerful tool to detect interfacial areas. For instance, X-ray photoelectron spectroscopy (XPS) and ultraviolet photoelectron spectroscopy (UPS) are utilized to determine the band alignments.[26–28] Auger electron spectroscopy (AES) provides information about surface composition.[29] However, in most surface sensitive electron spectroscopies, ultra-high vacuum conditions are required which makes the setup and measurement to be sophisticated. The need for vacuum also limits their application to certain specimen. Moreover, the techniques mentioned above can only access to the top surface instead of buried interfaces which would retain different properties and structures.

Optical probe has been proven as good candidate to study surfaces and interfaces.[30–32] Photons can be propagated and detected under ambient conditions which makes it easy to build the instrument. Other than that, the penetration depth of incident beam is on the order of hundreds of nanometers or even longer which enables the optical probe to access buried interfaces easily. Optical probe, in most cases, is also non-destructive to the specimen. Optical spectroscopy can detect molecular rotational transitions, vibrational transition, and electronic transitions by selectively choosing the incident photon energy, which in principle makes it applicable to study any interface accessible to light. One major problem of traditional optical spectroscopy, such as Ultraviolet-visible spectroscopy and Fourier-transform infrared spectroscopy, is while the light can detect interface, it simultaneously generates response from the bulk. As bulk accounts for larger volume, the signal from interface is overwhelmed by that from the bulk which indicates surface/interface sensitive optical spectroscopies need to be discovered to suppress the bulk response.

A few decades ago, the discovery of second harmonic generation spectroscopy (SHG) pioneered the development of the interface sensitive nonlinear optical spectroscopy.[33] More technologies such as sum frequency generation spectroscopy (SFG) and two-dimensional sum frequency generation spectroscopy (2D SFG) have been developed ever since to perform surface/interface specific research on different systems.[30,34] Li *et al* used chiral SFG spectroscopy to realize the in *situ* and real-time measurement of the protein secondary structures at interfaces, different conformations including random coils, α-helices and β-sheets can be observed at the lipid-water interface.[35] Water structures at various surfaces associate with different salt ions and lipids, including phospholipid membranes and zwitterionic lipid, were explored by both homodyne detected and heterodyne detected vibrational SFG spectroscopy.[35–39] The charge transfer state of CO on Pt (111) was probed by SFG, and the band structure at surface was determined.[40] Hot electron transfer from semiconductor nanocrystals, such as lead selenide on titanium dioxide, was investigated by time-resolved SHG spectroscopy.[41]

As shown in above cases, most of previous studies focused on probing the top surface whereas buried interfaces are barely explored. Moreover, SHG and SFG have mostly be applied to simple molecular interfaces, such as water, model peptides etc., whereas complex interfaces are relatively less explored. Molecular responses during the charge transfer process remain unclear and the role of molecular conformation during the charge dynamics hasn't been explored. This is mostly because complicated ultrafast dynamics on molecular interfaces are folded into a one-dimensional information in SHG and SFG spectroscopy and thereby convoluted. New interfacial optical techniques are needed to either investigate interfaces from different aspects, or expanding existing techniques into new time, frequency and spatial domains. Therefore, during my PhD career, to add new weapons to the arsenal to fight against the difficulties of probing interfaces, I have been working on developing and applying new nonlinear optical spectroscopy to learn more molecular details on complex interfaces, and they include: applied electronic SFG spectroscopy to measure the electronic structures at buried interfaces (chapter 3); developed transient vibrational SFG spectroscopy to resolve ultrafast charge dynamics at complex molecular interfaces and implemented heterodyne detection to extract out molecular responses (chapter 4 & 5); established forth order 3D SFG spectroscopy to study surface adsorbed catalyst monolayers (chapter 6); explored protein adsorption kinetics at air/water interface with vibrational SFG in combine with surface pressure measurement (chapter 7).

1.2 Ultrafast Nonlinear Spectroscopy and Research Objectives

As discussed above, there has been a tremendous growth in nonlinear optical spectroscopy. What is nonlinear spectroscopy? It is well-known that when shed light on an object, there will be different forms of light-matter interactions which can be generally summarized in eq. 1.1, where $P(t)$ is the polarization density at time t, $E(t)$ is the electric field driven by the incident light, $\chi^{(n)}$ is the nth order susceptibility of the medium. When the incident field is weak, the nonlinear polarization terms can be ignored so that the polarization is proportional to the incident light intensity. However, when we use intense light field (usually a laser light source) to interact with samples, the higher order terms are not negligible any more. Therefore, the nonlinearity of the specimen can be obtained through multiple light-matter interactions which is what nonlinear spectroscopy studies. It should be noted that not all the nonlinear spectroscopy methods have the interface selectivity. However, through the deliberate design of beam geometry and incident wavelength, even order of nonlinear spectroscopy methods which are inherently interface/surface sensitive can be achieved (details are discussed in Chapter 2).

$$\boldsymbol{P}(t) = \varepsilon_0 \left(\chi^{(1)}\boldsymbol{E}(t) + \chi^{(2)}\boldsymbol{E}^2(t) + \chi^{(3)}\boldsymbol{E}^3(t) + \cdots + \chi^{(n)}\boldsymbol{E}^n(t)\right) = \varepsilon_0 \sum_{i=1}^{n} \chi^{(i)}\boldsymbol{E}^i(t) \qquad (1.1)$$

Femtosecond laser systems generate high power laser beams that have the pulse duration on the order of tens of femtoseconds. They have been widely used as the light source for nonlinear spectrometers. Its high pulse energy and short pulse duration facilitate both static and kinetic analysis of surfaces and interfaces, especially the observation of ultrafast processes in nanomaterials at their spatial and temporal limits. In this dissertation, special experimental setups are designed for developing new nonlinear spectroscopy techniques which are then applied to study different types of interfaces including semiconductor/semiconductor interface, semiconductor/metal interface, air/solid interfaces, and air/aqueous interface. An emphasis will be placed on understanding the electronic structures and the change transfer dynamics at buried interface. Different types of charge behaviors will be investigated through time-resolved methods. Phase sensitive detection scheme is utilized to retrieve the phase information. Furthermore, catalysts for CO_2 reduction attached on gold surface will be explored to demonstrate the ability of nonlinear spectroscopy to study monolayers adsorbed on solid substrate. Protein adsorption kinetics at air/water interface will be studied as an example application to air/aqueous interface.

Chapter 2 Experimental Methodology and Background

In this chapter, the principles and typical setup of nonlinear spectrometers that used to study interfaces and surfaces are introduced. A brief introduction of femtosecond laser systems will be included in 2.1. A second order nonlinear spectroscopy, sum frequency generation (SFG) spectroscopy which is capable of obtaining static interfacial specific information will be discussed in 2.2. In 2.3, transient vibrational sum frequency generation spectroscopy (tr-VSFG) which is a tool to learn the dynamics at interfaces is demonstrated. Higher order of nonlinear spectroscopy methods including two-dimensional sum frequency generation (2D SFG) and three-dimensional sum frequency generation (3D SFG) spectroscopy are discussed in 2.4. At the end of chapter 2, different scenarios of signal collection will be introduced.

2.1 Femtosecond Laser and Optical Parametric Amplifier

The past few decades have witnessed tremendous development of laser technology. Techniques such as modelocking, self-phase modulation, and chirped pulse amplification make it possible to create ultrashort laser pulses while maintain high pulse energy. This is important as short pulse duration would provide high time resolution and high pulse energy would generate enough photons to study material's nonlinearity. Nowadays, femtosecond lasers can produce thousands of pulses in one second with the pulse duration on the order of tens of femtosecond. The ability to generate high power laser pulses facilitates the prosperity of nonlinear optics and enables great advancement in ultrafast nonlinear spectroscopy.

The research reported in this dissertation is carried out using a Titanium-sapphire (Ti:sapphire) laser system from Coherent as the light source. The gain medium is a sapphire crystal (Al_2O_3) doped with Ti^{3+} ions. Our Ti:sapphire laser out puts at 790 nm with 1kHz repetition rate. The output power is ~ 6 W and the pulse duration is 35-50 fs.

As the molecular electronic transitions and vibrational transitions we're interested in absorb in the near-infrared (NIR) and mid-infrared (MIR) spectral region, the output 790 nm light need to be converted into different wavelength to be on resonance with different transitions. Optical parametric amplifier, abbreviated OPA, is applied to realize the wavelength conversion from red edge of visible spectrum to the infrared spectrum.

It should be noted that the design of OPA differs from one to another depending on the requirement of output wavelength and output pulse energy. The model used in this dissertation is TOPAS-Prime from Light Conversion which possesses a two-stage parametric amplifier geometry (as shown in Figure 2-1). Its basic configuration consists of several components: pump beam delivery and splitting optics (PO), white-light spectrum generator (WLG), the first amplification stage (pre-amplifier, PA1), a beam expander-collimator (SE), and the second amplification stage (power amplifier, PA2). The rotational and translational stages in the OPA are controlled by the computer which enables a fast and precise tuning of the output wavelength.

The 790 nm output from the laser head is sent into the OPA at A0 which is then splitted into two parts by BS1. The small fraction is further splitted into two parts at BS2 where one of them (small portion, line 3) is used as the seed to produce white-light continuum (WLC) in a sapphire plate. The white light has a broad spectral coverage which enables the tunable IR output later. The other part (major portion, line 4) of the small fraction and the white light are focused onto the nonlinear crystal (NC1) for first stage of amplification and the two pulse are spatially and temporally overlapped. A non-colinear geometry is used for the easy separation of the signal beam. Only the signal beam is picked up (line 6) and expanded, then collimated by a lens telescope. At the second stage of amplification, the major component of 790 nm input (line 2) is used as the pump to amplify the signal beam after the first amplification stage and it is downsized to achieve high pump intensity by a lens-mirror telescope. The beam geometry is colinear at second stage of amplification which means the final output signal and idler beams are colinear. A dichroic mirror is applied to get rid of the pump residue (DM3) and only output the signal and idler beam which are both in the near infrared spectral region. To tune the final output wavelength, the time delay of seed light with respect to the pump pulse is changed and the orientation of both nonlinear crystals need to be adjusted to meet the phase matching condition.

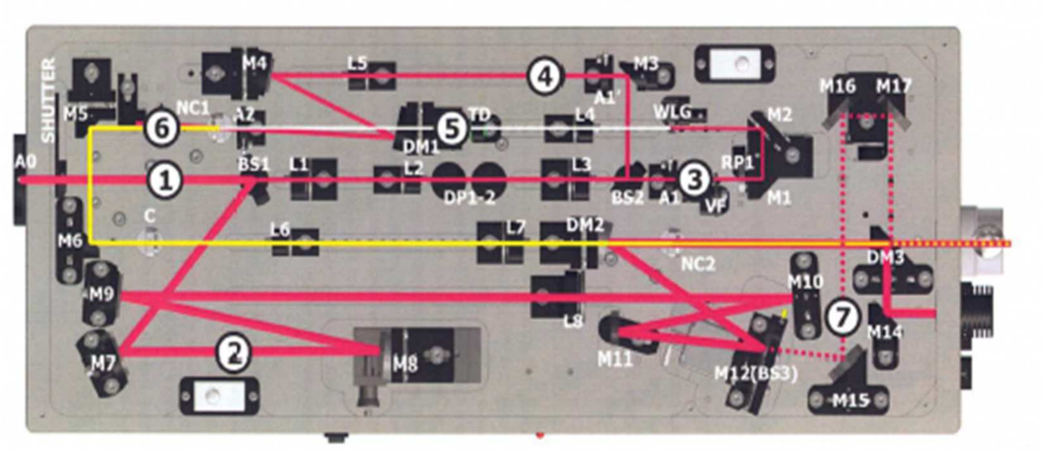

Figure 2-1. The layout of TOPAS-Prime. The pink lines indicate the 790 nm beams. White line represents the white light continuum and the yellow lines denotes the signal and idler beams of near IR. Thicker lines stands for higher intensity while thinner lines for lower intensity.

The output near IR beams can be directly used to study the nonlinearities of materials such as optical kerr effect or laser induced structural change. However, in order to probe the molecular vibrational modes which absorb in the mid-infrared spectral region, a different frequency generation process is needed to realize the frequency conversion. Nonlinear crystals such as lithium triborate (LBO), barium borate (BBO) and silver gallium sulfide (AGS) are usually used as the media for mid IR generation.

2.2 Sum Frequency Generation Spectroscopy

As discussed in chapter 1, nonlinear spectroscopic methods are implemented to study interfaces and surfaces. SFG spectroscopy, a second-order nonlinear technology, is inherently sensitive to space geometry which makes it a powerful tool to achieve this goal. The surface selectivity of SFG stems from $\chi^{(2)}$, known as second order susceptibility, which is an intrinsic property of materials. The reason is explained as follow: as explained in eq. 1.1, there's a relation between the incident electromagnetic wave and the polarization induced by it. If we assume an inversion operator, I_{Inv}, defined by $I_{Inv}\boldsymbol{P} = -\boldsymbol{P}$, and apply it to the total induced polarization, we have:

$$-\boldsymbol{P} = I_{Inv}\varepsilon_0 \textstyle\sum_{i=1}^{n} \chi^{(i)}\boldsymbol{E}^i(t) = \varepsilon_0 \sum_{i=1}^{n}(-1)^i \chi^{(i)}\boldsymbol{E}^i(t) \qquad (2.1)$$

Sum up eq. 1.1 and eq. 2.1, we have:

$$\varepsilon_0 \sum_{i=1}^{n} \chi^{(i)}\boldsymbol{E}^i(t) + \varepsilon_0 \sum_{i=1}^{n}(-1)^i \chi^{(i)}\boldsymbol{E}^i(t) = \varepsilon_0 \sum_{i=1}^{n}(1 + (-1)^i)\chi^{(i)}\boldsymbol{E}^i(t) = 0 \qquad (2.2)$$

Based on eq. 2.2, it can be learned that the even order susceptibility, $\chi^{(2i)}$, equals to 0 in centrosymmetric media. Therefore, the even order susceptibilities can only survive at interfaces where the centrosymmetry is broken so that it can generate a response to the incident light. This explains the interface sensitivity not only for second order process like SFG, but also for higher even order process such as 2D SFG which will be discussed later.

In general, it requires two light matter interactions to generate SFG signal which means two laser pulses are shed onto the sample surface. Depending on the different resonant conditions, SFG can be categorized in vibrational sum frequency generation (VSFG) and electronic sum frequency generation (ESFG) as demonstrated in the following section.

2.2.1 Vibrational Sum Frequency Generation Spectroscopy

VSFG was first developed in the 1980s and has been extensively used as a surface/interface selective probe. In a typical VSFG experiment, an IR beam and a visible beam are chosen to interact with the sample following the energy diagram depicted in Figure 2-2. The wavelength of IR beam (MIR in most cases) is tuned to be on resonance with specific molecular vibrational mode to initiate an excitation from ground state to excited state in the sample. Meanwhile, the visible beam is spatially and temporally overlapped with the IR beam to bring the excitation to a virtual state which allows the emission of VSFG signal ($\omega_{VSFG=}\ \omega_{IR+}\ \omega_{Vis}$) at the sum frequency of the IR photon (ω_{IR}) and the visible photon (ω_{Vis}). This process is also known as upconversion as it converts the information-bearing beam from IR region (low photon energy) to visible region (high photon energy). Upconversion method is favorable in terms of both providing the interface sensitivity and better detection sensitivity (knowing that the detectors are more sensitive to visible light over the infrared light). The mathematical express of VSFG process can be written as following equation:

$$E^{I}_{SFG}(\omega_{SFG}) \propto \sum_{JK} \chi^{(2)}_{IJK} E^{J}_{Vis}(\omega_{Vis}) E^{K}_{IR}(\omega_{IR}) \tag{2.3}$$

where I, J, K are the Cartesian component coordinate of the electromagnetic fields and $\chi_{IJK}^{(2)}$ is the element of second order susceptibility tensor $\chi^{(2)}$.

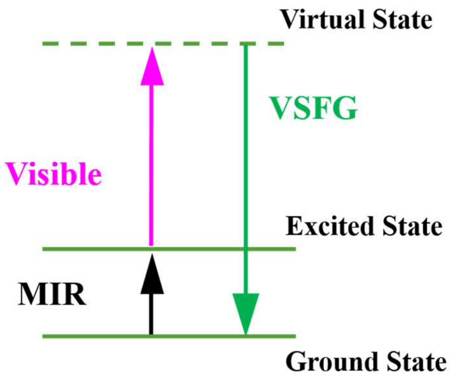

Figure 2-2. A schematic illustration of the energy diagram of VSFG process.

2.2.2 Electronic Sum Frequency Generation Spectroscopy

Unlike VSFG where a single IR beam is utilized to excite the sample, ESFG has two excitation beams interacting with the sample to create electronic excitation. Therefore, while VSFG can provide information about vibrational modes, ESFG probes the interfacial area from an electronic perspective. The energy diagram of an ESFG process is shown in Figure 2-3. A NIR beam and a visible beam are spatially and temporally overlapped at the sample surface to hit on an electronic resonance. The ESFG process have the same mathematical expression as VSFG and the emission wavelength is $\omega_{ESFG=}\ \omega_{NIR+}\ \omega_{Vis}$.

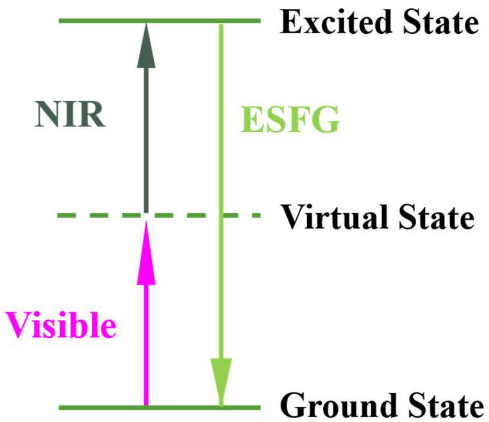

Figure 2-3. A schematic illustration of the energy diagram of ESFG process.

2.3 Transient Vibrational Sum Frequency Generation Spectroscopy

Ultrafast transient absorption spectroscopy is another commonly used nonlinear spectroscopy technique. As a third order nonlinear process, it is not interface specific, which means the response from interface or surface would be mixed with that from the bulk. In a typical transient absorption spectroscopy measurement, pump-probe method is employed, where a pump beam first creates an excitation in the sample. After certain waiting time (Δt), a probe beam comes in to interact with the sample and characterize the relaxation of the excited states. In this way, the response of the sample to the optical excitation can be obtained and by scanning the time delay between pump and probe, it is possible to learn how the system evolves along the time upon the external perturbation. Therefore, transient spectroscopy is often used as a tool to study kinetic processes including the charge transfer dynamics, molecular conformational change, and protein adsorption dynamics. The resolution of transient measurement is determined by the laser pulse duration.

In order to better characterize the changes in absorption spectrum as a function of time, the concept of pump-probe signal is introduced. That is, at each Δt, an absorbance spectrum is collected both before the system got pumped (pump off spectrum) and after pumped (pump on spectrum). Then the pump on spectrum is subtracted by the pump off spectrum to get the pump probe spectrum. In traditional transient absorption studies, the pump probe signal contains a lot of information, where the negative part indicates the ground state bleaching, while the positive part shows the higher state excitation. Ground state bleach stems from the depletion of carriers in ground state due to the excitation, which will reduce the absorption cross section of the ground state that generates smaller signal in pump on spectrum comparing to pump off spectrum.

From the previous discussions, we learn SFG is powerful in terms of providing static interfacial specific information whereas transient absorption technique enables dynamic study of a bulk system. A method which combines the advantages of both techniques is developed to get interfacial specific information that is transient vibrational sum frequency generation spectroscopy (tr-VSFG). A femtosecond laser pulse, which serves as the pump, first interacts with the sample. After a time delay, a VSFG probe, comes in to selectively detect the interfacial response to the pump excitation. The tr-VSFG technology will be utilized to explore the charge transfer dynamics across the interface in the following chapter.

2.4 Multi-Dimensional Sum Frequency Generation Spectroscopy

From previous sections, one-dimensional spectroscopy methods showed great capability of studying surfaces and interfaces from both static and dynamic point of view. Important information such as frequency resolved spectra, time dependent absorption, and lineshape can be obtained. However, when dealing with samples that have multiple vibrational modes in a narrow spectral region or exhibit great spectral broadening, one-dimensional spectroscopy has the limitations of unambiguously disentangling different vibrational modes and determining the homogenous and inhomogenous broadening linewidth. Therefore, the interactions between different modes including coupling, energy transfer can't be studied. One solution is to do multi-dimensional spectroscopy where an additional frequency axis is added through creating another coherence by the pump sequence. More observables such as the evolution of cross peaks, 2D lineshape can be extracted out from 2D spectra. In this section, multi-dimensional spectroscopic methods will be introduced which are two-dimensional sum frequency generation spectroscopy (2D SFG) and three-dimensional sum frequency generation spectroscopy (3D SFG). It should be noted that 2D SFG also has the interface selectivity as it is a fourth order nonlinear process.

A typical 2D SFG experiment has the pulse sequence showed in Figure 2-4. Two IR pump pulses interact with the sample first to create a coherence between the ground state and excited population state. The two pulses are separated by a tunable time delay t_1 which is controlled by a spectral pulse shaper. After a waiting time of t_2, another IR pulse comes in to probe the system to generate a second coherence. A visible beam is sent into the sample at the same time to upconvert the oscillation (that has the lifetime of t_3) to visible spectral region to be detected. Both t_1 and t_3 are scanned in time and then get converted into frequency domain through Fourier transform to get two frequency resolved axis. To make it simpler, a 2D SFG pulse sequence can be regarded as an SFG pulse sequence with additional two excitation pulses.

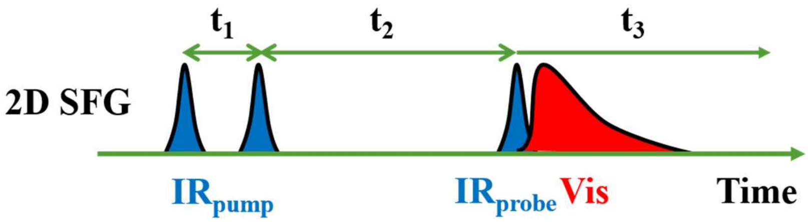

Figure 2-4. Schematic of 2D SFG pulse sequence. First two blue pulses are IR pump, the third one is IR probe, and the broad band pulse is the visible beam that used for upconversion.

2D SFG spectrum (a schematic is included in Figure 2-5.) has notably different features from linear SFG spectrum. First of all, both X and Y axis resemble frequency for a 2D spectrum which are denoted as ω_1 and ω_3. While ω_1 shows the oscillation induced by the pair of pump pulse between t_1, ω_3 depicts the decay induced by the probe pulse in t_3. The signal intensity is reflected by the pseudo color map. Secondly, the absorption of each molecular vibrational mode would show up as a doublet peak along the diagonal in a 2D SFG spectrum. In Figure 2-5, for example, there are two pairs of peaks which indicates two molecular absorptions in the probing spectral region. The reason is that the one locates right along the diagonal is generated through the fundamental transition ($\nu = 0 \rightarrow 1$) while the out-of-phase peak is the result of overtone transition ($\nu = 1 \rightarrow 2$). Last but not the least, there would be cross peaks showing up at the off diagonal direction which are referred as cross peaks. The appearance of cross peaks is due to the coupling between different vibrational modes which means 2D SFG can provide information about the interactions between different oscillators in the molecules. By analyzing the spectral lineshape of 2D SFG peaks, the homogenous and inhomogeneous broadening information can be extracted out. Since the phase of doublets depends on the directions of the transition dipole moment and the transition polarizability, we can also learn the information about the molecular orientation at interfaces.

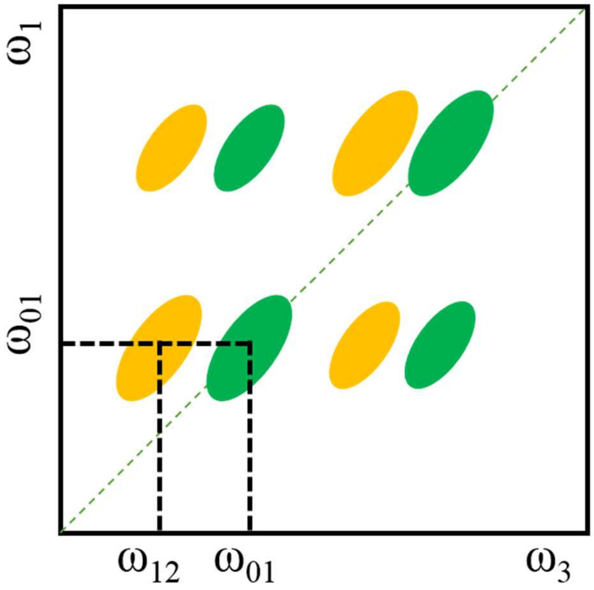

Figure 2-5. A schematic of typical 2D SFG spectrum. The fundamental peaks are colored in green whereas the overtone peaks are in orange. ω_{01} denotes the fundamental transition from ground state to first excited state, ω_{12} represents the overtone transition from first excited state to second excited state.

3D SFG has the same experimental setup as 2D SFG. The major difference between the two is for 3D SFG, by scanning t_2, a third frequency axis can be achieved through Fourier transform t_2 into frequency domain. Besides measuring the vibrational coherences of single vibrational modes, the fourth-order 3D SFG spectrum also measures the dynamics of interstate coherences and vibrational coherences states between two vibrational modes.

2.5 Signal Detection Methods

In this section, different signal detection schemes utilized in this dissertation are introduced including homodyne detection and heterodyne detection. An emphasis will be placed on describing the phase sensitivity of heterodyne detection over homodyne detection.

2.5.1 Homodyne Detection

In homodyne detection scenario, the intensities of emitted electromagnetic waves are detected directly on the detector. During this process, the phase information would be lost as shown in an example for homodyne detected SFG signal in equation 2.4, where I_{SFG} denotes the intensity of SFG signal, E_{SFG} is the electric field of SFG emission, $e^{-i\phi}$ is the phase of the electromagnetic field.

$$I_{SFG\ HO} \propto |E_{SFG} * e^{-i\emptyset}|^2 = |E_{SFG}|^2 \tag{2.4}$$

2.5.2 Heterodyne Detection

As discussed in section 2.5.1, homodyne detection measures the absolute intensity of the nonlinear signals where the phase information is lost. In some cases, such as probing the surface species or measuring the interfacial electronic structure, the phase of signal is not critical for data interpretation. Some other conditions, however, where molecular orientations are in great interests or there are multiple spectral components contributing to the detected spectrum, getting phase information is critical to unveil the structure at surfaces or interfaces and overcome the interference issue between different spectral components. In this section, optical heterodyne detection will be introduced as a tool to maintain the phase information.

In heterodyne detection scenario, a local oscillator (LO) is generated on a sample that has a known phase. The LO, which is relatively delayed to the SFG signal from the sample, will then interact with the SFG signal to generate an interferogram. The phase information contains in the fringes in the interferogram. Here, a heterodyne detected SFG signal is again used as an example, where E_{LO} is the electric field of LO, $e^{-i\phi_{LO}}$ is the phase of the LO signal. The heterodyne signal contains both DC terms (the first two terms) and the AC term (cross term between SFG and LO). From eq. 2.5, it's obvious that the phase of SFG signal can be retrieved from the heterodyne detected signal by doing the phase calibration for the AC term.

$$
\begin{aligned}
I_{SFG\ HD} &= \left|E_{SFG} * e^{-i\emptyset} + E_{LO} * e^{-i\emptyset_{LO}}\right|^2 \\
&= |E_{SFG}|^2 + |E_{LO}|^2 + 2|E_{SFG}||E_{LO}|\cos(\emptyset_{LO} - \emptyset) \qquad (2.5)
\end{aligned}
$$

For analyzing heterodyne detected data, the frequency resolved spectrum will first be Fourier transformed into time domain, where the DC terms which oscillates around zero point on the time axis is eliminated by applying a step filter. The remaining AC signal will be Fourier transformed back to frequency domain, followed by a phase calibration process where the phase of LO will be added to the AC term to retrieve the phase resolved SFG signal.

Other than phase sensitivity, heterodyne detection outweighs homodyne detection in other aspects. Since the LO beam is much stronger than the SFG signal, the intensity of the cross-term is greatly enhanced which means the signal-to-noise ratio is significantly improved. This is important because the application of SFG is sometimes limited by the small signal intensity and long data acquisition course. With the help of heterodyne detection, nonlinear spectroscopy can be utilized to study monolayer samples which generates very small response and hard to be detected using homodyne detection. Heterodyne detection also enables the separation of molecular signal from the large electronic nonresonance which is impossible for homodyne detected spectrum. The nonresonant signal usually shows up as a large broad Gaussian shaped background which makes it hard to identify the molecular response. These advantages will be demonstrated in more details in the later chapters.

In this chapter, ultrafast nonlinear spectroscopy techniques used in this thesis are discussed, both their fundamental theories and features are introduced. More details including the beam geometry of each spectrometer will be demonstrated in the following chapters.

Chapter 3 Probing Electronic Structures of Organic Semiconductors at Buried Interfaces by Electronic Sum Frequency Generation

In this chapter, a second order nonlinear spectroscopy method – Electronic Sum Frequency Generation Spectroscopy (ESFG) will be employed to study the electronic structures at a buried solid/solid interface for the first time. The system is an organic thin film, poly(3-hexylthiophene-2,5-diyl) (P3HT), supported on a silicon surface. The ESFG measurement is only in resonance with electronic (or vibronic) excitations, thus capable of yielding rich information of the band gap and electronic structures of the P3HT film at interface. We find the bandgap of P3HT in contact with silicon is 2.2 eV, with a narrowed bandwidth and Lorentzian lineshape. This is significantly distinct from the UV-Vis spectra of bulk P3HT, which contains multiple broad Gaussian peaks. Our measurement demonstrates at interfaces regioregular P3HT has a uniform electronic structure, which could improve the short circuit currents. The unique capability of ESFG to probe electronic structures at buried interface under atmosphere will be useful for investigating many buried interfaces.

3.1 Introduction

Buried interfaces are ubiquitous in devices such as field effect transistors[42,43], light emitting diodes[44] and photovoltaics.[45,46] The band gap and electronic structures at buried interfaces are crucial in understanding and predicting the charge carrier behaviors at interfaces, such as exciton and polaron formations, charge separations and recombinations.[45,47–50] However, the bandgap and electronics structures at the interfacial region, where two materials are in contact with each other, can differ from the bulk, because of interfacial interactions.[51–55] Therefore, robust and direct methods are needed to probe the band gaps as well as electronic structures at buried interfaces.

Significant successes on determining interfacial electronic properties of materials in vacuum have been achieved by surface techniques. For example, UV photoelectron spectroscopy[48,52,55] or Ballistic-Electron-Emission Microscopy[56] can determine the band alignment at interfaces of films with precisely-controlled thickness. It is found that in the films that are a few molecules thick, electron tunneling between two domains significantly changes the electronic structures of the molecules at interfaces[57,58].

Aside from measurements in vacuum condition, determining electronic structure at interfaces under atmospheric conditions is also necessary. Atmosphere resembles the working environments of devices, and the electronic and molecular structures of interfacial molecules under atmosphere can be significantly different from the ideal vacuum condition[53]. It is difficult to directly extend the vacuum techniques into measurements under atmosphere. Only some recent advances in differential pumping allow photoelectron spectroscopic techniques to study surfaces under ambient condition (a few Torr)[59].

More often, optical spectroscopies are used and developed for probing electronic structure of interfaces under atmosphere. For instance, bulk sensitive optical techniques, such as linear absorption spectroscopy, are widely used to probe nanometer-thick films, whose properties are used to approximate the interface properties.[60–63] It is questionable whether such an approximation is valid. For instance, can we use the optical spectra of thin films to extract electronic structure information of the molecules at interfaces?

In this report, we demonstrate for the first time, that electronic sum frequency generation (ESFG) spectroscopy[64–68] can determine electronic structures of interfacial molecules at solid/solid interfaces. Like other sum frequency generation techniques and electronic second harmonic generations[32,69], ESFG is intrinsically interface sensitive, since it is a second order coherent optical signal that can only be generated from non-centrosymmetric media.

We investigated the organic/inorganic semiconductor interfaces composed by poly(3-hexylthiophene-2,5-diyl) (P3HT) and n-doped Si (111). We found although the P3HT polymers have a complicated electronic structure distribution in the bulk, which results in multiple broad visible transitions, only one narrow Lorentzian peak dominates the ESFG spectrum, indicating that the conformation of P3HT at interfaces are more uniform than the bulk.

3.2 Experimental Methods and Theoretical Background

A Ti:Sapphire regenerative amplifier is used to generate 6mJ, 35 fs, 800nm pulse at 1kHz (Astrella, Coherent). Majority of the beam is sent to an OPA system (TOPAS, Light Conversion) to generate the signal and idler beams. Based on the band gaps of the materials, either signal or idler is used as near IR beam in ESFG. A small amount 800nm (<0.5mJ) pass through a band narrowing filter (Idex Optics & Photonics) to create narrowband 800nm spectrum (fwhm = 1.5 nm). The relative delay between 800nm and near IR is controlled by a mechanical stage. Both the near IR and narrowband 800 nm beams are focused by a gold parabolic mirror (EFL= 10 cm, Edmund Optics) onto the sample, with both incident angle to be 60° relative to the surface normal. The ESFG signal is reflected off the sample surface and is collimated by another gold parabolic mirror (EFL = 5 cm, Edmund optics). The signal is sent through short-wavelength pass filter (Newport) to remove residue 800nm beam, and finally sent into a spectrograph to be dispersed and recorded on a CCD camera (Andor). Both near-IR and 800 nm beams are attenuated to reduce sample damage due to multiphoton absorptions. We do not observe any ESFG signal decrease over the course of ESFG measurement (10 mins), which indicates that there is no sample degradation happening.[70] The polarization of ESFG pulse sequence is *SSP*, where the order of the letters corresponds to ESFG, 800 nm and near IR beam. We use this polarization scheme to remove nonresonant contributions from Si substrates. Since the near IR spectra range might not be broad enough to cover the entire electronic transition, we scan the near IR wavelength from 1840 to 2300 nm in a step of 20 nm and plot the overall ESFG counts versus the sum of near IR and 800 nm beams' frequency to find the resonant transitions. ESFG signals of bare Si, GaAs and gold surfaces are also recorded as control and reference samples.

The emitted SFG signal can be expressed as following:

$$I_{SFG}(\omega) \propto \left|x_{eff}^{(2)}\right|^2 I_{800nm}(\omega_{800nm}) I_{IR}(\omega_{IR})$$

$$= \left|x_{NR}^{(2)} + \sum_n x_{ijk,n}^{(2)}(\omega_{SFG}) * e^{i\cdot\varphi_n}\right|^2 I_{800nm}(\omega_{800nm}) I_{IR}(\omega_{IR}) \qquad (3.1)$$

where $x_{eff}^{(2)}$ is the second order susceptibility, which is often composed by the sum of various nonresonant ($x_{NR}^{(2)}$) and resonant ($x_{ijk}^{(2)}(\omega_{SFG})$) transitions. In the homodyne detection scenario, the signal I_{SFG} is proportional to the square of $x_{eff}^{(2)}$, and the products of near IR (I_{IR}) and 800nm (I_{800nm}) beam intensities. As we show below, by normalizing I_{SFG} of the sample to an SFG signal from the reference sample, the dependence on I_{IR} and I_{800nm} can be removed. As a result, we can directly determine $x_{eff}^{(2)}$, which contains $x_{ijk,n}^{(2)}(\omega_{SFG})$. The term $x_{ijk,n}^{(2)}(\omega_{SFG})$ reflects physical properties such as bandgap energy and transition dipole strength of the systems. The resonance second order susceptibility $x_{ijk}^{(2)}(\omega_{SFG})$ [68,71–80] can be written as eq 3.2,

$$x_{ijk}^{(2)}(\omega_{SFG}) \propto \sum_e \frac{<0|\rho|0><0|\mu_i|e><e|\alpha_{jk}|0>}{\omega_{e0}-\omega_{SFG}-i*\varepsilon} \tag{3.2}$$

where |0> and |e> are the ground and excited electronic states of the system, $< 0|\rho|0 >$ is the initial population at ground electronic state, $< e|\alpha_{jk}|0 >$ is the hyperpolarizibility of two-photon absorption, which promotes systems from |0> to |e> through virtual states |v>, and $< 0|\mu_i|e >$ corresponds to the electronic dipole transition that brings the system from |e> to |0> by emitting visible lights. In the denominator, ω_{e0} is the frequency difference between |e> and |0>, ω_{SFG} is the frequency of emitted SFG signal, which satisfies $\omega_{SFG}=\omega_{NIR}+\omega_{800nm}$, and the ε is the dephasing contribution. At resonance condition ($\omega_{e0}=\omega_{SFG}$), the denominator in eq 3.2 approaches to zero, and the ESFG signal is enhanced. Therefore, at resonant, the photon energy of the emitted electric fields equals to the band gap.

We emphasize this equation differs from the formula for vibrational sum frequency generation (VSFG) [45,81–90], in which one of the two incoming pulses are tuned in resonant with molecular transitions. First, all states are electronic states and the contribution from vibrational states are treated implicitly. Second, in a typical VSFG case the hyperpolarizability term corresponds to Raman transition[80], where for ESFG, the hyperpolarizability represents two photon absorption process, as firstly pointed out by Moad and Simpson.[79] Last, the light-matter interaction sequences differ in VSFG and ESFG. In ESFG, the two photon absorption-like light-matter interactions first populate the electronic coherences and then the SFG signal is emitted through a dipole interaction and relaxes the systems from excited coherence state to ground electronic states; In VSFG, a vibrational coherence is excited first, followed by the Raman-like process. We note that in either ESFG or VSFG processes, only coherence states are excited.

To demonstrate our method, we investigate the prototype interfaces of hybrid organic/inorganic photovoltaics composed by poly(3-hexylthiophene-2,5-diyl) (P3HT) and n-doped Si (111).[91] Although P3HT is a well-studied organic semiconductor, a fundamental understand of its bandgap and electronic structure at buried interfaces is still far from being complete. Here we show that ESFG can provide insights on both the band gap and the electronic structure at interfaces. We focus on the regioregular (RRE) form of P3HT, which has all sidechains organized to minimize structural twist from steric effects. The P3HT/Si interfaces are prepared by spin coating onto Si substrate at 2000 rpm speed and 6mg/ml concentration. The thickness of P3HT film is determined to be ~150nm by profilometry. The P3HT/sapphire thin film sample is prepared by the same way, which is used to measure UV-Vis spectra. The UV-Vis is used to remove the reabsorption effects, and also to determine the absorption spectrum of bulk P3HT.

3.3 Electronic Sum Frequency Generation Spectra

The ESFG spectra of RRE P3HT/Si and bare Si substrates are collected and compared in this work (Fig. 3-1b). The ESFG spectra of RRE P3HT/Si and bare Si substrates show different intensities. In Fig. 3-1b, ESFG spectra of both samples at λ_{NIR}=1954 nm indicate that the RRE P3HT/Si has larger ESFG signal than pure Si substrates. This indicates that the ESFG signals of P3HT/Si are dominated by the P3HT at P3HT/Si interfaces, since the ESFG signal from Si substrates is much smaller comparing to the P3HT/Si samples. The signal from Si is suppressed because the *SSP* polarization is used to suppress any non-resonance ESFG signal from Si.

To ensure the measured signal is from the ESFG process described by eq 3.1, we also measure how the signal depends on the power of near IR beam. We control the power of near IR by a pair of waveplate and polarizer, where the polarizer defines the near IR beam polarization and we use the waveplate to control the portion of near IR beam that transmits through the polarizer. We find the measured signal depends on the near IR power linearly (Fig. 3-2a), as described in eq 3.1.

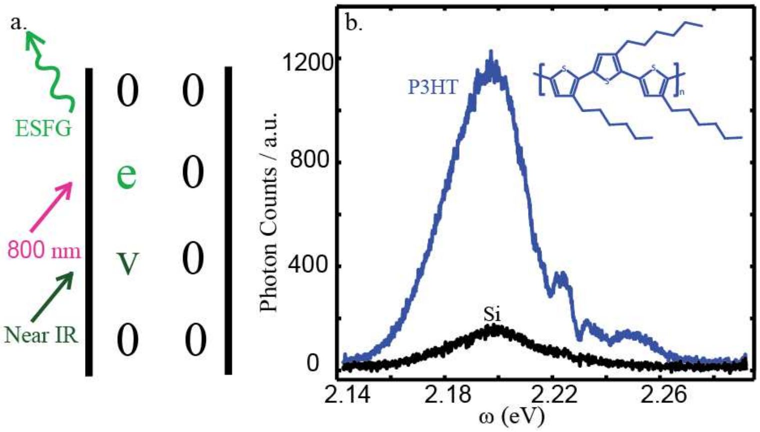

Figure 3-4. ESFG Feynman Diagram (a) and ESFG spectra (b) of regioregular P3HT on Si and bare Si surfaces. The regioregular P3HT on Si has stronger signal than bare Si, indicating the ESFG signal is generated from P3HT layers at the interfaces. The features at 2.22 and 2.23 eV in both spectra are originated from the near IR spectrum.

Next, to determine the interfacial band gap and its distribution, we investigate the ESFG intensity dependence on near IR frequency. We found both the ESFG emission photon energy and the intensity change as the near IR frequency is scanned (Fig. 3-2b). The center frequency of ESFG emission directly matches with the sum of the frequencies of the near IR and the 800 nm beams, which indicates there are no competing processes such as relaxation from high energy manifolds[48,91–94] or coherence transfer[95–97] happening during the ESFG signal emission.

The ESFG intensity dependence on near IR frequency is a result of resonance enhancement, which serves as a measure of band gap transitions at the interface, as discussed in the Theory section. To quantify the resonant enhancement, we plot the ratio of ESFG intensities between P3HT/Si and gold surfaces (PPP polarized) as a function of the sum frequency of near IR and 800 nm beams[66]. This analysis effectively removes intensity fluctuation of the near IR beam as it being tuned to different center frequency (see SI). The SFG intensity ratio is directly correlated to $\left|x_{eff}{}^{(2)}\right|^2$ of the P3HT/Si interfaces. As we discussed below, although there are no resonant absorptions for the incoming pulses, the emitted SFG signal can be reabsorbed by the bulk materials. Therefore, we normalized the ESFG signal by the transmission spectrum of the P3HT to remove effects from reabsorptions.

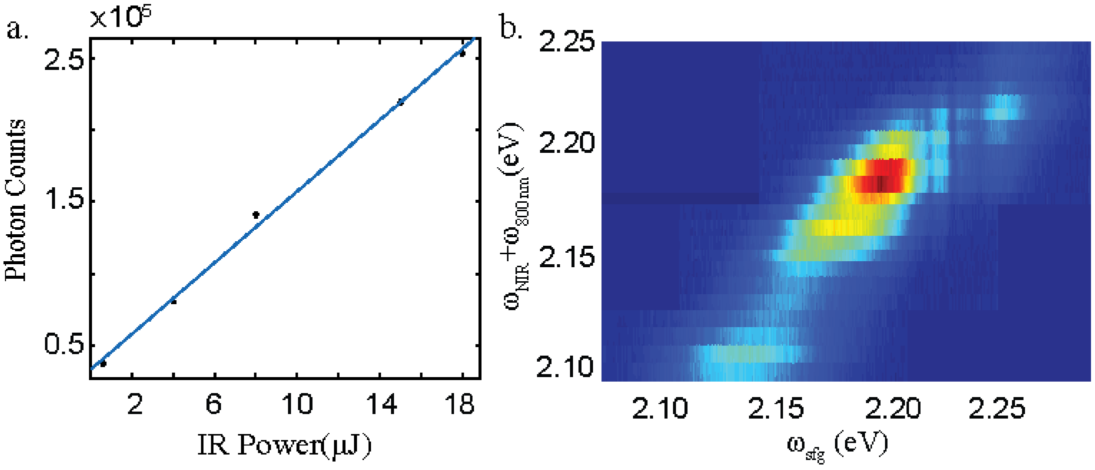

Figure 3-5. ESFG signal as a function of near IR wavelength and power. (a) The ESFG signal depends on the IR power linearly, which agrees with Eq. 3.1. (b) 2D plot of ESFG signal as a function of sum of incoming beam frequencies.

For RRE P3HT/Si sample, ESFG signals peak at 2.2 eV (Fig. 3-3b) and the signal is enhanced by 80%. Similar enhancement is seen in a previous SHG study on organic field-enhanced-transistor (OFET) composed by P3HT.[98] This enhancement is well above the instrumental uncertainty of our measurement (± 20% fluctuation of the ratio between two nonresonance SFG signals from GaAs and gold surfaces, see Fig. 3-3a). We note that there is another small 20% enhancement at ~2.12eV, since it is on the margin of the instrumental uncertainty, we decide not to focus on this peak in details.

As shown in chapter 3.2, the spectrum in Fig. 3-3b measures $\left|x_{eff}{}^{(2)}\right|^2$, which possesses many terms, including the electronic resonance and nonresonance terms of P3HT. Moreover, since the sum frequency of the two input pulses are well above the band gap of Si, which has continuous density of states, there should be a contribution $x_{Si}{}^{(2)}$ from the Si surface as well. Therefore, the measured spectrum should be fitted by[81],

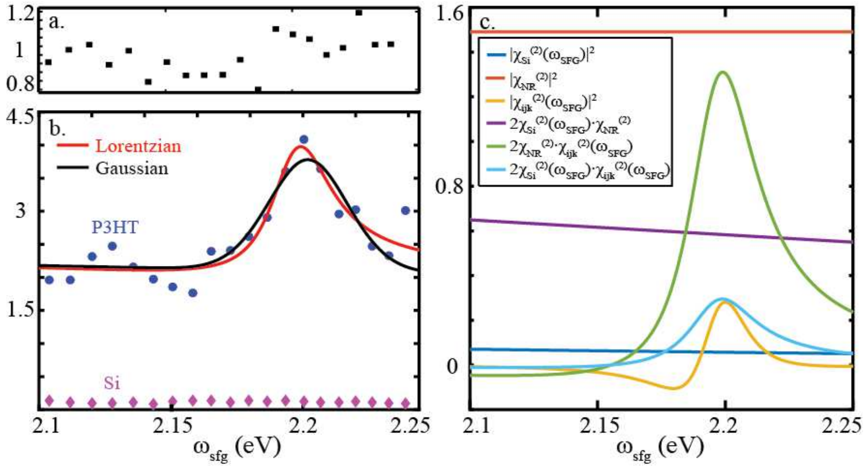

Figure 3-6. ESFG intensity as a function of the sum frequency of incoming photons. (a) normalized intensity ratio between two nonresonant ESFG signals from GaAs and Au surfaces, which represents the noise level of the measurement. (b) normalized ESFG intensity ratio between P3HT/Si and Au. More than 80% of signal enhancement is seen at 2.2 eV. The RMSE of Lorentzian fit is 0.23 and is 0.33 for the Gaussian fit. (c) curve fitting breakdown of (b).

$$\left|x_{eff}{}^{(2)}\right|^2 = \left|x_{NR}^{(2)} + \sum_n x_{ijk,n}^{(2)}(\omega_{SFG}) \cdot e^{i\cdot\varphi_n} + x_{Si}^{(2)}(\omega_{SFG})\right|^2 \tag{3.3}$$

With at least three unknown x terms, it is difficult to get unique fittings. However, we can independently determine $x_{Si}^{(2)}(\omega_{SFG})$ by measuring and fitting the ESFG spectrum of Si surface (Fig. 3-3b). We fit the spectrum by a linear function, since the corresponding UV-Vis absorption of Si is approximately linear. Then $x_{Si}^{(2)}(\omega_{SFG})$ becomes a known parameter in eq 3.3. Since $x_{NR}^{(2)}$ is a constant, the fitting procedure is significantly simplified and more reliable. We can use one Lorentzian function as the $x_{ijk}^{(2)}(\omega_{SFG})$ term to fit our data well. The center of the Lorentzian is 2.199±0.004 eV, with fwhm to be 0.014±0.006 eV and phase to be 83±16°. Therefore, it indicates only one electronic transition of P3HT is observed at the interfaces.

To understand the fitting result, we breakdown the fitting curves and plot them in Fig. 3-3c. Overall, terms that give rise to the peak around 2.2 eV are cross terms $x_{NR}^{(2)} \cdot x_{ijk}^{(2)}(\omega_{SFG})$ and $x_{Si}^{(2)}(\omega_{SFG}) \cdot x_{ijk}^{(2)}(\omega_{SFG})$ and the intensity term $\left|x_{ijk}^{(2)}(\omega_{SFG})\right|^2$. All three terms peak at the same position. The leading term that contributes to the lineshape is $x_{NR}^{(2)} \cdot x_{ijk}^{(2)}(\omega_{SFG})$. This term has an absorptive lineshape, not a dispersive lineshape, because the phase difference between the P3HT resonant and nonresonant signals is close to 90°. The term $x_{Si}^{(2)}(\omega_{SFG}) \cdot x_{ijk}^{(2)}(\omega_{SFG})$ has similar lineshapes, because $x_{Si}^{(2)}(\omega_{SFG})$ is close to constant. The intensity term $\left|x_{ijk}^{(2)}(\omega_{SFG})\right|^2$ contains a small dip at 2.18 eV. Nevertheless, it is only < 10% than $x_{NR}^{(2)} \cdot x_{ijk}^{(2)}(\omega_{SFG})$ and therefore, does not cause large lineshape changes. The rest of terms are almost all constant, which contribute to the large offset in the ESFG spectrum. Overall, from the fitting we can conclude that there are no significant interferences among the P3HT nonresonant, resonant signals and Si signals that cause lineshape distortions in the spectrum.[81]

Another possibility is to fit the peak into a Gaussian, which indicates that the electronic transition is inhomogeneously broadened. We replaced the Lorentzian function with a Gaussian and used it to fit the data. The fitting result well match the bandwidth but failed to reproduce the sharp peak at 2.2 eV. Therefore, we conclude that Lorentzian can reproduce the lineshape better than Gaussian, which agrees with the root-mean-square-error (RMSE) of the two fitting functions.

3.4 Discussion of Two Interfaces Scenario

It is possible there are two interfaces in the P3HT/Si samples that could contribute to the ESFG signals: the P3HT/Si and P3HT/air interfaces. We conclude the measured spectra are mainly contributed from the P3HT/Si, or even if the P3HT/air interface contributes a weak signal, its peak position is coincident with the P3HT/Si signal, for the following reasons. From a Fresnel factor calculation (see Appendix A.1), we show that the ESFG electric field from P3HT/Si interface is 7 times of the one from the P3HT/air interface. Since the signal is homodyne detected, the ESFG signal from P3HT/Si is more than 50 times larger than the P3HT/air signal. In principle, there should be cross-term between the signals from P3HT/Si and P3HT/air, which would lead to interference on the measured spectrum. Since only one peak is observed in the ESFG spectrum, it is either that the signal from P3HT/air is even smaller than we estimate here and therefore do not contribute to the measured signal or it has similar spectral peak and shape, which does not complicate ESFG spectrum. This conclusion also agrees with many previous vibrational

SFG works on similar P3HT/solid samples, which concluded that the signal are dominated by the P3HT/solid interfaces.[42,43,45,99,100]

3.5 Different Electronic Structure Between Interface and Bulk

The ESFG spectrum appears to be significantly different from the corresponding UV-Vis spectrum (Fig. 3-4) which probes the entire P3HT molecules in the bulk thin films. There are at least four peaks in the UV-Vis spectra. The first three are from various inter/intramolecular interactions or vibronic modes[101,102], where the long tail beyond 2.3 eV is attributed to oligomers that have short exciton delocalization[101]. Furthermore, all peaks are fitted into Gaussian lineshapes with fwhm between 0.14 to 0.30 eV (see Appendix A.2), which indicates each peak is also inhomogeneous broadened. The fact that UV-Vis spectrum needs to be fitted into multiple broad Gaussian peaks indicates that there are a few different electronic structures of P3HT in bulk.

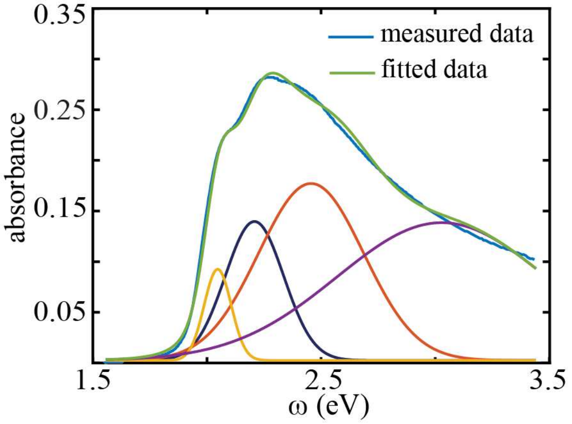

Figure 3-7. UV-Vis spectrum of the RRE P3HT film on sapphire. UV-Vis probes the bulk electronic structures of the P3HT, which is fitted into four Gaussians, indicating structural inhomogeneity. The position and fwhm (in parenthesis) of the four peaks are 2.041 ± 0.002 eV (0.14 ± 0.08), 2.202 ± 0.007 eV (0.30 ± 0.03), 2.45 ± 0.03 eV (0.55 ± 0.05) and 3.02 ± 0.04 eV (1.08 ± 0.07), respectively.

On the contrary, the single peak in ESFG is a clear indication that only one conformation dominates at the interface (there is also no peaks between 2.4 and 2.6 eV, see Appendix A.4). Furthermore, the narrow Lorentzian lineshape indicates that this electronic structure at interfaces does not subject significant inhomogeneous broadening, and the main lineshape broadening should be from electronic dephasing.

All of the ESFG spectral features indicate that the P3HT molecules have uniform electronic structures at the P3HT/Si interfaces, regardless the complexity of the P3HT electronic structures in the bulk. The uniform electronic structure distribution of P3HT on the Si interfaces indicates that order structures, such as crystallization, are formed at the interfaces. This ordered structure can allow the charges delocalized[91] on the interfaces and also increase the carrier mobility in the two-dimensional plane.[103] Several previous results have pointed out extra delocalization can promote the charge separation at the interfaces.[47,104] Furthermore, it has been shown that ordered structure at interfaces can prevent geminate recombination[91] and mitigate bimolecular charge recombination.[105,106] Therefore, all of these effects from ordered interfacial structures could lead to an increase in the short-circuit current, which improves the efficiency of the photovoltaics.

3.6 Summary of the Chapter

Our study demonstrates that the electronic structure measured from bulk thin film is not a good approximation to the electronic structures of interfaces. This finding agrees with previous works done on metal/metal oxide interfaces in vacuum[57,58], and suggests that the difference between bulk and interfaces is a ubiquitous phenomenon in many solid/solid interfaces. Therefore, interfacial specific methods need to be utilized to study buried interfaces under atmosphere.

Finally, we would like to emphasize that our approach of ESFG is robust for various sample conditions and the ESFG spectra interpretation is straightforward. First, by using two photon absorptions to reach the electronic states, we circumvented any distortions due to one photon absorption[72] of the input pulses from the bulk materials. For instance, for any SFG involved one photon absorption-like resonance, the incidence beams spectra can be distorted by absorption of the bulk materials. As a result, phantom peaks can be created.[107] In our two-photon-absorption like resonance ESFG, neither of the incident pulse is absorbed by the bulk layer, and therefore largely mitigates the necessity to use ultrathin bulk materials in the experiments. The sample still needs to remain thin to avoid the reabsorptions of the emitted SFG signal, which could be on resonance with the bulk materials. Second, we simplify the spectroscopic interpretation by avoiding any vibrational resonances. By purposely using non-resonance near IR beam as one of the two excitation beams, spectral phase twists are avoided, which exist when both electronic and vibrational resonances are met in SFG[72,108].

In conclusion, we for the first time demonstrate that electronic sum frequency generation can determine the electronic structure of organic polymers at buried solid/solid interfaces. Since the optical beams have a long penetration depth, and do not require special conditions such as UHV, we anticipate broad applications of the electronic sum frequency generation spectroscopy to many complex buried interfaces, especially at the device working conditions in the near future.

Chapter 3, in part, is a reprint of the material as it appears in Yingmin Li, Jiaxi Wang, Wei Xiong. *"Probing Electronic Structures of Organic Semiconductors at Buried Interfaces by Electronic Sum Frequency Generation Spectroscopy".* The Journal of Physical Chemistry C, 119(50), 28083-28089. The dissertation author is the first author of this work.

Chapter 4 Ultrafast Direct Electron Transfer at Organic Semiconductor and Metal Interfaces

The ability to control direct electron transfer can facilitate the development of new molecular electronics, light-harvesting materials and photocatalysis. However, it has been rarely reported and the molecular conformation-electron dynamics relationships remain unclear. Here, we describe direct electron-transfer at buried interfaces between an organic polymer semiconductor film and a gold substrate, by observing the first dynamical electric-field-induced vibrational sum frequency generation (VSFG). In transient electric-field-induced VSFG measurements on this system, we observe dynamical responses (<150 fs) that depend on photon-energy and polarization, evidencing that electrons are directly transferred from Fermi level of gold to LUMO of organic semiconductor. Transient spectra further reveal that, although the interfaces are prepared without deliberate alignment control, a sub-ensemble of surface molecules can adopt conformations for direct electron transfer. DFT calculations support the experimental results and ascribe the observed electron transfer to a flat-lying polymer configuration in which electronic orbitals are found to be delocalized across the interface. The present observation of direct electron transfer at complex interfaces as well as the insights gained into the relationship between molecular conformations and electron dynamics will have implications for implementing novel direct electron transfer in energy materials.

4.1 Introduction

Electron-transfer is of heightened interest in many energy materials, such as molecular electronics, light-harvesting and photocatalysis [32,48,109–119]. At an interface between two materials, electron-transfer can be stimulated by incident light or electrons in one step or in multiple steps [32,48,109,113–120]. Most of electron transfer involve intermediate states and multiple steps, including initial excitation, charge or exciton migration, and charge separation. As opposed to this multi-step scenario, a direct interfacial electron transfer can vertically excite charges from their initial electronic states at donor molecules to the unoccupied electronic states of acceptors, such as charge transfer states, in a single step [40,111,116,121–125]. Direct interfacial electron transfer is similar to an intramolecular electronic transition, such as metal-to-ligands charge transfer (MLCT) in organometallic compounds, but direct interfacial electron transfer occurs between molecules. Because direct interfacial electron transfer is a one-step light-matter interaction, which avoids charges propagating in space before separating at interfaces, it is more advantageous in catalysis [126,127], solar energy materials [110,117,128,129] and molecular electronics [130]. For example, by using light at a certain wavelength to excite electrons directly from substrates to specific electronic states of surface adsorbates, chemical groups and reactions can be selectively activated in photocatalysis [126]. In another example, by directly promoting charges to acceptor molecules in solar cells, unwanted competing processes, such as charge recombination and relaxation in bulk phases [32,48,121,131,132] can be mitigated.

To the best of our knowledge, direct electron-transfer was first reported at the interface of metal adatoms and semiconductor electrodes, by Gerischer and co-workers [122]. Subsequent studies over the next two decades have extended to CO and metal interfaces [40,123], C_6F_6 and metal interfaces [133] and type II quantum dots [121]. It remains an open question to determine the extent of direct electron transfer at complex interfaces of energy materials, in which interfacial molecules are not optimized for electronic coupling [110,117,126,128,129], which consist of molecules that are not optimized for interfacial electronic coupling. In addition, a deep understanding of molecular conformation-charge dynamics relationships is necessary for applying this novel charge transfer pathway broadly in energy applications. The challenges of detecting direct interfacial charge transfer in complex interfaces is two-fold: First, complex interfaces where direct charge transfer might occur are hidden in bulk materials. It is difficult to selectively probe these hidden interfaces using techniques such as two-photon photoemission spectroscopy. Second, strong electronic coupling at interfaces is necessary for facilitating direct interfacial charge transfer. Thus, direct interfacial charge transfer has been only experimentally demonstrated on interfaces between small atoms/molecules and metals [40,122,123]. These systems require careful preparations of molecular monolayers to optimize the interfacial electronic interaction, and thus have limited application to real energy materials. One recent novel exception was shown by Lian and co-workers who demonstrated a plasmon-induced metal-to-semiconductor interfacial charge transfer transition pathway by taking advantage of surface plasmonic resonance [111,116]. This new pathway relies on synthesized nanoplasmonic materials. Ideally, to implement direct interfacial charge transfer in energy materials, it is critical to understand whether direct charge transfer exists broadly in complex interfaces of energy materials, even if without the aids of well-controlled surface plasmon or interfacial electronic coupling.

4.2 Experiment Method

Here, using a combination of advanced transient vibrational sum frequency generation (tr-VSFG) spectroscopy [134,135] and theoretical calculations, we present the first spectroscopic evidence of direct electron-transfer at complex polymer/metal interfaces in realistic conditions and further understand molecular conformation-charge dynamic relationships. We focus on interfaces between organic polymer semiconductor and metal, in which the interfaces are fabricated by simple solution-phase spin coating process. Using tr-VSFG, we selectively probe molecular conformation and dynamics at hidden interfaces between organic semiconductor and metal. We observe the first dynamical electric-field-induced VSFG signals, corresponding to direct interfacial electron transfer from metal to organic semiconductor. Furthermore, we resolve two simultaneous interfacial electron dynamics with distinct VSFG spectra: one corresponds to fast charge relaxation, while the other reflects interfacial charge transfer. This suggests that a subensemble of molecules at the interface undergoes direct electron transfer. The experimental observations are supported by density functional theory (DFT) calculations that demonstrate electron delocalization exists when organic semiconductors lie parallel to metal surfaces. This result indicates that although organic semiconductor molecules are deposited without controlling alignments, a portion of the molecules still adopts conformations that make the delocalized π orbitals interact strongly with metal substrates and facilitates direct interfacial electron transfer. The presented result shows that is not necessary to have perfectly controlled alignment for direct interfacial charge transfer, which implies that such a charge transfer mechanism be a viable pathway in many solution-phase processed materials, such as organic photovoltaics and flexible optoelectronics.

The interfaces between organic semiconductor Poly(3-hexylthiophene-2,5-diyl) (P3HT) and gold are studied by spin-coating P3HT solution onto a sputter-coated gold substrate. P3HT is an organic polymer material in which electron orbitals are delocalized through thiophene units, with a band gap of 2 eV. P3HT/gold interfaces are frequently used in molecular electronics [45,136], organic light emitting diodes [98,137], organic field effect transistors [42] and solar materials [110]. When P3HT and gold are in contact, the gold Fermi level is 0.5 eV above HOMO and 1.5 eV below LUMO of P3HT (Fig. 4-1b), determined by ultraviolet photoelectron spectroscopy (Appendix B.1), and it is consistent with previous results [27,138–141]. The band energy level rearrangement maintains charge neutrality on both sides of the interface [27,130,140,141]. Theoretically, this band alignment should create new charge transitions between gold Fermi level and electronic states of P3HT, thereby promoting electrons from gold to the LUMO of P3HT or from HOMO of P3HT to gold.

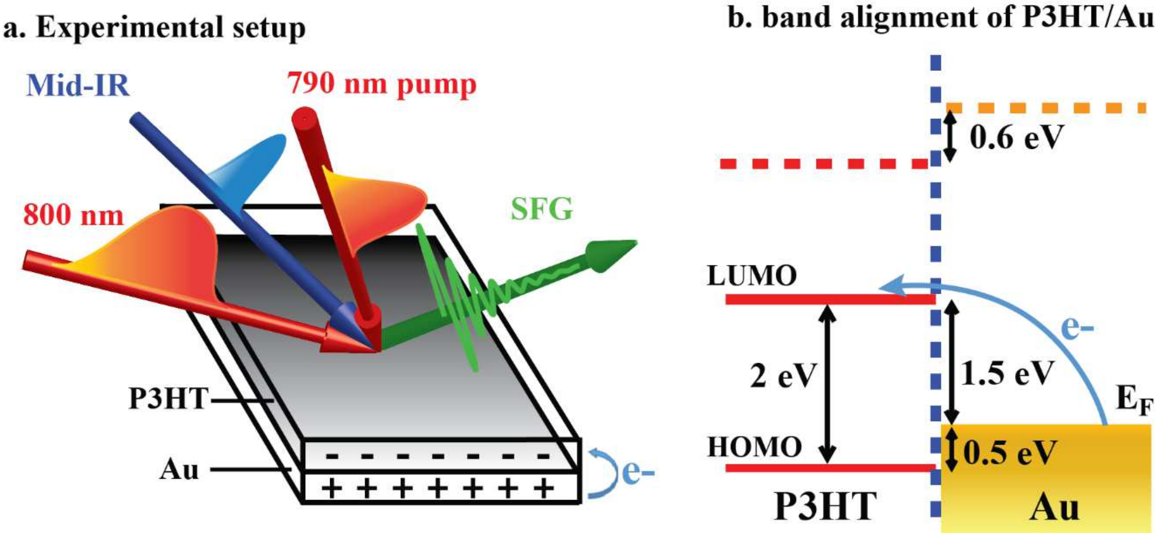

Figure 4-1. tr-VSFG spectroscopy on P3HT/gold interfaces. (a) experimental setup. (b) band alignment between P3HT and gold when they are in contact with each other. The blue arrow indicates the direct charge transfer pathway.

To investigate any new interfacial electron transfer transitions, and to understand molecular conformation-charge dynamics relationships, we implement tr-VSFG spectroscopy on P3HT/gold interfaces as described in chapter 2.3. Tr-VSFG spectroscopy is sensitive to interfacial charge dynamics and molecular conformations. It is composed of a 50 fs, 790 nm (1.57 eV) pump pulse to initiate electron excitation, and a vibrational sum frequency generation (VSFG) pulse sequence to probe molecules and charges at interfaces.

(Fig. 4-1a) The pump pulse fluence is set low enough that only one-photon absorption occurs (<20% of interfacial molecules are excited). VSFG is intrinsically sensitive to molecules at non-centrosymmetric systems, such as interfaces [42,142–144]. Furthermore, like second harmonic generation (SHG) [32,98,145–148], VSFG should be sensitive to interfacial charge dynamics through the "electric-field-induced effect" [42,142,144]. In this experiment, the IR frequency is set about 3000 cm^{-1} to probe the CH_2 and CH_3 stretches of P3HT sidechains. These vibrational modes are probed (instead of the thiophene ring modes) because the C-H stretches are not part of the conjugated π systems and, therefore, should only be influenced by electric fields at interfaces and not by electronic structure modifications associated with charge excitation. Each tr-VSFG spectrum is obtained by taking the difference of VSFG spectra when the pump pulse is switched on and off, which removes any intrinsic dipole electric field effects [138]. To avoid sample damage, all samples are studied in a sealed sample cell, purged with N_2 gas, and samples are rastered between each scan.

4.3 Dynamical Electrical Field Induced VSFG Reveals Interfacial Electron Transfer

The tr-VSFG spectrum of P3HT/gold interfaces shows distinct time-dependent dynamics. (Fig. 4-2a) First, the tr-VSFG spectrum becomes negative at t=0, and recovers to a positive signal within 1 ps. It stays positive and decays slowly (~2 ns). Second, the tr-VSFG spectra have different spectral shapes at early (< 200 fs) and larger (> 1000 fs) time delays. Both features encode information of ultrafast electron transfer dynamics and molecular conformations at interfaces. In the following, we first focus on understanding the origin of overall dynamics, and then further analyze the physical process associated with spectral shifts (Fig. 4-2b).

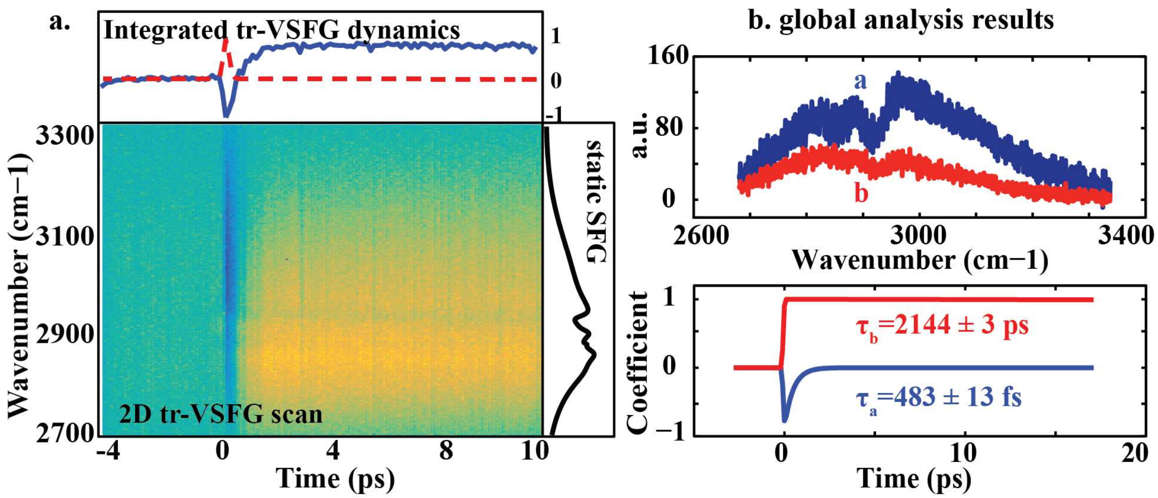

Figure 4-2. (a) pseudocolor tr-VSFG spectrum. A negative signal is observed at t = 0, which recovers very fast and becomes a positive peak at t > 0. Peak maximum shifts from high frequency to low frequency. Top: integrated tr-VSFG signal (blue) and response function (dashed red), right: linear VSFG spectrum. (b) global analysis results. Two simultaneous charge dynamics are observed as shown in the lower panel. a and b in the upper panel represent the two spectral components corresponding to the two dynamics in the lower panel (details refer to Chapter 4-5).

To understand the nature of this dynamic signal, tr-VSFG spectroscopy is performed on two control samples, bare gold surface and P3HT/SiO_2/gold, at the same pump fluence used for P3HT/gold interfaces. We find both control experiments show dynamics that are very different from the dynamics of P3HT/gold interfaces. (Fig. 4-3a) The dynamic trace of gold surface is featureless, indicating that there is no strong change in the refractive index of gold surface that can result in tr-VSFG signals. The dynamic scan of P3HT/SiO_2/gold also shows a flat trace within noise levels, consistent with two conclusions. First, because SiO_2 is an insulator that prevents electron transfer between P3HT and gold, this result confirms that the transient signal of P3HT/gold requires P3HT to be in electrical contact with gold. Second, the fact that no dynamics in P3HT/SiO_2/gold systems is observed at low pump power indicates that multiphoton excitation processes, such as a bandgap excitation of P3HT through two-photon absorption, does not occur at low pump fluence. We confirm that the P3HT in the P3HT/SiO_2/gold sample can be excited through multiphoton absorptions by increasing pump pulse power to 3 μJ and above; the dynamics of P3HT/SiO_2/gold at high pump fluence is very different from any dynamics discussed above, in which a negative signal with a fast hot exciton relaxation component (1.5 ps) and a slow charge recombination component are observed (Fig. B-5c) [149,150]. Thus, excitons can be created in bulk P3HT through multiphoton absorption. Conversely, at 1.4 μJ or lower pump energy, multiphoton excitation is not observed, which indicates 790 nm pump pulse interacts with samples at one-photon absorption limit when pump energy is set lower than 1.4 μJ. In addition to the control experiments discussed above, we also rule out thermal heating effects by measuring tr-VSFG signal on polymethylmethacrylate (PMMA)/gold systems. If thermal effects on gold substrate cause the observed tr-VSFG signal, similar signal should be obtained on PMMA/gold systems under the same pump fluence, but it is not observed (Fig. B-5a).

Under one-photon absorption limit, the only charge dynamic that can be initiated is interfacial electron transfer between gold Fermi level and P3HT. The origin of this charge dynamics is similar to the interfacial electric field induced effect, a phenomenon widely observed in SHG [32,42,98,142,144–148]. Zhu and co-workers [32] and Tisdale and co-workers [151] have recently observed the ultrafast interfacial electric field effect in time-resolved SHG spectra. When charges with opposite signs separate from each other at interfaces and become free charge carriers, a DC field is generated at interfaces. The DC field at interfaces can introduce additional $\chi^{(3)}$ signals to modulate second order optical signals, such as SHG and VSFG, as described in Eq. 4.1:

$$I_{VSFG} \propto \left|\chi^{(2)}E_{IR}E_{up} + \chi^{(3)}E_{IR}E_{up}E_{DC}\right|^2 \tag{4.1}$$

where, $\chi^{(n)}$ is the nth order nonlinear susceptibility, and E_{IR},E_{up} and E_{DC} are the electric fields of mid-IR, upconversion and DC fields, respectively. After charge separation, the interfacial electric field only exists within very few layers near interfaces; thereby, the modulated signal is still interfacial sensitive. The interfacial electric field effects in tr-VSFG is confirmed by the fact that the same tr-VSFG dynamics are observed, independent of whether the IR pulse frequency is tuned on and off from vibrational resonances of P3HT (Fig. B-5d), because the electric field effect should not be specific to vibrational resonance. Since electron transfer occurs only on hidden interfaces between P3HT and gold, tr-VSFG spectra can be used to exclusively probe this hidden interface. The sensitivity to hidden interfaces is further confirmed by checking the VSFG intensity at different P3HT thickness [46,152] (Appendix B.2.1). Different from SHG, when VSFG is on resonance with vibrational modes, it probes both electronic transitions through non-resonance background, and vibrational modes and molecular conformations, through resonance peaks. Hence, tr-VSFG is able to resolve charge dynamics with conformation specificities, as discussed below. The electric field induced effect has been used in VSFG under electrostatic conditions [42,142,144] to study charge accumulations of field-effect transistors and other semiconductor devices. However, this report is the first experimental observation of dynamical electric-field-induced effect of VSFG.

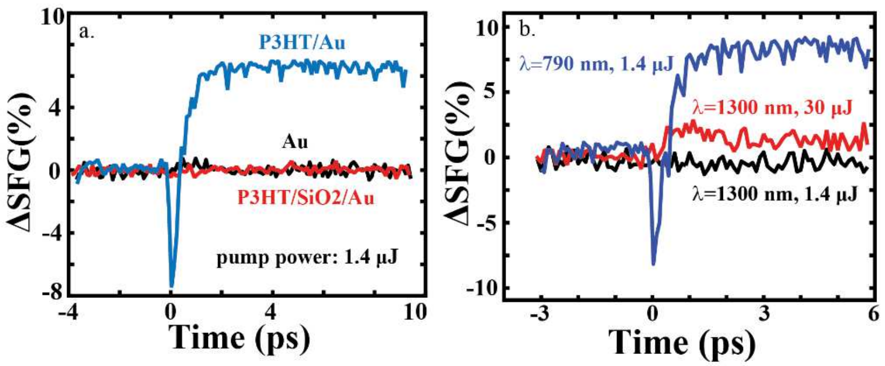

Figure 4-3. tr-VSFG dynamics of various interface samples. (a) P3HT/gold interface (blue) shows distinct dynamics from bare gold (black) and P3HT/SiO2/gold (red) sample. (b) dynamics of P3HT/gold when the interface is pumped by 0.9 eV (1300 nm) pulse. No dynamics are observed at low pump fluence (black) and similar positive dynamics are observed when pump fluence is increased (red), which enables two photon absorptions. These results suggest that charge transfer occurs from gold fermi level to the conduction band of P3HT.

The electron transfer pathway is further determined by performing tr-VSFG at a different pump photon-energy. In principle, when using a 790 nm pulse to initiate electron transfer, an electron can be lifted from either HOMO of P3HT to an unoccupied conduction band of gold, or from the Fermi level of gold to LUMO of P3HT. To differentiate these processes, an experiment is performed using a 1300 nm pulse as the pump, instead of the 790 nm pulse. In this scenario, there is no tr-VSFG dynamics observed. Only when the power of the 1300 nm pulse is increased to as high as 30 μJ to enable multi-photon absorptions do similar positive dynamics appear (Fig. 4-3b). Because the photon energy of 1300 nm light is 0.95 eV, it can only promote electrons from HOMO of P3HT to gold. Thus, the absence of dynamics in this 1300 nm pump VSFG probe control experiment indicates the tr-VSFG signal in Fig. 4-2a is solely because of electron injection from gold Fermi level to LUMO of P3HT and has no contributions from electron promotion from HOMO of P3HT to unoccupied bands of gold.

4.4 Polarization Dependence Confirms Electron Transfer Mechanism

Electrons can transfer from the Fermi level of gold to LUMO of P3HT through two possible mechanisms: First, hot electrons can be created on gold surfaces and subsequently transferred to P3HT LUMO in competition with other relaxation pathways, such as electron-electron or electron-phonon scattering; Second, electron transfer states can be directly excited across the interface of P3HT and gold [124,132,153]. Direct electron transfer transition can avoid relaxation pathways in bulk phases. In addition, direct electron transfer can selectively excite molecular orbitals, which can be used to improve selectivity in photocatalysis. Thus, understanding the mechanisms is critical to further engineering this interfacial electron transfer process.

To determine electron transfer pathway at interfaces, we examine the tr-VSFG signal's dependence on the pump pulse's polarization, a predominant method used for this purpose [123,124,153]. In hot electron mechanisms, electron transfer dynamics depend only on the absorption cross section of gold. Based on the Fresnel equations, 790 nm pulse, p polarized (perpendicular to the interfaces) pulse's absorption by gold is four times that of s polarized light (Appendix B.2.2) [153]. Therefore, if electron transfer is mediated through hot electrons, it is expected that the tr-VSFG signal will be reduced four times when pump polarization is switched from p to s polarization. On the contrary, in direct electron transfer transition mechanisms, the transition should strongly depend on polarization, because under dipole transitions, only a p polarized pump pulse can efficiently promote electron directly across interfaces from gold to P3HT layer, whereas s polarized light can only move electrons within gold layers.

The polarization-dependent results indicate that direct electron transfer transition mechanism dominates. (Fig. 4-4) When P3HT/gold interfaces are pumped by s polarized pulses at 1.4 μJ, there are no measurable dynamics, but when the same interfaces are pumped by p polarized pulses at only 0.36 μJ, distinct electron transfer dynamics are observed. Because the s polarized light used in this experiment is ~ 4 times that of p polarized light, it compensates for the differences in absorption cross-sections. However, the tr-VSFG signal intensity ratio between pumping using p and s polarized pulses is above 6, which is much larger than the ratio of 1 that would be expected for hot electron mechanism. Hence, this experimental result shows that a direct electron transfer occurs at interfaces – the p polarized pump pulse promotes electrons directly from gold Fermi level to LUMO of P3HT.

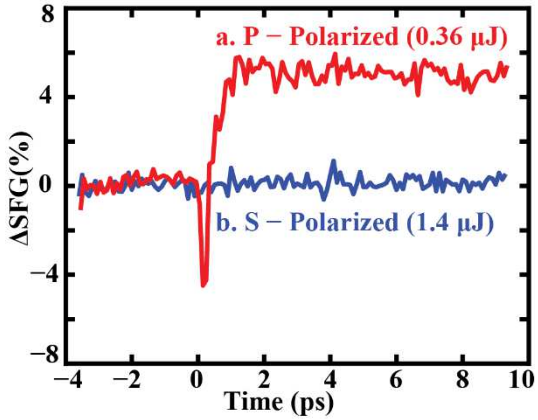

Figure 4-4. Polarization dependence on tr-VSFG. Only when pump is p polarized, large tr-VSFG signal observed. This suggests that the polarization of pump needs to be set perpendicular to the interface to lift the electron from gold to P3HT, which agrees with the direct charge transfer pathway. Pump fluence is set at 0.36 μJ when it is p polarized and is 1.4 μJ at s polarization.

4.5 Frequency-resolved tr-VSFG and DFT Reveal Conformation-Dynamics Relationship

Further insights of the excitation mechanisms are observed in the spectral shifts in tr-VSFG spectra. Using global analysis (Appendix B.2.3), the overall dynamics can be broken down into two components. (Fig. 4-2b) Component a has a negative spectral signature at t=0, and it recovers back to zero in 480 fs. Component b rises to a positive spectral signal in a time frame that is faster than the instrumental response and slowly decays (> 2 ns). These two dynamics are simultaneous and parallel processes, rather than sequential, because as component b rises, component a has not decayed. Since the dynamics of both component a and b happen exclusively when P3HT and gold are in contact with each other, these two spectral components must represent two simultaneously different electron dynamic pathways at interfaces. The decay dynamics of component a is close to 500 fs, which is longer than a coherent artifact (150 fs) [154]. Therefore, it results from a combination of coherent artifacts and other dynamics processes. This dynamics is very similar to the dynamics observed in PMMA/gold interfaces when pumped at high fluence (Fig. B-5a), in which excited electrons at interfaces can only relax quickly through electron-electron and electron-phonon scatterings [155], because the gaps between the Fermi level of gold to PMMA's HOMO or LUMO are too large for electron transfers. Thus, based on the similarity, we assign the additional dynamics of component a to be a fast relaxation pathway at interfaces, which does not lead to charge separation. Excited electrons at P3HT/gold interfaces transiently modulate the electron density of interfacial molecules and, therefore, alter the second-order molecular susceptibility, which causes the negative signal [32].

The spectral dynamics of component b is unique, since it only exists on P3HT/gold interfaces. It reflects direct interfacial electron transfer. The tr-VSFG intensity rises so fast that it is beyond the time resolution of our instrument (150 fs). This agrees with the direct electron transfer mechanism – a vertical excitation occurs and no exciton migration is involved in this process. After excitation, this set of electron-hole pairs quickly separates and forms free charge carriers within 150 fs. The free charge carriers generate interfacial DC electric fields, which induces a positive signal in tr-VSFG. After charge separation, the tr-VSFG signal relaxes in about 2 ns, confirming that interfacial charge recombination is slow. This slow recombination could be due to subsequent polaron formation [156] or screening effects [157]. The spectral shifts in component b is because of a preferred electric-field-induced signal on an electronic resonance located at the lower frequency side of the VSFG spectrum, which agrees with previous observations [42]. Based on the percentage of tr-VSFG signal, it is estimated that the transition dipole moment of this interfacial electron transfer transition is on the order of a few Debye (Appendix B.2.4), similar to many organic dyes [158]. Thus, the probability of interfacial electron transfer is not as small as previously believed.

The different dynamics of component a and b can only be detected using spectral resolved tr-VSFG data. If only the dynamics of the integrated tr-VSFG signal is measured, it is impossible to determine whether the dynamics of components a and b are simultaneous or sequential, due to their similarity. Furthermore, as discussed in detail in Appendix B.2.5, even when tr-VSFG is performed with IR frequency to be off-resonance from the vibrational modes, which is equivalent to tr-SHG, the tr-VSFG signal at off-resonance condition cannot be dissected by either global analysis or SVD into two spectral/dynamical components. This significant difference is due to the fact that, when on-resonance, tr-VSFG probes both electronic and vibrational transitions, whereas tr-SHG and off-resonance tr-VSFG are only sensitive to electronic transitions. Hence, when different conformations are perturbed by charge dynamics, the different dynamics can be directly traced back to the corresponding vibrational features, which makes them distinguishable through subtle differences in the VSFG spectra. By contrast, when the IR pulse is off-resonance, only the electronic transition is probed, which is less sensitive to molecular conformations, and thus leads to indistinguishable spectra for the two conformations, despite they exhibit distinct charge dynamics.

Since interference between various spectral components can also, in principle, induce spectral changes, we performed spectral fittings for the two spectral components to determine whether optical interference or distinct conformations are responsible for the observed global analysis components. We considered two scenarios: In scenario 1, all parameters of resonant and nonresonant signals are allowed to vary in the fitting procedure, while only amplitudes and phases of the nonresonant signal are allowed to change in scenario 2 to mimic the effect associated with optical interference between resonant and nonresonant signals [42]. We found that the two spectral components can only be correctly simulated in scenario 1. In scenario 2, only one component, in the best case, can be fitted reasonably well, while the other component one is poorly reproduced, displaying both amplitude and phase mismatches. We thus conclude that optical interference is not the dominant effect responsible for the two observed components. Indeed, it is found that, to correctly reproduce the two components, the peak positions of the vibrational modes must be slightly different in the fits to components a and b. This supports the interpretation that the two components reflect structural differences of P3HT at the interface, which, in turn, are responsible for different charge dynamics. To further determine the phase of all peaks, heterodyne detection [83,159–162] will need to be implemented, which will be discussed in chapter 5.

We note that there are two parallel electron dynamics associated with distinct VSFG spectra at interfaces, and only one of them is direct interfacial electron transfer. This indicates only molecules with some specific conformations at interfaces facilitate direct electron transfer. To understand how direct electron transfer happens at this interface and why only a sub-ensemble of molecules participates direct electron transfer, we perform DFT calculation to gain insights on the interaction of organic semiconductor molecules and gold. We place a sexithiophene (6T) molecule on top of a gold surface. 6T is an oligomer analogue of P3HT, which has similar electronic structures and makes the calculation more affordable. Two extreme configurations of 6T are modeled: parallel and perpendicular to the gold surface, and their relative distances are optimized under these configuration constraints. After optimization, the parallel configuration energy level is slightly lower by 1.1 kcal/mol than the perpendicular configuration. Considering the error of DFT in calculating energies, both parallel and perpendicular configurations and alignments in between parallel and perpendicular should be present on the surface.

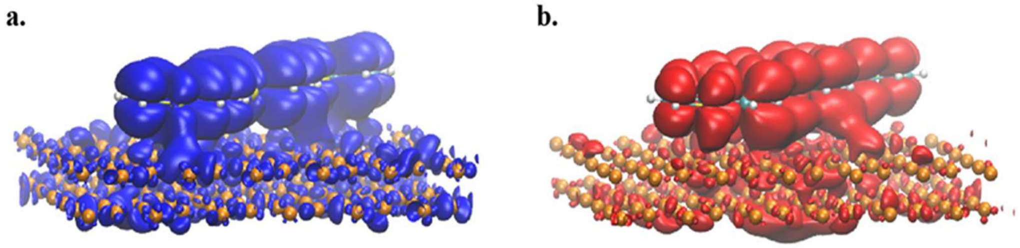

Figure 4-5. Electronic orbitals of the LUMO (a) and HOMO (b) bands of 6T/gold interfaces for parallel configuration. Both LUMO and HOMO show significant amounts of orbital delocalization to gold substrates, which enables vertical excitation at the interfaces.

However, the parallel and perpendicular orientations have drastically different electronic interactions with gold surfaces. When aligned parallel, the calculated LUMO and HOMO orbital structures of 6T have a significant amount of delocalization into gold substrates with an iso value of 0.0015 e/Å3 (Fig. 4-5). Consequently, the electron transfer transition at the interface becomes a transition between delocalized HOMO and LUMO, which subsequently undergoes fast charge separation. This strong interaction between organic conjugated molecules and metal generally exists in molecules that have π orbitals[163]. Indeed, similar direct electron transfer has been observed in molecules with small conjugation systems, such as C_6F_6[133]. Conversely, when aligned perpendicular, no orbital delocalization is observed (Fig. 4-6). Thus, when perfect control of molecular alignment is difficult to achieve, the disorder of organic semiconductor/gold interfaces serves as a practical scenario that allows direct interfacial electron transfer occurrence. When many orientations coexist on the interfaces, a sub-ensemble of P3HT is parallel or close to parallel to the gold surface allows strong electronic coupling between delocalized π electronic orbitals of P3HT and electronic bands of gold, and thus enables direct electron transfer transition occurring at interfaces.

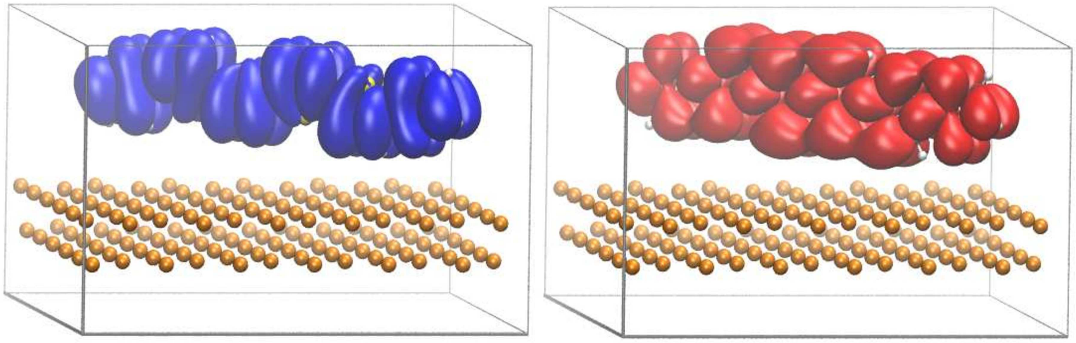

Figure 4-6. Electronic orbitals of the LUMO (a) and HOMO (b) bands of 6T/gold interfaces for perpendicular configuration. Both LUMO and HOMO show no orbital delocalization to gold substrates.

4.6 Discussion and Conclusion of the Chapter

The present experimental and calculation results agree with previous investigations of direct electron transfers on simple interfaces under vacuum condition using two photon photoemission (2PPE) spectroscopy, but the present results extend this phenomenon of direct interfacial electron transfer to complex and hidden interfaces between organic semiconductors and metals [40,122,123]. Previous studies have shown that for small molecules at metal interfaces, direct electron transfer transition can exist when strong adsorbate-substrate electronic coupling, direct chemical π bonding or coupling to image potential states exist at interfaces [123,133]. The present results indicate even for complex interfaces composed by organic semiconductor polymers with various orientations, part of surface molecules can adopt geometries that induce a substantial amount of electronic orbital delocalization into metal surfaces. Under this condition, interfacial molecules and metal atoms at the interface form delocalized HOMO and LUMO electronic orbitals and interfacial electron transfer become an electronic transition between them, followed by charge separation. This picture further confirms the advantages of direct interfacial electron transfer – this electron transfer only involves electron moving from one orbital to another orbital within the delocalized electronic structures, and does not involve any spatial charge propagations.

Furthermore, dynamic electric-field induced effect is observed for the first time in tr-VSFG, which provides a unique way to resolve multiple electron dynamics at hidden interfaces. In combination with DFT calculations, the tr-VSFG spectra can reveal molecular conformation-charge dynamics relationships. This technique is complementary to 2PPE, since it does not require vacuum conditions and can be explicitly sensitive to the interfaces where charge separation occurs. Thus, electron transfer interfaces that are close to the device working environments or at liquid/solid interfaces can be explored in the future. One caveat is that we cannot determine absolute molecular orientations directly from VSFG measurement of vibrational modes of P3HT sidechains, because the sidechains are flexible. P3HT orientation at interfaces can be measured by probing ring-mode of thiophene backbones, but the interpretation of tr-VSFG spectra of thiophene backbone is more complicated, because besides electric field induced effects, the tr-VSFG spectra of thiophene can also be affected by changing of oxidation states, after interfacial charge transfer occurs. However, this caveat might not exist for other molecular interfaces. We notice that the observed dynamics does not involve surface plasmon polariton, because the momentum-energy conservation between photon and surface plasmon polariton cannot be satisfied in our current experimental condition [164]. However, interfacial dynamics induced by surface plasmon polariton using gratings or prism geometry can be studied using the method presented here. Lastly, the overall efficiency of charge transfer of this complex interface is not as high as that observed in other nanomaterials [116,121]. Yet, it could be enhanced by optical engineering, e.g., using mesoscopic framework [165] to prepare interfaces with larger surface area, or using hyperbolic metamaterials [166] to enhance charge transfer rate.

In conclusion, by detecting the first transient electric field induced VSFG spectra, it was shown that direct metal-to-organic molecule electron transfer could occur on complex interfaces prepared by solution phase spin-coating process. This observation is consistent with previous measurements on spin-coated organic semiconductor heterojunction materials, which inferred that a sub-band gap transition direct electron transfer could occur at interfaces[118,167,168]. In addition, the strong dependence of direct interfacial charge transfer to light polarization could enable new polarization-selective detectors. Thus, the demonstration of direct photon-initiated electron transfer at more complex interfaces will open the potential to broadly apply this mechanism in artificial energy materials, selective photo-catalysis and substrate-mediated coherent control.

Chapter 4, in part, is a reprint of the material as it appears in Bo Xiang,* Yingmin Li,* C. Huy Pham, Francesco Paesani, Wei Xiong. "*Ultrafast direct electron transfer at organic semiconductor and metal interfaces*". Science advances, 3(11), e1701508. The dissertation author is the co-first author of this work.

Chapter 5 Revealing Molecular Response to Interfacial Charge Transfer

In the previous chapter, a novel charge transfer pathway, direct interfacial charge transfer is demonstrated using tr-VSFG spectroscopy. One remaining but important question is how to determine the molecular response to interfacial charge transfer. In this chapter, a new technique is introduced to disentangle different contributions to the transient charge dynamics. Heterodyne detected transient vibrational sum frequency generation (HD tr-VSFG) spectroscopy is implemented to probe transient electric fields caused by interfacial charge transfer at organic semiconductor and metal interfaces. The static and transient VSFG spectra are composed of both non-resonant and molecular resonant responses. To further disentangle both contributions, we apply phase rotation to make the imaginary part of the spectra be purely molecular responses, and the real part of the spectra be dominated by non-resonant signals. By separating non-resonant and molecular signals, we can track their responses to the transient electric-fields at interfaces independently. This technique combined with the phase sensitivity gained by heterodyne detection, allows us to successfully identify three types of photoinduced dynamics at organic semiconductor/metal interfaces: coherent artifacts, optical excitations that do not lead to charge transfer, and direct charge transfers. The ability to separately follow the influence of built-in electric fields to interfacial molecules, regardless of strong non-resonant signals, will enable tracking of ultrafast charge dynamics with molecular specificities on molecular optoelectronics, photovoltaics, and solar materials.

5.1 Introduction

Interfacial charge transfer is ubiquitous in photovoltaics, optoelectronics, and solar materials[32,48,113,114,119,169–171]. Yet, the charge transfer processes often occur at hidden interfaces rather than on the top surface, which makes it difficult to study the transfer process using surface techniques, such as scanning tunneling microscopy (STM), atomic force microscopy (AFM), or photoemission spectroscopy. Second-order nonlinear optical spectroscopy, i.e., second harmonic generation (SHG) and vibrational sum-frequency generation (VSFG), provides an elegant approach to probe hidden interfaces[42,45,142,152,172–175]. Its sensitivity to hidden interfaces comes from the fact that second-order nonlinear optical susceptibility only exists at non-centrosymmetric media, such as interfaces, when quadrupole and magnetic dipole contributions are negligible. In particular, VSFG probes molecular vibrational modes, which further provides molecular specificities at hidden interfaces. Since it was first demonstrated, VSFG has been a powerhouse technique for providing molecular level knowledge of a variety of interfaces, including air/water interfaces, interfaces of materials, and biological membrane systems[6,176–178].

The sensitivity of SHG or VSFG to interfacial charges could come from changes of electronic structures upon charge transfer, or, more generally, the so-called electric-field-induced effect. Electric-field-induced effect was first observed on SHG by Bloembergen, who showed SHG intensity was modulated by applying electrical potential at interfaces[148]. This intensity modulation is because a strong DC electric field is added to the interfaces, which further enables a third order $\chi^{(3)}$ signal. Because the electric field is largely screened in the bulk, the $\chi^{(3)}$ signal reflects the existence of strong DC electric fields at interfaces. Since then, electric-field-induced effects have been seen on air/liquid interfaces with ionic surfactants[179–186], and many prototype charge transfer materials[32,42,142,175]. In particular, transient electric-field-induced SHG has been demonstrated by X.Y. Zhu and co-workers[32], and static and transient electric-field-induced

VSFG has been developed by Massari[42] and our group[175], respectively. These developments provide a suite of tools to probe charge accumulation and dynamics at hidden interfaces.

Compared to SHG, VSFG should, in-principle, have the advantage of being able to follow molecular responses during interfacial charge transfers, which can provide insights into the role of interfacial molecules in many molecular optoelectronics, photovoltaics, and solar cell devices. However, as shown in both Massari's and our group's previous works[42,175], the VSFG spectra of charge transfer interfaces are often composed of both non-resonant (NR) and molecular resonant responses, and because NR signal often dominates the spectra, extracting molecular responses becomes difficult. Techniques such as adding delay between infrared (IR) and upconversion pulses could mitigate the NR signal, but add complications to the temporal dynamics.

In the rest of this chapter, we describe a new way to separate the NR and resonant VSFG signals in transient HD VSFG measurements[187,188] of charge transfer at interfaces[189], which enables separate dynamic analysis of both the NR signal and the molecular response during charge transfer events. This method is based on heterodyne detection, which measures both the phase and amplitude of the emitted VSFG signals. We focus on a prototype charge transfer system composed of P3HT and Au. These two materials undergo dipole rearrangements and create new interfacial bands, which also enables new direct charge transfer pathways at interfaces. However, the associated dynamics are somehow still complicated by NR background. Therefore, it serves as an ideal system to develop heterodyne transient electric-field-induced VSFG to extract previously unavailable knowledge on this model system.

5.2 Experimental Methods

5.2.1 Sample preparation

The P3HT/Au system is prepared by a spin coating method. Titanium layers, which serve as the adhesion layer, are first sputtered onto glass slides. Then, gold layers are deposited on top of the titanium with a thickness of 150 nm. The Au substrates are sonicated in acetone for 15 minutes followed by ozone cleaning for 20 minutes before using. Regioregular P3HT polymers (from REIKE metals) are dissolved in chloroform to obtain an 8 mg/ml solution, which is then spin coated onto the Au substrates using 1500 rpm spin speed. The P3HT/SiO_2/Au system is prepared followed the same procedure as P3HT/Au except using a different substrate, where a thin layer of SiO_2 is magnetron sputtered on the gold slice with the thickness of 50 nm.

5.2.2 Heterodyne Transient VSFG Spectrometer

The heterodyne transient vibrational sum frequency generation (HD tr-VSFG) spectrometer is based on a transient VSFG spectrometer described in the previous chapter, a detailed schematic of the setup is included in Figure 5-1. The light source is an ultrafast Ti: Sapphire regenerative amplifier (Astrella, Coherent), which outputs 790-nm pulses (~35 fs, ~6 W, 1 kHz). The 790-nm pulses are then split into two parts. The major part (~5 W) is sent into an optical parametric amplifier (TOPAS, LightConversion) to generate two tunable near-IR pulses, referred to as signal and idler pulses. The signal and idler pulses after the TOPAS are spatially and temporally overlapped onto a type I barium borate (BBO) crystal to generate a mid-IR beam at 3.3 μm (~7 μJ) through the difference frequency generation (DFG) process. The residual 790-nm beam after TOPAS is used to prepare an upconversion pulse by passing the beam through a home-built pulse shaper for near-IR that narrows the spectra of the residual 790-nm beam to 0.6 nm or 9.5 cm^{-1} at full-width at half maximum (FWHM), which determines the spectral resolution. The minor part of the 790-nm fundamental pulse (~1 W) serves as the pump beam, which passes through a variable-length delay line before hitting on the sample. The pump pulse is modulated by a shutter which is controlled by a homemade Labview program. The shutter is modulated to be on and off every 1s which gives the integration time of pump on/off spectra. The power of the pump beam is controlled by a waveplate and polarizer.

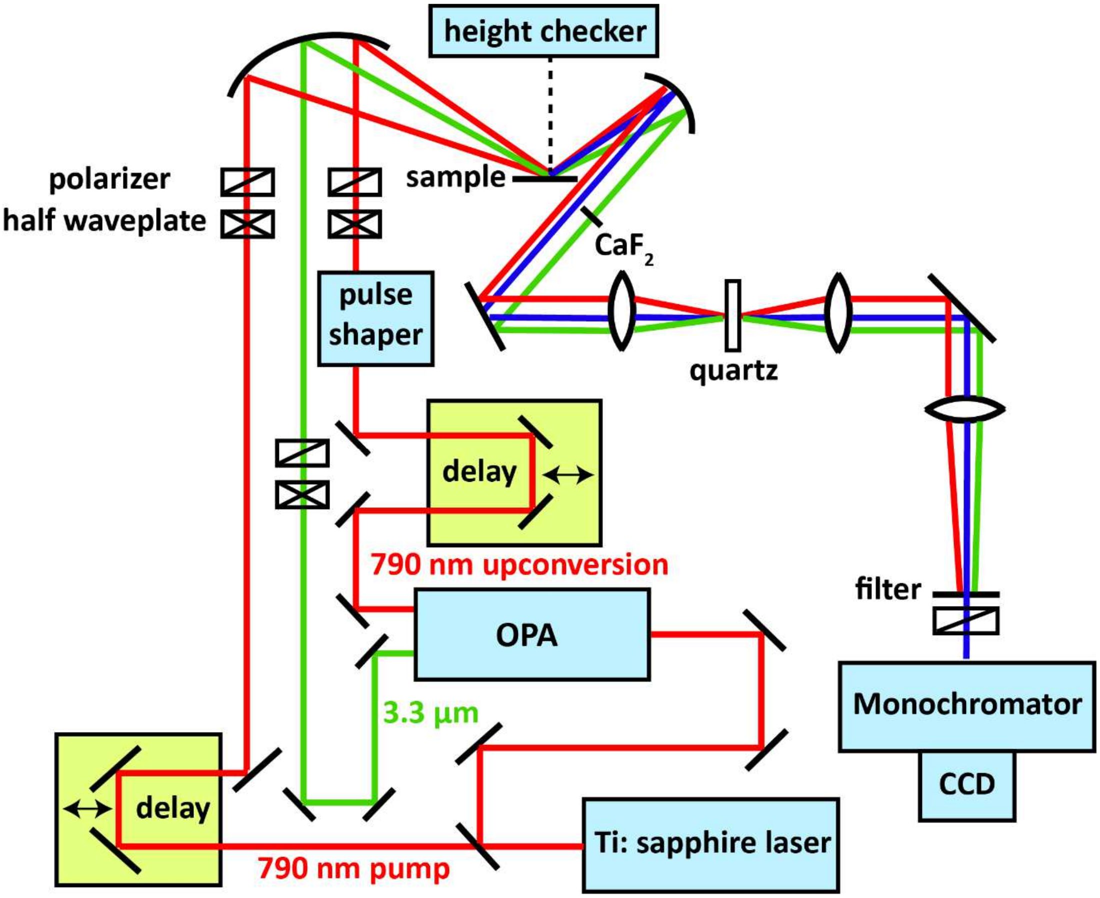

Figure 5-8. Schematic of the transient HD VSFG spectrometer setup.

The VSFG probe signal is generated by overlapping the mid-IR beam and the 790-nm upconversion beam both spatially and temporally at the sample surface. The center wavelength of the mid-IR is tuned to 3.3 μm to be on resonance with the C-H vibrational modes of P3HT. The mid-IR beam and the 790-nm beam are focused by an f = 10 cm parabolic mirror. Both beams approach the sample at about a 60-degree angle relative to the surface normal. The signal is collected by another parabolic mirror and collimated. After the beams get collimated, a piece of 2-mm thick CaF_2 crystal is added on the IR path to generate a time delay between the IR pulse and the 790-nm pulse for local oscillator (LO) generation[160,190], where a transmission geometry is implemented. Since the 790 nm upconversion pulse is long in time domain, the delayed IR would still overlap with the upconversion to generate the local oscillator. Moreover, due to the phase matching condition, it is much easier to insert delay media in the IR path. The VSFG probe, along with the other two beams, are focused by a lens (f = 10 mm) onto a Y-cut quartz crystal to generate the LO for heterodyne detection. The LO and VSFG signals are collimated by another lens (f = 10 mm) then passed through short-band pass filters to remove any 790-nm residuals, and then enter the monochromator and charge-coupled device (CCD) camera (400 X 1,340, Andor). LO and VSFG signals interfere with each other at the CCD, generating the heterodyne VSFG signal. A pair of waveplates and polarizers is used in each beam path to control both the beam intensity and polarization. The polarization configuration is kept at SSP through the whole experiment (S – SFG signal, S – 790 nm upconversion, and P – IR). The optical pump beam HD tr-VSFG signal is sent prior to the VSFG pulse sequence to trigger charge transfer. Typically, 1.4 μJ is used to pump the sample. For the transient dynamic analysis, the pump probe signal at each time step is obtained by taking the difference of VSFG spectra when the pump pulse is switched on and off. The time delay between pump and probe pulses are controlled by a computerized stage, which randomizes its position during each scan to remove the effects of systematic errors on the dynamic trace. Between each scan, a height checker is applied to make sure the sample is at about the same height (the variation is within 1 μm).

Data collection is done by home-made Labview programs and Andor-Solis software. Each data set takes 20 minutes to finish that is well within the phase stable period. All the spectra are first Fourier transformed from the frequency domain to the time domain, then window function filters are applied to remove the DC signal. An inverse Fourier transform is applied to get the interference fringes in frequency domain. The interference fringes of the samples are then phase referenced by the HD SFG signal from a flat, clean gold surface. The transient signal is obtained by taking the difference between VSFG spectra with pump on and off.

5.3 Static HD VSFG Spectra at Interfaces and Its Non-resonance Signal

Before discussing transient HD VSFG dynamics of the P3HT/Au system, we must first show the static HD VSFG spectra of P3HT/Au to examine the phase stability of our setup, the sample and spatial heterogeneity of spectral phase, and the phase of the NR signal. We tested the phase stability on both Au substrates and freshly made P3HT/Au sample. We measured HD VSFG spectra at the same spot of samples multiple times to examine the relationship between the sample condition and phase stability. We found that the phase of our phase reference, bare Au slice, remained stable for at least half an hour (Fig. 5-2a). We also observed that the phase of the P3HT/Au samples would undergo a constant decreasing due to laser illumination before reaching an equilibrium state (Fig. 5-2b). However, the phase soon reaches a constant, and during the entire process, the lineshape of VSFG spectra remain unchanged. Thus, we believe the initial phase drift is not due to sample damage, but rather to the light-induced annealing process, which is a subject for future studies. To guarantee consistency, all of our measurements are performed after the samples reach stable conditions. The phase of each measurement shows 0.02 radian variation within each measurement, which not only demonstrates the phase stability, but also indicates that P3HT does not undergo sample degradation after reaching equilibrium, as the spectral phase is very sensitive to sample quality (Fig. 5-2b).

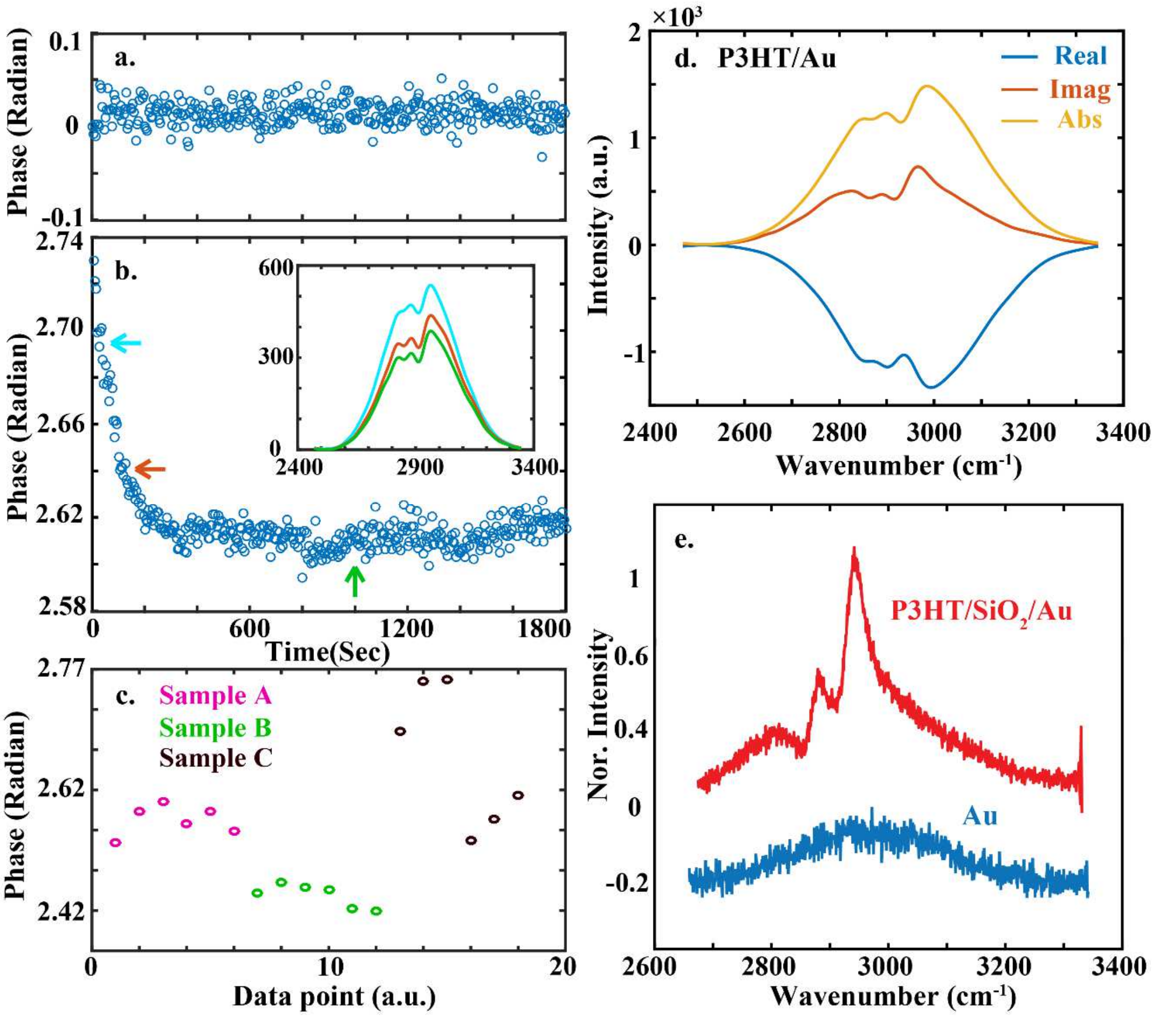

Figure 5-2. Phase stability and static VSFG spectra. (a) Phase stability of our phase reference, bare Au slide, in 30 minutes. The standard deviation is 0.0125. (b) Phase stability of P3HT/Au sample at the same spot. The inset shows three HD VSFG spectra of P3HT/Au at different times, as indicating by the arrows. Between the beginning of the scan (red) and the end of the scan (green), the spectra shape doesn't change. (c) Phase of three different P3HT/Au samples (A, B & C) prepared on three different days. Six different spots are tested for each sample. (d) Real, imaginary, and absolute HD SFG spectra of P3HT/Au sample. (e) Homodyne VSFG spectra of bare Au and P3HT/SiO_2/Au with very small non-resonant signal.

Next, we turn our attention to understanding whether there are spectral phase variations between different samples and different areas of the same sample. P3HT is a polymer and could be subject to spatial heterogeneities because of various molecular conformations at interfaces or subtle changes in sample preparation[191,192]. The result (Fig.

5-2c) suggests that different areas of the same sample do show some phase variations due to sample heterogeneity[192]. However, larger phase differences are seen between different samples because of various sample conditions. Therefore, the spectral analysis is conducted for each sample separately.

Lastly, we note that the HD VSFG spectra of P3HT/Au system have NR signals in both the real and imaginary parts (Fig. 5-2d), indicating the phase of NR signal is not $\frac{\pi}{2}$ [193], as for the bare Au surface, instead, it's 2.69. This suggests there are electronic interactions between P3HT and Au. Thus, it is different from the conventional nonresonant signal from Au. Further computational effort is underway to understand the phase shift. In addition, all spectra are taken at SSP polarization, under which only a small NR signal appears for bare Au surface and P3HT/SiO_2 (Fig. 5-2e). All this evidence indicates that by depositing P3HT onto Au, the electronic bands of both materials hybridize and form new orbitals[140], which alters not only the phase but also the polarization selectivity of NR signals. The exact origin of these changes will be explored in future studies, in combination with theoretical works. Nevertheless, the existence of NR signals in both real and imaginary parts means that NR and molecular resonance signals are still mixed together, and, thus, imposes difficulties for following molecular specific dynamics, as we show in the next section. We also want to point out that the VSFG signal we observed comes from the buried interface as we discussed in our previous publication[15], where we showed the contribution from air/P3HT interface is almost negligible.

5.4 HD Transient VSFG Dynamics

The HD transient VSFG spectra are shown in Fig. 5-3a. From the transient spectra, we can clearly see that a time-dependent spectral shift exists in both real and imaginary parts of the dynamics where the spectrum centers at a higher wavenumber around time zero and shifts to a lower wavenumber at later time delay. To further understand the dynamics, we plot the integrated dynamics of both real and imaginary HD tr-VSFG spectra (Fig. 5-3b). The sign of the real part of the spectra is flipped for comparison purposes in both Fig. 5-3a and Fig. 5-3b. The dynamics of real and imaginary HD tr-VSFG spectra show similar overall dynamic features, where both spectrums have a negative peak around time zero, then the transient signals recover and become positive. However, it is obvious that the time scales associated with the real and imaginary spectral dynamics are different, which cannot be extracted if only the dynamics of homodyne VSFG is measured. For example, the recovery dynamics of imaginary spectral dynamics is slower than the real part.

Another way to analyze HD transient VSFG spectra is to plot the phase dynamics (Fig. 5-3c). Three cuts are taken at different frequencies: 2890 cm^{-1}, 2950 cm^{-1}, and 3050 cm^{-1}, as shown in Fig. 5-3d. Using Eq. 5.1, we can fit the dynamics cut at 2950 cm^{-1} into a combination of two exponential functions and a constant. We extract two components: a fast component, which decays in 120 fs, and another component that decays in around 1.14 ps. Therefore, the phase dynamics provide extra insights into the charge transfer process.

$$y = A_1 * e^{-t/\tau_1} + A_2 * e^{-t/\tau_2} + A_3 \tag{5.1}$$

Yet, up to this point, it is still difficult to extract just the molecular dynamics involved in the charge transfer. This difficulty can be understood based on the Lorentzian model that is used for modeling VSFG spectroscopy (Eq. 5.2). It can be easily expanded to show that unless the non-resonant phase ϕ is zero, both the real and imaginary components of the VSFG spectra contain NR and molecular resonant responses. However, NR and molecular resonance could have different temporal dynamics, which convolute all dynamics together and is the origin of the difficulty we encounter here.

$$\chi_{eff}^{(2)} = A_{NR} * e^{i\varphi} + \sum A_R * \frac{1}{(\omega+\omega_R)+i\Gamma} \tag{5.2}$$

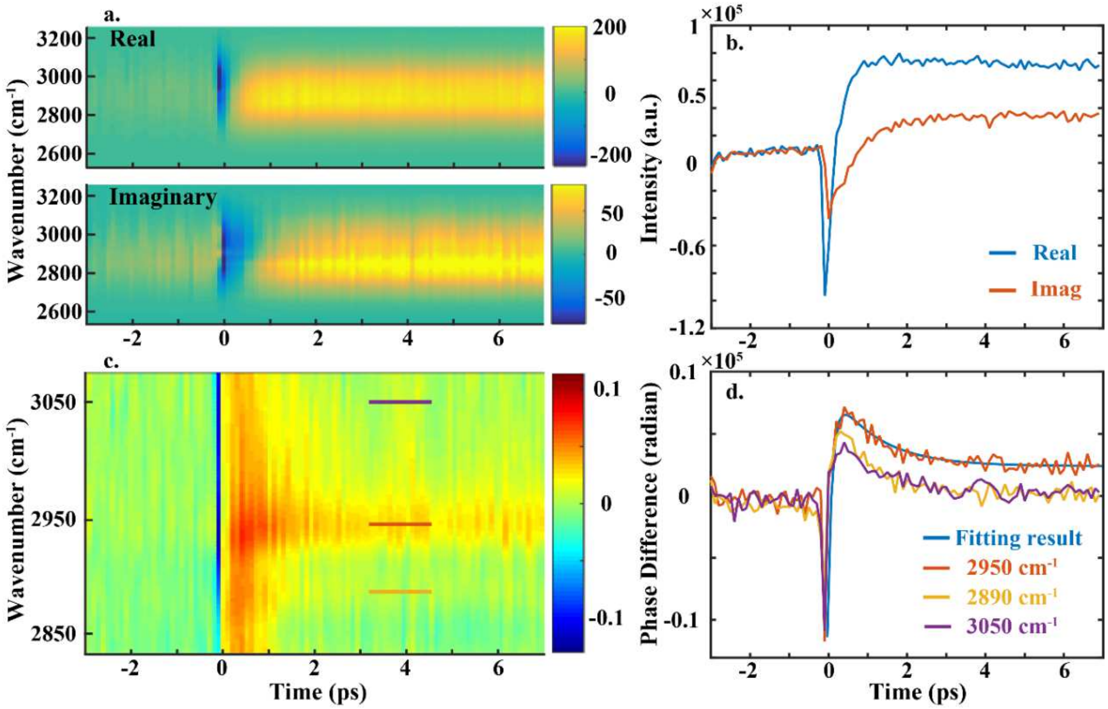

Figure 5-3. HD Transient-VSFG dynamics. (a) Pseudocolor 2D HD tr-VSFG spectrum of P3HT/Au sample. The upper panel shows the real part of HD dynamics, and the lower panel shows the imaginary part. (b) Integrated HD tr-VSFG dynamics for the real (blue) and imaginary (red) parts. The sign of the real-part spectra in both (a) and (b) is flipped for comparison purpose. Both parts show a negative signal at t=0, which recovers to a positive signal at t > 0. (c) 2D plot of the phase dynamics. The wavenumber axis is cut since the SNR of phase plot is low. Different color bar is applied from the 2D tr-VSFG spectra. (d) Cuts of phase dynamics at three different frequencies: 2890 cm^{-1} (orange), 2950 cm^{-1} (red) and 3050 cm^{-1}, as indicated by the colored lines in (c). The blue trace shows the fitting result of the cut at 2950 cm^{-1}.

5.5 Extracting Molecular Dynamics Using Phase Rotation Method

Fortunately, ϕ in Eq. 5.2 is a constant and independent of frequency. Thus, if ϕ can be determined, and a factor $e^{-i*\phi}$ is multiplied to Eq. 5.2, the NR signal can be shifted to the real component, and the molecular resonance will still have both real and imaginary components[189]. Most importantly, when the imaginary spectra are studied, they should only reflect molecular responses. The VSFG response after phase rotation is summarized in Eq. 5.3. Despite the function of the imaginary component appearing to be more complicated, the imaginary spectra can still be fitted using the same parameters of the original Lorentzian model for VSFG because ϕ is known.

$$\chi_{eff}^{(2)*} = \chi_{eff}^{(2)} * e^{-i\varphi} = A_{NR} + \sum A_R * \frac{1}{(\omega+\omega_R)+i\Gamma} * e^{-i\varphi} \tag{5.3}$$

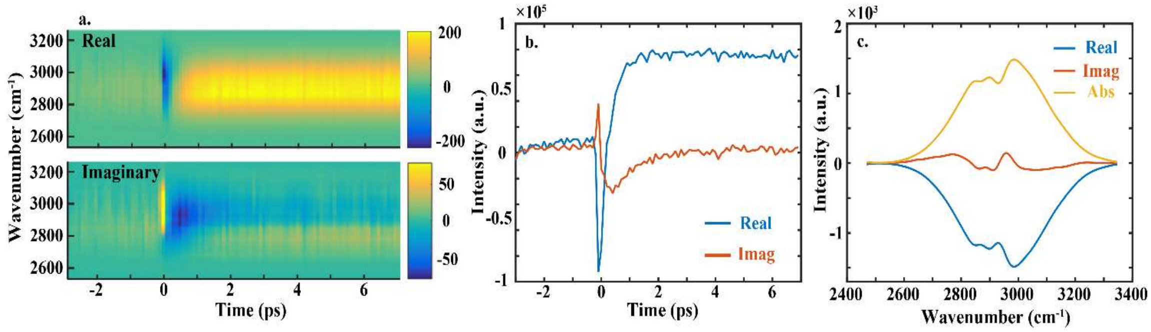

Figure 5-4. HD Transient-VSFG dynamics and static HD SFG spectra after phase rotation. (a) Pseudocolor 2D HD tr-VSFG spectrum of P3HT/Au sample after phase rotation. The upper panel shows the real part of HD dynamics, and the lower panel shows the imaginary part. (b) Integrated HD tr-VSFG dynamics for the real (blue) and imaginary (red) part after phase rotation. (c) The real (blue), imaginary (red), and absolute (yellow) static HD SFG spectra of P3HT/Au when not pumping the sample.

The phase ϕ can be determined by measuring the phase of HD VSFG spectra where there is no molecular resonance. This is a reasonable assumption, because although Lorentzian function has a long tail, NR signals often dominate the spectra, and, therefore, the spectra phase of HD VSFG is also dominated by the NR signal phase. In practice, we rotated the NR signal into negative real numbers, so it should have a phase of $\boldsymbol{\pi}$, which results in equation: $\boldsymbol{\varphi_{NR-PR} + \varphi = \pi}$, where $\boldsymbol{\varphi_{NR-PR}}$ is the phase of NR signal, $\boldsymbol{\varphi}$ is phase rotation factor. Thus, for the data of P3HT/Au, we determine ϕ to be 0.45 from the static HD VSFG spectra, for our following data analysis.

The phase-rotated HD VSFG spectra (Fig. 5-4c) show that NR signals are shifted to the real part of the spectra, whereas the molecular resonances appear in the imaginary spectra, as the imaginary spectra remain flat in the region where no molecular resonances are expected[83]. In the HD tr-VSFG spectra after phase rotation (Fig. 5-4a), it is clearly seen that the imaginary spectra intensity and lineshape evolve as a function of time, whereas in the real spectra, there is also time-dependent spectral evolution (Fig. 5-4b).

Because the spectral dynamics are clearly frequency-dependent (Fig. 5-4a), the integrated spectral dynamics can lose important insights. For example, even though there is a clear transient signal at long time delay, it appears the signal relaxes to zero in a few picoseconds in the transient imaginary spectral dynamics when integrated (Fig. 5-4b). To further extract dynamics of P3HT during interfacial charge transfer, we performed global analysis[194] on the real and imaginary parts of spectral dynamics, separately. The reconstructed HD tr-VSFG spectra from the global analysis results (Fig. 5-5a) well capture salient features of the experimental results, as indicated by the differences seen between experimental and reconstruction results (Fig. 5-5b).

Global analysis shows that both real and imaginary dynamics can be decomposed into three components (Fig. 5-6) that are simultaneous and parallel, rather than sequential. The lineshapes of the spectral components (Fig. 5-6a, b, and c) indicate that the spectral components are all dominated by NR signal except the imaginary part of component 3 (orange, Fig. 5-6c), which resembles the molecular spectral feature in static HD VSFG after phase rotation (Fig. 5-4c). What is particularly striking is that NR signals also dominate imaginary spectral components 1 and 2, which is notable considering that NR signals have been removed from the imaginary VSFG spectra after phase rotation (Fig. 5-4c). This result indicates that upon photoexcitation, new NR signals, or a phase shift of NR signals, are created. However, it is interesting that even for NR signals, two different components are introduced. For example, the phases of transient components 1 and 2 are 2.94 and -1.59, respectively.

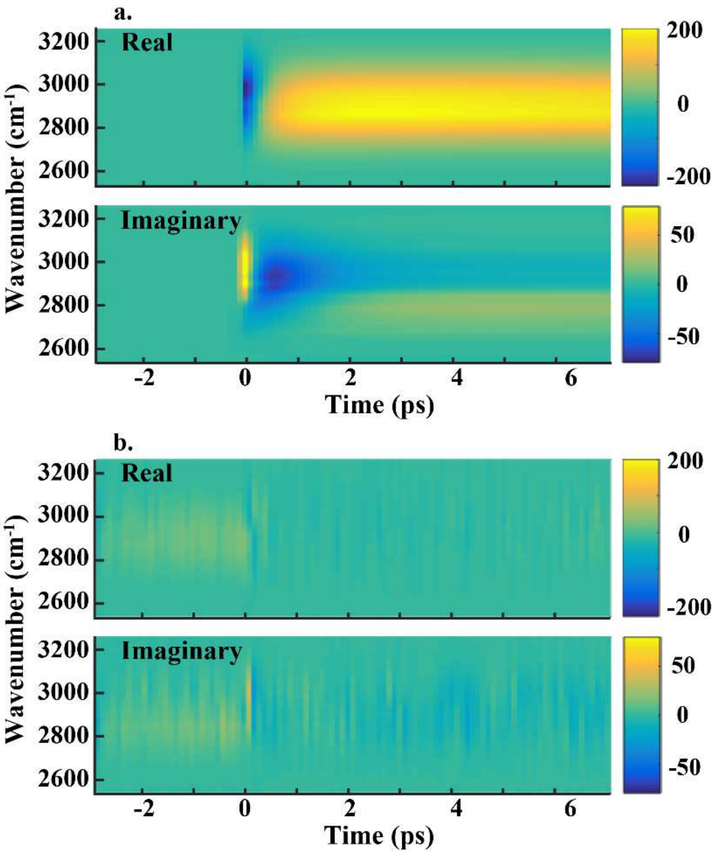

Figure 5-5. HD Transient-VSFG dynamics from global analysis. (a) Reconstructed real (upper panel) and imaginary (lower panel) 2D HD tr-VSFG spectrum of P3HT/Au from global analysis result. (b) The difference between the experimental and simulated 2D HD tr-VSFG spectrum, which shows good agreement.

Another remarkable result is the agreement between the temporal dynamics of the real and imaginary components from the global analysis, despite the fact that the real and imaginary spectral dynamics are analyzed separately. Components 1, 2, and 3 have lifetimes c.a. 250 fs, 900 fs, and 40 ps, respectively, regardless of whether the component is from the real or imaginary spectral dynamics. This consistency implies that the real and imaginary parts of each component reflect the same physical process during interfacial charge transfer. Furthermore, we note the extracted lifetime for components 1 and 2 are very close to the lifetime of the phase dynamics fitted using Eq. 5.1, which indicates that the multi-exponential phase dynamics in Fig. 5-4d is composed of two parallel dynamical processes. Note that we only scan the dynamics to 7 ps, so the 40 ps lifetime only reflect and agree with the observation that there is a long dynamic component in the charge transfer process.

Based on the time-scale, we tentatively assign components 1 to be coherent artifacts and component 2 to be optical excitations that only lead to unsuccessful charge transfer which is fast charge recombination through hot electron scattering and electron – phonon scattering[154,175]. The ca. 250 fs relaxation time of component 1 is just slightly longer than the instrumental response, but within the experimental uncertainty range. We note that components 1 and 2 together are likely to be the first component in our previous homodyne tr-VSFG work[175]. When homodyne detection is employed, it is difficult to disentangle the dynamical processes. With the additional phase measurement gained from heterodyne detection, these two dynamical processes are successfully disentangled. Thus, as a result, when homodyne detection was used, the relaxation dynamics was determined to be ca. 500 fs, which is likely to be convoluted results of the dynamics of coherent artifacts and charge relaxation[175]. Heterodyne detection provides a more accurate measurement for the charge recombination dynamics, which is ca. 900 fs.

Component 3 has a very long relaxation lifetime, matching with the direct interfacial charge transfer across the P3HT/Au interface, as we described before. It is interesting to note that the imaginary part of component 3 consists of purely resonant molecular signal, while the real part is dominated by NR signal. Nevertheless, both components have the same type of dynamics. This result suggests that both the molecule signal and the NR signal experience similar built-in electric fields upon charge transfer. This is consistent with the previous thoughts that electric-field-induced effect in charge transfer materials are dominated by NR signals[42]. However, we clearly show, using heterodyne detection, that molecular resonance features also have responses from electric-field-induced effect. The response is much smaller than the response from NR signals, but is not negligible and can only be learned with the help of HD detection. Most importantly, because we can now separate NR and molecular responses to local electric fields, and NR signal is mostly due to non-resonance electronic excitations, whereas molecular resonances represent local molecular excitations, this development augments local molecular sensitivity to build-in electrical fields. We include a cartoon (Fig. 5-6g) to better describe the physical process of dynamic component 2 and 3.

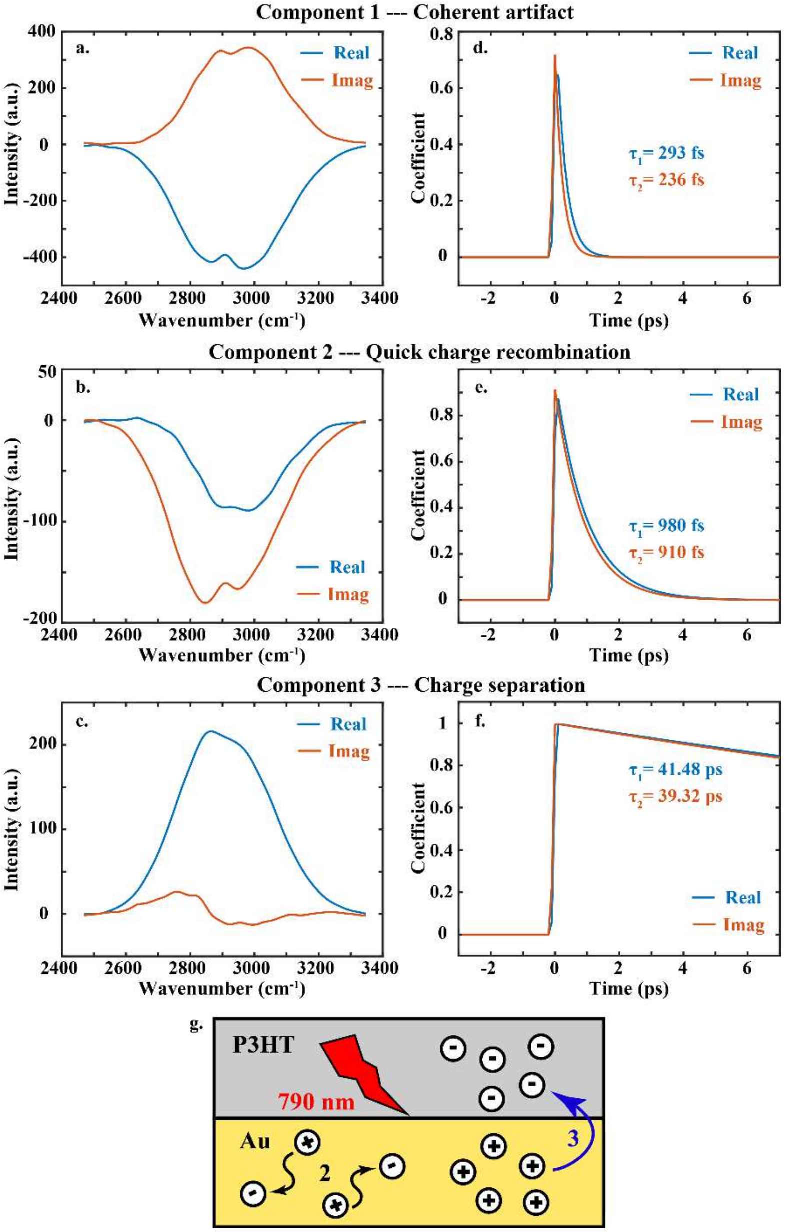

Figure 5-6. Individual plots of three different spectral components (a, b, and c) and their correspondent temporal coefficients (d, e, and f) from global analysis of the real part (blue) and imaginary part (red) of the spectrum. A schematic of dynamic component 2 and 3 is shown in g.

5.6 Summary of the Chapter

In this chapter, heterodyne detected transient electric-field-induced VSFG is demonstrated and applied to P3HT/Au interfaces. The heterodyne detection enables phase sensitivity in tracking electric-field-induced VSFG. Furthermore, to clearly resolve nonresonant and molecular resonant responses to local DC electric fields, we implemented a phase rotation scheme to rotate the non-resonant signal so that it only appears at the real part of the VSFG spectra, which ensures the imaginary parts are composed purely of molecular resonance. The separation of non-resonance and molecular resonances in VSFG, along with its phase sensitivity, allowed us to resolve three spectral dynamic components. Using heterodyne detection, we successfully disentangled coherent artifacts and ultrafast dynamics of charge relaxation/recombination, which were convoluted in previous homodyne measurements. The third component resembled the direct charge transfer dynamics revealed in our previous homodyne measurements[175], which further supports the conclusion from our previous work that two types of charge dynamics, e.g., charge recombination and direct charge transfer, happen simultaneously at P3HT/Au interfaces.

Chapter 5, in part, is a reprint of the material as it appears in Yingmin Li, Bo Xiang, Wei Xiong. "*Heterodyne Transient Vibrational SFG to Reveal Molecular Responses to Interfacial Charge Transfer*". The Journal of chemical physics, 150(11), 114706. The dissertation author is the first author of this work.

Chapter 6 Characterizing Surface Adsorbed Catalyst by 3D SFG Spectroscopy

In Chapter 2, the theory and typical setup of two-dimensional sum frequency generation (2D SFG) spectroscopy have been introduced. With the help of two-dimensional spectroscopy, we learned the information that is not accessible to linear spectroscopy techniques. In this chapter, a novel method we developed, fourth-order 3D SFG spectroscopy, will be discussed and implemented as the tool to learn the interstate vibrational coherent dynamics of a monolayer of the catalyst Re(diCN-bpy)(CO)3Cl on a gold surface. Besides measuring the vibrational coherences of single vibrational modes, the fourth-order 3D SFG spectrum also measures the dynamics of interstate coherences and vibrational coherences states between two vibrational modes.

6.1 Introduction

Interstate vibrational coherences are the superposition states of two vibrational modes[95,195] which provide pathways for redistributing energy in a fast but concerted fashion.[95,196] In particular, interstate vibrational coherences are a critical channel to control energy transfers in molecular monolayer-based materials and devices, such as surface catalysts,[197] molecular electronics[198] and biosensor chips.[199] Although interstate coherences have been observed in both vibrational and electronic states in solution phase, measuring coherent dynamics between states of a single monolayer is a difficult task because (1) the spectral signals from monolayers are usually small, and (2) the interstate coherence is mixed with population relaxation and single vibrational modes coherence, which makes it hard to be extracted.

In the following chapter, we demonstrate the first fourth-order 3D SFG spectroscopy to measure the interstate vibrational coherences from a monolayer. This technique is based off heterodyned 2D sum frequency generation (HD 2D SFG) spectroscopy[34,37,200,201], a surface sensitive 2D vibrational spectroscopy. By scanning and Fourier transform along the waiting time during the interstate coherence, t_2, we obtain 3D SFG spectra and can separate the interstate coherence spectra from other spectroscopic features that normally overlap with them in the 2D spectra. Therefore, we can precisely determine the homogeneous and inhomogeneous contribution to interstate coherence dephasing dynamics on the surface.

To demonstrate this technique we focus on a model surface bound catalyst for CO_2 reduction, Re(diCN-bpy)$(CO)_3$Cl (referred as **1**, diCN-bpy = 4,4′-dicyano-2,2′-bipyridine)[202], adsorbed on gold. The goal of this type of surface catalysis is to combine advantages of both homogenous (tenability, selectivity) and heterogeneous (separations) catalysts. However, the subtle changes of vibrational dynamics of molecular catalysts after surface attachment can significantly alter the catalyst's performance. For instance, coupling and interstate coherence between vibrational modes can be altered, which influence the channels for energy quickly sampling all of the vibrational modes and breaking chemical bonds.[203,204] Therefore, it is necessary to understand how the vibrational coupling and coherence dynamics of these catalysts are influenced by surface attachment.

The Re-bpy based complexes have been studied in solution phase using 2D IR spectroscopy,[119,205,206] and the corresponding monolayers have been investigated using time-resolved SFG spectroscopy[207] for vibrational relaxations and 2D IR spectroscopy,[208] for spectral diffusion. However, the dynamics between coupled vibrational modes, such as interstate coherence, have yet been observed because of the challenges mentioned above.

6.2 HD 2D SFG Spectra at Different Time

In this section, we first characterized the vibrational coherence dynamic of this molecular monolayer by acquiring the HD 2D SFG spectra with different waiting time t_2. We then took 2D IR spectra of **1** in solution and extracted the differences in the dynamics of **1** in solution and on the surface. To better quantify the different contribution to coherence dynamics, Fourier transform is applied to the series of HD 2D SFG (and 2D IR) spectra along the t_2 axis to obtain the corresponding 3D spectra.

Although this type of 3D spectroscopy has been taken in both bulk sensitive IR and visible spectroscopy,[209,210] to the best of our knowledge, this is the first time it is developed for surface specific SFG spectroscopy. In principle, the 3D spectra presented here carry the same dynamic information as the series of 2D spectra, but the advantage is that 3D spectra can better separate the homogenous and inhomogeneous broadening contributions to the interstate vibrational coherence peaks. We note that our 3D SFG spectra is different from the 5th order 3D spectra that Zanni, Hamm and Nelson pioneered.[210–214]However, in both types of 3D spectra, there are three coherences involved during the measurement and therefore both 3D spectra are essentially frequency correlation maps of three coherence states. The difference is one of the coherences characterized in our work is an interstate coherence – coherent superposition between two different vibrational modes, where in the 5th order 3D IR experiments all three vibrational coherences are coherent superpositions between different quanta of the same vibrational modes.

In the HD 2D SFG spectra series of **1** on gold (Fig. 6-1), there are both diagonal peaks and cross peaks. The diagonal peaks at $\omega_1 = 2020\ \mathrm{cm}^{-1}$ correspond to the fundamental transitions of A′ (1) of the CO modes (Appendix C.3), and the out of phase peak that is redshifted from the diagonal peak is the corresponding overtone transition. The peak sets between 1950 and 1890 cm^{-1}, correspond to the A″ and A′(2) modes of the CO groups,[205,208] which are also composed of the fundamental and overtone doublet. Due to strong coupling between vibrational modes, there are cross peaks (pairs of out of phase doublets) in both spectra at the corners of the 2D spectra, which are determined by the frequency of two coupled vibrational peaks. The 2D IR spectra (Fig. 6-2) show similar features, with A′(1) mode at 2020 cm^{-1}, and A″ mode at 1919 cm^{-1}, whereas the A′(2) mode is redshifted enough that it is out of the spectral coverage of our IR beam.

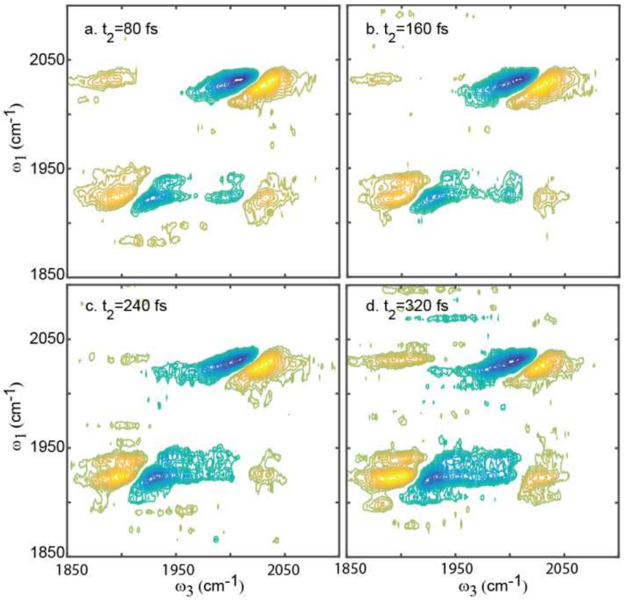

Figure 6-1. T$_2$ dependent HD 2D SFG spectra. As t_2 is increased from 80 to 320 fs (a-d) the cross peak intensity oscillates back and forth. All spectra are normalized to the absolute peak intensity of A′(1) mode.

The interstate vibrational coherence (quantum beating) of the surface catalysts can be visualized in cross peak intensity of HD 2D SFG spectra in Fig. 6-1 as t_2 is scanned. If interstate coherences are involved in the 2D spectra, the intensity of both cross peaks should oscillate as t_2 increases. We note that there should also be Feynman pathways involving the interstate coherence that contribute to the diagonal peaks,[195] but since the diagonal peaks are dominated by contributions that only involve population states during t_2, we focus on analyzing the cross peak intensity. In Fig. 6-1a-d, the HD 2D SFG spectra at 80, 160, 240 and 320 fs are plotted. The cross peak intensity first decreases and then recovers, which indicates there are interstate coherences that last long enough to be characterized. A similar trend from the 2D IR spectra of solution phase sample is also observed (Fig. 6-2). Therefore, the presence of cross peak oscillation during t_2 in both HD 2D SFG and 2D IR indicates that the interstate coherences exist in both solution and surface samples, and is not significantly disturbed by surface attachment.

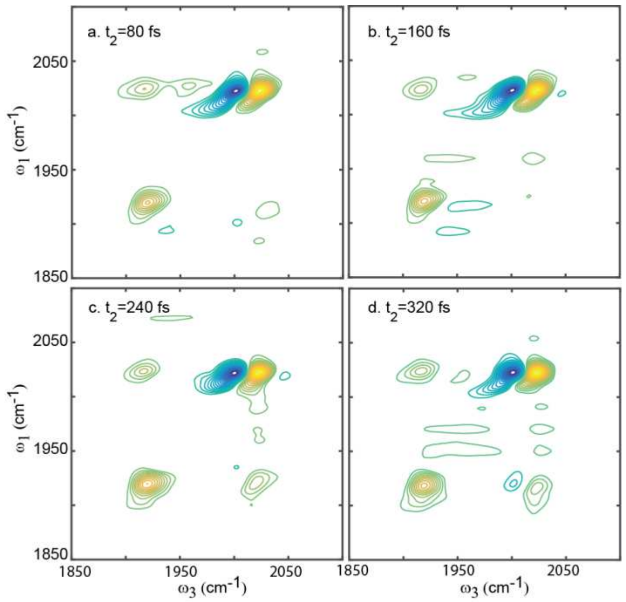

Figure 6-2. T_2 dependent 2D IR spectra. As t_2 is increased from 80 to 320 fs (a-d) the cross peak intensity oscillates back and forth. All spectra are normalized to the absolute peak intensity of A′(1) mode.

6.3 Dephasing Dynamics of the Interstate Coherence

Next, it is important to quantitatively determine the dephasing dynamics of the interstate coherence in both the surface and solution phase sample. We plot the integrated cross peak amplitude versus t_2. For both the surface and the solution phase spectra cross peak intensity oscillations are observed at early time delays. We Fourier transform the oscillatory cross peak intensity to obtain the corresponding spectra (Fig. 6-3b). In the frequency domain, peaks at 103 and 96 cm^{-1} appear for the solution and surface samples, respectively, which agree well with the energy difference between A′(1) and A″/A′(2) modes.

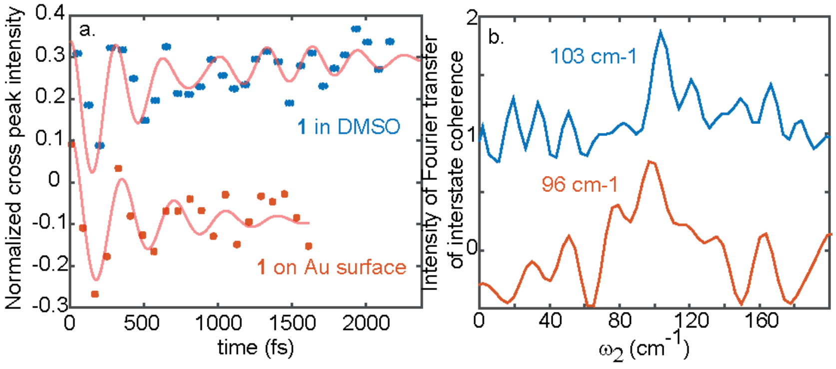

Figure 6-3. Interstate vibrational coherence dynamics. (a) Time-dependent integrated cross peak intensity with trend lines in pink (b) Corresponding Fourier transform power spectra.

Interestingly, the spectral linewidth of the surface sample is broader than the corresponding linewidth in the solution phase spectrum. The broader spectral width indicates a faster dephasing time of the interstate coherence for the surface sample. The fast dephasing process can come from (1) homogeneous broadening, an ensemble average of molecules that all have the same short dephasing time; or (2) inhomogeneous broadening, an ensemble average of molecules that all have long dephasing time but slightly different coherence frequencies. For the surface catalysts it is intuitive to think that the inhomogeneous surface distribution will lead to the fast dephasing time, but the question is: is there a homogenous contribution to the dephasing process? Distinguishing between these two mechanisms is critical since only the homogenous dephasing can dampen the vibrational coherence of individual molecules, which is related to catalytic performance. However, it is difficult to answer this question from only the lineshape of these spectra.

The homogeneous contribution to the dephasing process can be more accurately determined by applying the Fourier transform to the series of t_2 dependent HD 2D SFG and 2D IR spectra and obtain 3D spectra.[209,215] In 3D spectra, the interstate coherence peaks are well separated from those do not involve interstate coherences. For spectral peaks that involve interstate vibrational coherences, their 3D spectra appear around ω_2=100 cm^{-1} (Fig. 6-4a and b) whereas other spectroscopic signals that are not involved with the interstate coherence located at ω_2=0 cm^{-1}. This separation allows the spectral parameters of these interstate coherent peaks to be extracted without any interference from other peaks. In addition, the 3D spectra in our work track the dephasing dynamics of the single mode coherences during t_1, t_3, and the interstate coherence during t_2. Both solution phase and surface 3D spectra contain diagonal and cross peaks, indicating that the interstate coherences are involved in both spectral pathways, similar to 2D IR and 2D Vis spectroscopies[216]. We note there are additional peaks missing due to the spectral coverage and signal to noise limitations in our measurement. Nevertheless, we can clearly understand the interstate coherence dephasing dynamics from the available spectral features in the 3D spectra (Fig. 6-4a and b, blue boxes).

6.4 Lineshape Analysis of 3D spectra

To better examine the lineshape, we cut along ω_1 to get 2D spectra that reveal the correlation functions between the second and third coherences. The solution phase spectrum shown here involves a “nonrephasing” process (where the oscillation frequency of ω_{Aa} and ω_{A0} have the same sign) during t_2 and t_3, as indicated from the corresponding Feynman diagram (Fig. 6-4c). The spectral doublet (Fig. 6-4d) has a homogenous diamond lineshape,[217] which is the signature lineshape for homogeneous broadening - only homogenous solvent interactions contribute to the interstate coherence dephasing. In contrast, the spectrum from the monolayer sample in Fig. 6-4f is a rephasing spectra, since the oscillation frequency at t_2 and t_3 (ω_{aA} and ω_{a0}) have opposite signs (Fig. 6-4e). The spectrum in Fig. 6-4f is elongated along the diagonal. This is due to a heterogeneous molecular distribution, same as the contribution for inhomogeneous broadening in the HD 2D SFG spectra. However, the spectrum is also significantly broadened along the antidiagonal, with a linewidth ~24±2 cm^{-1}. In rephasing spectra, the antidiagonal linewidth corresponds to the homogenous linewidth. Since the upconversion pulse's spectral full width half maximum (fwhm) is < 20 cm^{-1}, narrower than the spectral linewidth, the antidiagonal linewidth indicates that the spectrum is homogenously broadened as well. Therefore, both homogenous and inhomogeneous dynamics contributes to the fast dephasing time of interstate coherence of the surface catalysts.

Since there are no solvent present around the catalysts on the surface, processes that contribute to the homogenous broadening must be interactions induced after surface attachment, such as coupling to the image dipole on the surface,[218] coupling to other low frequency surface modes,[219,220] non-adiabatic electron transfer coupling,[221] or intermolecular interactions, such as dipole-dipole coupling[222]. Non-adiabatic electron transfer coupling between the adsorbates and substrates happens when the adsorbates' electronic states are heavily mixed with the d-band of metal states[221]. Since CO modes do not directly attach to the surface, it is unlikely that orbital mixings between the CO and gold surfaces exist. Similarly, coupling to low frequency surface modes may not cause dephasing of vibrational coherences.[219,220] Low frequency modes such as hindered translation or rotation can only strongly affect CO vibrational dephasing dynamics, if the CO modes are not directly attached to the surface, which is not the case in the current system. Another possibility would be intermolecular interactions such as dipole-dipole coupling between adjacent molecules[223], but it is understood that dipole-dipole interaction are not effective in this type of molecular monolayers[222].

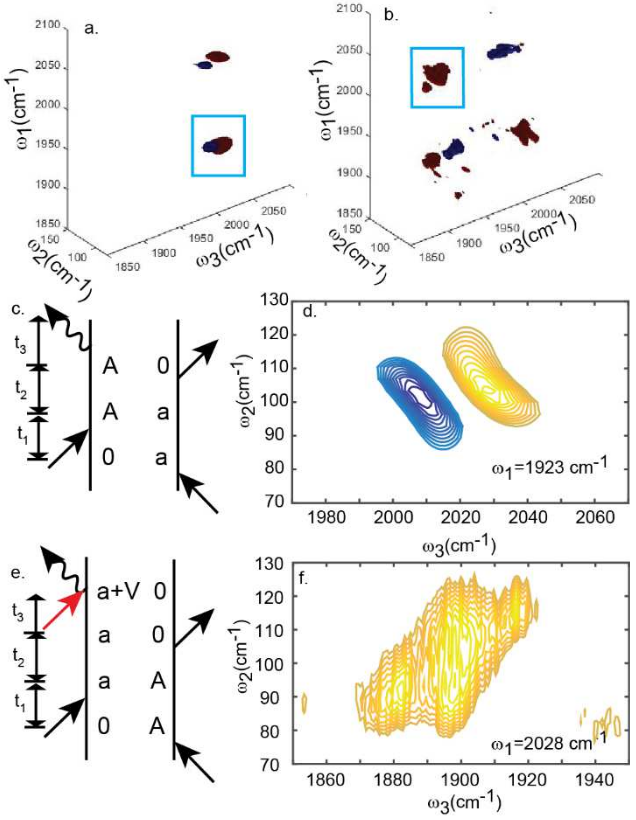

Figure 6-4. 3D vibrational spectra. (a) 3D IR spectra obtained by Fourier transform of the t_2 axis. (b) 3D SFG spectrum (c) Feynman diagram of the spectral slide (d) of 3D IR spectrum. State "A" represents the vibrational state with higher energy, whereas state "a" is the one with lower energy (e) Feynman diagram of the spectral slide (f) of 3D SFG spectrum.

The scenario that the adsorbate electrostatically couples to the image dipole on the surface is likely to account for our observations, as it is often the dominating force for homogenous dephasing[218]. This agrees with previous work where we observed that single vibrational mode dynamics are influenced by image dipole interactions for the same system.[5] The image dipoles should couple to all the vibrational modes, which induces homogenous dephasings not only to the single vibrational modes but also the interstate coherences between different vibrational modes. This new experimental result indicates that even though the vibrational modes of interests are not in direct contact with the substrates (i.e. carbonyls), there are still adsorbate-substrate interactions that can influence the vibrational dynamics.

6.5 Summary of the Chapter

In summary, we characterized the interstate vibrational coherence dynamics of a surface monolayer using fourth-order 3D SFG spectroscopy. By comparing it to the 3D IR spectra of compound **1** in solution phase, we learned that surface attachment induces both homogenous and inhomogeneous dephasing dynamic of the vibrational modes, but the coherence is preserved upon surface grafting. The method demonstrated here can be easily extended to monolayers under working conditions, and can provide a new platform for *in operando* investigation of previously unavailable physical properties. In combination with the current state of the art computational research, the rich and detailed knowledge learned from HD 2D SFG and 3D SFG spectroscopies can extract the critical physics for catalysts and therefore provide comprehensive understanding of surface monolayers.

Chapter 6, in part, is a reprint of the material as it appears in Yingmin Li, Jiaxi Wang, Melissa L. Clark, Clifford P. Kubiak, Wei Xiong. "*Characterizing Interstate Vibrational Coherent Dynamics of Surface Adsorbed Catalysts by Fourth-order 3D SFG*

Spectroscopy". Chemical Physics Letters, 650, 1-6. The dissertation author is the first author of this work.

Chapter 7 Salting Up of Proteins at the Air/Water Interface

From chapter 3 to chapter 6, interface sensitive nonlinear spectroscopic methods are applied to study the air/solid interfaces and hidden interfaces. In this chapter, a vibrational sum frequency generation study, in combination with surface pressure measurement, on air/water interface is demonstrated to understand the adsorption kinetics of a globular protein, bovine serum albumin (BSA). It is learned that at low (2-5 ppm) protein concentrations, which is relevant to environmental conditions, both VSFG and surface pressure measurements of BSA behave drastically different than at higher concentrations. This phenomenon is term as “salting up” which differs from the well-known “salting out” effect as it occurs at protein concentrations well-below where “salting out” occurs.

7.1 Introduction

Proteins, which are ubiquitous in biological systems, are also enriched at the sea surface microlayer, the topmost layer of the ocean surface, and present within sea spray aerosol, despite their ultralow concentrations in the ocean.[224–227] Adsorbed proteins at the air/sea water interface play important roles. For example, enzymes at the interface have been suggested to alter the surface properties of sea spray aerosol,[228,229] and surface proteins can also stabilize foams and bubbles.[230–232]

To provide physical insights into protein adsorption at the air/salt water interface, we combine VSFG with surface pressure measurements to study BSA at low bulk concentrations (2-5 ppm) at the air/ salt water interface. We demonstrate a “salting up” phenomenon whereby certain proteins partition to the interface within tens of minutes to a few hours, in the presence of salts, but not in their absence. These results show for the first time that ions play an important role in the dynamical adsorption of proteins at the air/salt water interface.

Protein concentration in bulk sea water is found to be much lower than the corresponding concentration at the sea surface microlayer.[233–236] What drives proteins to the air/liquid interface? To answer this question, air/liquid interface sensitive techniques are needed. VSFG, as a second order nonlinear optical technique, has inherent interface selectivity, and has become a useful spectroscopic tool to detect proteins at air/liquid interface *in-situ*[8,230,237–240]. Most of the previous VSFG experiments have focused on high protein concentrations (ca. 1000 ppm),[230,239] and not at low environmentally relevant concentration (~2 ppm). Additionally, although the effects of salts on protein behavior in bulk solutions have been extensively studied,[241–245] the influence of relatively high concentrations of salts on proteins at the air/water interface has hitherto not been demonstrated. Most of the previous studies used buffer solutions, which are at relatively low ionic strength.[238,239,246]

7.2 Experimental Details

The VSFG spectrometer used in this experiment has been described in previous publications.[6,175,247] All spectra are collected using SSP polarization (polarization of signal, visible input, and infrared input beams, respectively). Salt solutions with concentrations of ~35 g/L are prepared by dissolving sea salt (Sigma Aldrich, composition listed in Table D-1) in D_2O and H_2O for VSFG and surface pressure measurements, respectively. This sea salt solution represents the high salinity and high ionic strength of sea water and is therefore a good mimic for studying the air/sea water interface. We use D_2O in VSFG experiments to remove the interference from the H_2O bending mode, near the absorption frequency of the amide I band. BSA (≥ 98%, Sigma Aldrich) is added to the sea salt solution to make a 1 mg/mL (1000 ppm) concentrated solution, which is then diluted to required concentrations (5, 4, 3 and 2 ppm). For experiments without salts, BSA is directly added to D_2O/H_2O to obtain a 1 mg/mL solution and then desired concentrations of protein solutions were prepared. The protein solutions are freshly prepared before each of these reported experiments. The solutions are loaded into a petri dish that is covered with parafilm to alleviate water evaporation. A slit is cut on the parafilm to let the light pass through. The preparation of lysozyme and lipase solutions follow the same protocols as BSA solutions.

7.3 VSFG Study on BSA at Air/Water Interface

VSFG spectra of BSA show very different behavior at the air/salt water interface compared to the air/pure water interface (Figure 7-1a). As seen in Figure 7-1a, there is a VSFG feature from BSA at the air/salt water interface, whereas the spectrum for the air/ pure water interface is featureless. The small bump in the red trace is due to the nonresonant signal of D_2O (Fig. D-1). The main peak centered at 1650 cm^{-1} in Figure 7-1a is attributed to the amide I band of α-helices.[240,248,249] Overall, these spectra indicate that salts influence the appearance of the VSFG signal from BSA at the interface. We note the VSFG signal probes interfacial BSA only, and not the bulk BSA due to the electric field induced $\chi^{(3)}$ term,[179–186,250–253] because of the large ionic strength (I=0.71 mol/L) used in this study.

The effect of salts on the VSFG signal from BSA is dynamic. While the spectra show a strong amide I band response at 40 minutes after BSA salt solution is loaded (Figure 7-1a), at earlier times (after 10 minutes) there is no VSFG signal (inset, Figure 7-1a). This result suggests the absence of ordered BSA molecules at the interface following the introduction of BSA solution.

To further elucidate the kinetics of the VSFG signal obtained from BSA, we performed time-dependent VSFG measurements on both air/ pure water and air/salt water interfaces. Figure 7-1b shows the integrated VSFG intensity of the amide I band as a function of time. From this VSFG kinetic study, we observe that only air/salt water interface shows the emergence of a strong signal and the evolution of protein adsorption. The kinetics of this adsorption process show the following: At first there is an induction period (1 and 2 in Figure 7-1c), followed by a rise in signal (3 in Figure 7-1c) and then by saturation of the signal (4 in Figure 7-1c). This behavior is not observed when BSA is in pure water, nor in systems of salt water without BSA (Fig. D-2).

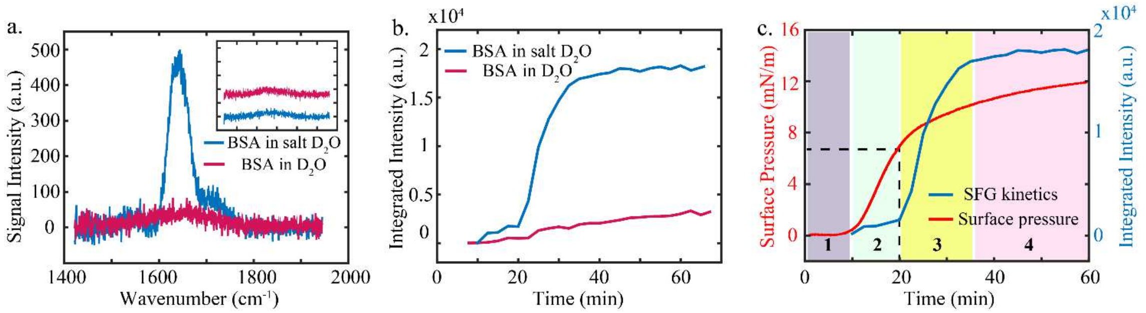

Figure 7-9. VSFG spectra of BSA monolayer at air/liquid interface. (a) Static VSFG spectra of 3 ppm BSA in salt water and in pure water collected 40 minutes after the solutions are loaded. The inset shows the spectra collected 10 minutes after the solutions are loaded and the purple spectrum is offset for clarity. (b) Kinetic studies of VSFG signal. VSFG response of BSA at the air/salt water interface undergoes a steep increase at around 20 minutes, whereas no such change is seen at the air/water interface. (c) Adsorption kinetics at the air/salt water interface. Under the same sample condition, surface pressure and SFG show different adsorption kinetic. The dashed lines mark the surface pressure value when the VSFG signal begins to increase. The *colored* areas represent different stages of adsorption (1 to 4) described in the main text.

There are two possible explanations for these observations. In the first scenario, at low concentrations, few BSA molecules adsorb at the surface because of slow diffusion of BSA from the bulk solution. The diffusion is accelerated by ions, which drive BSA to the interface. Once at the interface, the adsorbed interfacial proteins rearrange into ordered structures and generate VSFG signals. A second scenario is that BSA molecules are adsorbed at the interface from the start, but the proteins need time to rearrange into ordered structures, which leads to the VSFG signal, and that ions play an important role in the protein rearrangement at the interface.

7.4 Surface Pressure Study on BSA at Air/Water Interface

To test these two scenarios, we performed surface pressure measurements. Unlike VSFG, surface pressure measurements are sensitive to the presence of surface species, but rely little on the orientation, conformation or ordering.[254] Thus, we can disentangle the dynamics of surface adsorption from changes in structural/conformational and/or ordering. The surface pressure measurement exhibits a qualitatively similar, but quantitatively different time dependence when compared to VSFG kinetics (red line, Figure 7-1c): The surface pressure measurement only has a 10-minute induction period, while for VSFG it takes 20 minutes before the signal rapidly rises at the same experimental condition. Following the induction period, surface pressure increases sharply, till it reaches a bending point, where there is a much slower rate of increase in the surface pressure. However, only around when surface pressure reaches a bending point, VSFG signal start to rise.

Because the surface pressure change reflects the amount of BSA molecules adsorbed at the surface, it means that at 10 minutes after BSA solution is added, the surface coverage of proteins drastically increases at air/salt water interface. However, because the VSFG signal only starts to increase at 20 minutes, when many BSA molecules are present at the interface, this additional lag phase in VSFG kinetics indicates that rearrangement and ordering of BSA occurs during this period. Therefore, these results support the hypothesis in the first scenario, i.e. there is adsorption of BSA molecules at the interface followed by rearrangement at the interface. In contrast to salt water conditions, proteins in pure water show no surface pressure change within 60 minutes (Fig. D-4), which is consistent with the VSFG results.

7.5 Surface Coverage Induced Structural Rearrangement

There is another interesting kinetic effect observed. The 20-minute induction period in the VSFG data roughly matches the bend in the surface pressure curve (Figure 7-1c). At the bending point of the surface pressure, the surface concentration is around 0.82 mg/m^2, corresponding to a surface coverage of 90%. (Fig. D-6)[255] At such a high surface coverage, protein molecules are more likely to interact with one another leading to ordered structures. Therefore, we speculate that the surface coverage of BSA needs to reach a critical value (and concomitant with that a critical surface pressure) to undergo any structural rearrangement and/or ordering at the interface.

To determine the role of surface coverage in the structural rearrangement of BSA at the interface, we measured the VSFG and surface pressure kinetics for three other concentrations: 2, 4, and 5 ppm (Fig. 7-2). If there is a critical surface coverage, the time for the VSFG signal to appear should correlate with the same surface coverage (pressure), regardless of the bulk protein concentration. In Figure 7-2, these four concentrations have different induction times and different duration of all periods for both surface pressure and VSFG signal kinetics. However, VSFG signal begins to increase approximately at the bending points of the surface pressure curves for all concentrations, which corresponds to a critical surface pressure of between 5.8 to 6.8 mN/m. At this surface pressure, the corresponding surface concentration is 0.82 ± 0.02 mg/m^2, and surface coverage is

90%±2%. (Fig. D-6) Thus, from these results we can conclude that 90% is the critical surface coverage, which triggers protein interactions for structural rearrangement and/or ordering.

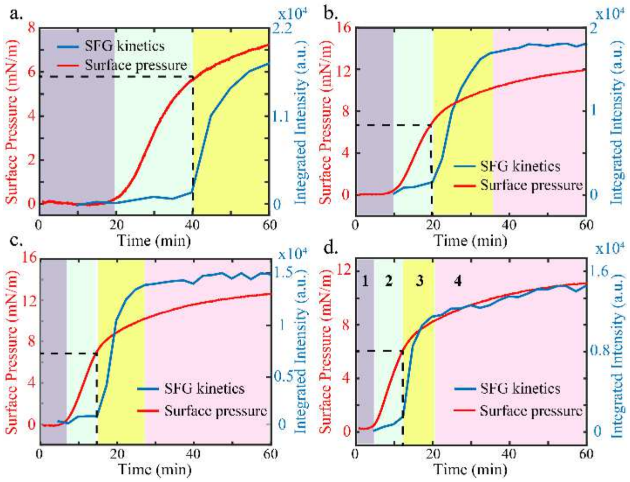

Figure 7-2. Adsorption kinetics of BSA at the air/salt water interface at different protein concentrations. (a) 2 ppm; (b) 3 ppm; (c) 4 ppm; (d) 5 ppm. A concentration dependent induction time is observed in all cases. However, the corners formed by the pair of dashed lines show that a certain surface pressure needs to be reached before the VSFG signal appears.

A four-stage model of the adsorption kinetics is proposed based on these experimental observations (Figure 7-3). In salt water, a majority of BSA molecules initially stay in the subphase and gradually migrate to the surface, which can be attributed to a salting up effect driven by ions. As the surface coverage reaches ca. 50% (Stage 1), it causes the surface pressure to increase[256]. In Stage 2, BSA molecules continue to accumulate at the surface until the surface pressure reaches a value of ca. 6 mN/m, (c.a., 90% surface coverage), which triggers a structural rearrangement and/or ordering that leads to the VSFG signal. In Stage 3, the drastic increase in the VSFG signal reflects BSA reorientation and ordering process at the interface. Both surface pressure and VSFG signal reach an equilibrium (or slowly changing) state in Stage 4.

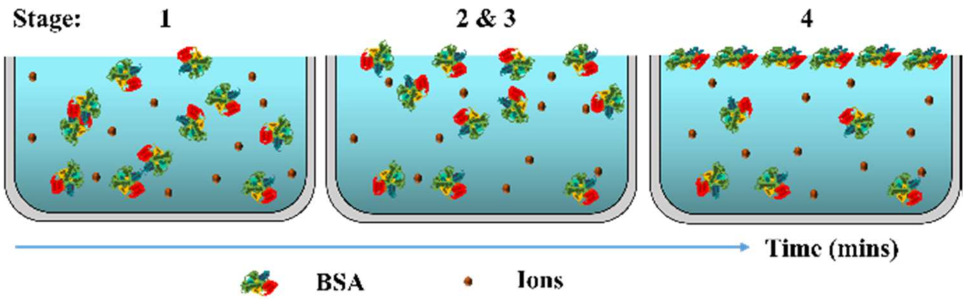

Figure 7-3. A schematic of the different stages of adsorption kinetics for BSA at the air/salt water interface.

This four-stage model can be applied to all concentrations investigated here. The induction time is closely related to the BSA concentration - the higher the concentration, the shorter the induction time (the induction times for 2, 3, 4 and 5 ppm are 40, 20, 15, and 12 minutes, respectively). This concentration dependence can be explained by diffusion process that drives the protein to the interface.[8] At higher concentrations, more BSA molecules diffuse to the interface taking less time to reach a critical surface coverage.

7.6 Mechanism of "Salting Up" Effect

In order to get more insights about the mechanism of "salting up" effect of BSA, we performed a salt concentration dependent experiment. The surface pressure kinetics of 5 ppm BSA in three different NaCl concentration solutions, which are 0.5 M, 0.05 M and 0.005 M, are measured, while pure water and BSA water solution are used as control. As shown in Figure 7-4, Because the onset of salting-up happens at 0.005 M NaCl (0.005 M ionic strength), it suggests that the electrostatic screening is a key driving force for salting-up. For example, the salt ions in solution successfully build a screen layer with Debye length similar or shorter than the diameter of BSA, thereby screening charges on BSA and reducing the interaction between protein and water to allow BSA molecules partitioning to the surface. However, BSA solution with higher NaCl concentration shows larger surface pressure value at equilibrium which indicates larger BSA surface coverage. We believe that the dependence on salt concentration is originated from the volume exclusion in "salting out". For "salting out", hydrated ions strongly interact with their first hydration shell which produce large energy barrier to interact with proteins. As a consequence, hydrated ions are excluded from protein molecules in the bulk solution and when more hydrated ions are added, it leads to protein aggregations ("salting out') and thus reduction of excluded volume at the protein surfaces. Thus, for salting up, when adding more hydrated ions to the solution, aside from electrostatic screening effects, it can also induce more excluded volume at protein surfaces and driving protein to emerge onto surface and aggregate.

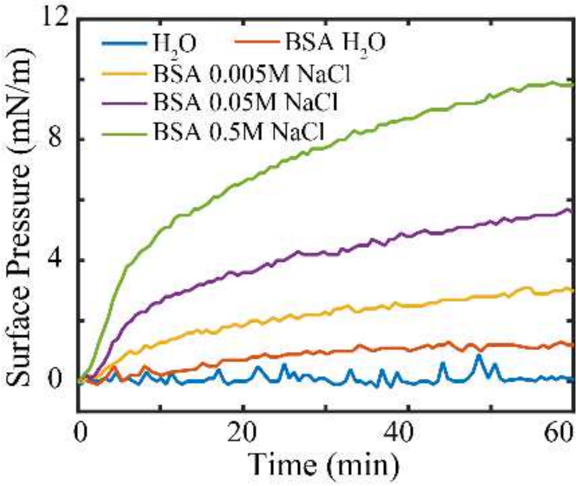

Figure 7-4. Surface pressure kinetics of 5 ppm BSA in different NaCl concentration solution.

To test if "salting up" effect is a general phenomenon to all proteins, we performed the surface pressure measurement on lysozyme and lipase with the same molarity as BSA. The concentration of NaCl is set to be 0.5 M. Interestingly, we find the surface pressure for both lysozyme and lipase solutions doesn't change after 60 min (Fig. D-7) which means the protein molecules stay in the aqueous phase. There are two general difference between

BSA and the other two proteins: first, it is known that lysozyme and lipase both have rigid structure, while BSA is known as a "soft" protein and has low internal stability; second, in NaCl solution (pH=7), BSA is negatively charged while lysozyme and lipase are positively charged. Both differences could cause the observed distinction. To learn whether it is charge type on protein surface affecting adsorption dynamics, we performed a control experiment of 5 ppm BSA in 0.5 M NaCl solution with pH=3, which is below the isoelectric point of BSA, and therefore BSA is positively charged. The result shows the surface pressure of BSA also increased indicating "salting up" still exists (Fig. D-8). Thus, despite that electrostatic screening is critical in "salting up", the type of charges does not play an important role. On the other hand, it is likely that structural flexibility of proteins influence "salting up". The mechanism of how salt ions change protein structures to drive them to the surface subjects to future MD simulation study.

7.7 Summary of the Chapter

In summary, we observe the accelerated emergence of BSA at air/liquid interface due to the presence of salts, which can be due to a new "salting up" effect. It is well known that salts impact protein behavior in bulk solution, with "salting in" and "salting out" effects.[257–259] Our observations lead to a conclusion that while both "salting up" and "salting out" depends on volume exclusion induced by hydrated ions, there are additional mechanistic difference between them, e.g., "salting up' also depends on flexibility of protein structures. The mechanistic difference is supported by that the phenomenon of "salting up" is not related to the formation of aggregates in the bulk as observed for "salting out". Experiments performed using dynamic light scattering (DLS) showed no protein aggregation even under much higher protein (1000 ppm) and salt concentrations (Fig. D-

5), which suggests that "salting up" occurs at a different condition than the one that drives "salting out". One way to understand this substantial difference is that lower protein concentrations may be needed to reach to a critical point for rearrangements in 2D surface compared to the 3D bulk environment.

This study demonstrates for the first time that salts play a pivotal role in BSA adsorption dynamics at air/aqueous interface, which we term as the "salting up" effect. The mechanism of "salting up" lies in the electrostatic screening, structural change of BSA and volume exclusion induced by the hydrated salt ions. Initial mechanistic studies indicate that "salting up" is specific to certain types of proteins that have "soft" structure. Because this study focuses on environmental chemistry related condition, extensive survey of various salt is out of the scope of this initial report. However, this exciting initial result would lead to further study to categorize the proteins that can salt up, as well as more mechanistic studies in whether salting up is ion specific (initial study on NaCl and $CaCl_2$ suggests that salting up is less sensitive to the types of ions, i.e mono- versus di-cations). Further investigation of the salting up effect, using different experimental (e.g. x-ray scattering[260] and VSFG microscopy[190,261,262]) and computational methods,[263] is warranted.

Chapter 7, in part, is being prepared for publication of the materials. Yingmin Li, Mona Shrestha, Man Luo, Meishi Song, Vicki Grassian, Wei Xiong will be the coauthors. The dissertation author is the first author of this work.

Chapter 8 Conclusions and Perspectives

Ultrafast nonlinear spectroscopy is a powerful technology to probe surfaces and interfaces, from both static and kinetic perspective. New methods of performing nonlinear spectroscopy study and improvements of existed techniques are discussed in this dissertation, which are applied to various interfaces to provide new knowledge of interfaces. The main findings can be summarized as following:

1. The bandgap at buried interface can be measured by electronic sum frequency generation spectroscopy is demonstrated for the first time. It is found that the bandgap at interface is different from bulk materials. P3HT/Si system is studied as an example where the bandgap of P3HT at interface is determined to be 2.2 eV whereas the UV-vis measurement gives 2.3 eV bandgap for the thin film. Since the measurement can be performed under ambient condition, it provides a handy tool to study electronic structure of interface under working environment.

2. Ultrafast charge dynamics at interface is explored by transient VSFG spectroscopy. The first transient electric field induced VSFG measurement is demonstrated on P3HT/Au samples and we observed the direct interfacial charge transfer across the interface. With the help of DFT calculations, the molecular conformation at interfaces is related to the charge behaviors. It is concluded that a subensemble of P3HT molecules at interface possess parallel or close to parallel conformation relative to the gold substrate that enables the strong electronic coupling between the π orbitals of P3HT and the electronic state of gold. This coupling then facilitates the direct electron transfer from gold to P3HT

3. A phase sensitive detection method – heterodyne detection is applied to P3HT/Au interface to learn the molecular response during the charge transfer process. A phase rotation method is established to separate the molecular signal from the nonresonant electronic signal. The heterodyne detected transient VSFG signal allows us to resolve three different dynamic components during the charge dynamics which are coherent artifact, unsuccessful charge transfer and direct interfacial charge transfer. The phase resolved dynamics would help us better understand the physical picture of charge transfer dynamics.

4. A monolayer of Re(diCN-bpy)(CO)3Cl catalyst attached to gold surface is investigate through multidimensional SFG spectroscopy. The interstate vibrational coherent dynamics is studied through the first fourth-order 3D SFG spectroscopy. Both homogeneous broadening and inhomogeneous broadening are determined by the lineshape. By comparing to the molecules in solution phase, the effect of surface attachment is analyzed.

5. Protein adsorption kinetics is measured by VSFG spectroscopy where BSA is studied as a model sample. BSA molecules are found to come to the air/water interface within a much shorter waiting time with the assistance with salt ions than without them. This observation is described as “salting up” effect which is different physical process than the know “slating out” phenomenon. By doing the salt concentration dependent experiment, the mechanism of “salting up” effect is explained by electrostatic force. After testing lipase and lysozyme, two types of proteins with hard structure, it is concluded that the emergence of “salting up” effect also depends on the structure of protein molecules.

Using ultrafast nonlinear spectroscopy, we have shown that it can produce new knowledge and insights for surfaces and interfaces. A lot of continuous research can be carried out based on the work presented in this dissertation. For example, the ultrafast charge dynamics across different interfaces can be studied which is an ongoing project in our group. By using different metal substrates including gold, silver and platinum, the relationship between the phase and the charge transfer direction can be unambiguously determined. Other than that, charge dynamics at different interfacial band structures can be explored with the help of theoretical calculations such as DFT.

Another exciting future direction is to investigate the mechanism of “salting up” effect in more details, especially to explore the role played by protein structures and the interactions between salt ions and proteins. Computational methods such as molecular dynamics simulation can be very helpful to provide the structural information. Other studies of protein molecules using structure sensitive nonlinear spectroscopy techniques in combined with the linear absorption spectroscopy methods such as FTIR and infrared reflection absorption spectroscopy (IRRAS) would be very helpful to study the mechanism of protein degradation and unfolding process.

Appendices

Appendix A

A.1 Fresnel factor calculation

In order to determine the fractions of the ESFG signal coming from the P3HT/Si interface or the P3HT/Air interface. We calculate the Fresnel factor for each interface to find out how much SFG signal is generated. As mentioned in the main paper, the intensity of the ESFG response is proportional to the square of the effective second order susceptibility, $x_{eff}^{(2)}$. For SSP polarization combination, which we used in our experiment, $x_{eff}^{(2)}$ can be expressed as:

$$x_{eff,SSP}^{(2)} = L_{yy}(\omega_{SFG})L_{yy}(\omega_{vis})L_{zz}(\omega_{NIR})\sin\beta_{NIR}\, x_{YYZ} \qquad \text{(A1)}$$

where ω_{SFG}, ω_{vis} and ω_{NIR} are the frequencies of ESFG signal, visible and NIR fields, respectively. β_{NIR} is the incidence angle with respect to the surface normal for the optical field of ω_{NIR}. $L_i(\omega_i)$ is the tensorial Fresnel factor at ω_i defined as following:

$$L_{yy}(\omega_i) = \frac{2n_1(\omega_i)\cos\beta_i}{n_1(\omega_i)\cos\beta_i + n_2(\omega_i)\cos\gamma_i}$$

$$L_{zz}(\omega_i) = \frac{2n_2(\omega_i)\cos\beta_i}{n_1(\omega_i)\cos\gamma_i + n_2(\omega_i)\cos\beta_i}\left(\frac{n_1(\omega_i)}{n'(\omega_i)}\right)^2 \qquad \text{(A2)}$$

where $n_m(\omega_i)$ is the refractive index of medium m (m=1,2) at frequency ω_i, γ_i is the refractive angle of medium 2 which can be calculated via $n_1(\omega_i)\sin\beta_i = n_2(\omega_i)\sin\gamma_i$. $n'(\omega_i)$ is the refractive index of the interfacial layer at frequency ω_i. We estimate the value of $n'(\omega_i)$by taking the average of the refractive index of the two mediums aside of the interface since we cannot determine the accurate value of $n'(\omega_i)$. All the parameters used for the calculation are summarized in Table. A1

Table A1. Parameters of the calculation for Fresnel factor

	n(800nm)	n(SFG)	n(NIR)
P3HT	2.27	2.46	2.17
Si	3.75	4	3.4
Air	1	1	1

A.2 Fitting of UV-vis spectrum of P3HT

The UV-Vis spectrum is taken on a P3HT thin film spin coated on to a sapphire window, using the same condition as we prepare it on Si substrate. Fig. 3-4 shows the UV-vis spectrum of the regioregular P3HT sample. The spectrum is fitted into 4 Gaussians, where each Gaussian is in form of a*exp(-(x-b/c)^2). The fit reproduces the experimental data well, and the parameters are summarized in Table. A2. The first two peaks locate at 2.04 and 2.20 eV correspond to electronic states of P3HT polymers, where the two higher energy peaks are from oligomer or monomers. Nevertheless, we can clearly see that each of them has the band width bigger than 0.2 eV, which is much larger than the bandwidth of ESFG signal.

Table A2. Parameters of the fitted Gaussian

	Peak 1	Peak 2	Peak 3	Peak 4
a	0.091±0.011	0.14±0.03	0.18±0.02	0.137±0.004
b (eV)	2.041±0.002	2.202±0.007	2.45±0.03	3.02±0.04
c (eV)	0.084±0.05	0.18±0.02	0.33±0.03	0.65±0.04
FWHM (eV)	0.14±0.08	0.30±0.03	0.55±0.05	1.08±0.07

A.3 Fitting of the ESFG spectrum

As demonstrated in the main paper, the measured normalized ESFG intensity ratio between P3HT/Si and Au should be fitted by,

$$\left|x_{eff}{}^{(2)}\right|^2 = \left|x_{NR}^{(2)} + x_{ijk}^{(2)}(\omega_{SFG}) \cdot e^{i\cdot\varphi} + x_{Si}^{(2)}(\omega_{SFG})\right|^2 \tag{A3}$$

$x_{Si}^{(2)}(\omega_{SFG})$ can be determined by measuring the ESFG of the bare Si surface. The ESFG spectrum of Si can be fitted to a linear function in the form of $ax + b$ to simplify the fitting, since the corresponding UV-vis spectrum is nearly linear. The nonresonant signal of P3HT/Si is treated as a constant. We use a Lorentzian function (Shown in Eq. A4) and a Gaussian function (Shown in Eq. A5) to fit the resonant signal, respectively. Then, the functions we use to fit Eq. A3 are as following,

$$Re\left(a_0\left(\frac{1}{x-b_0-i*c_0}\right)e^{i*\varphi} + C_{NR} + ax + \mathrm{b}\right)^2 \tag{A4}$$

$$Re(a_1 * e^{\frac{-(x-b_1)^2}{c_1{}^2}} * e^{i*\varphi} + C_{NR} + ax + \mathrm{b})^2 \tag{A5}$$

where a_0 and a_1 determines the amplitude of the spectrum, b_0 and b_1 are the peak position and c_0 and c_1 correlate to the width of the spectrum. C_{NR} represents the nonresonant signal from P3HT and the term “$ax + b$” stands for Si signal. All the fitting parameters are included in Table. A3.

Table A3. Parameters of fitted linear and Lorentzian function

	a	b			
Si	-0.3±0.4	0.8±0.8			
	a_0	b_0 (eV)	c_0 (eV)	φ	C_{NR}
Lorentzian	0.007±0.004	2.199±0.004	0.014±0.006	-1.5±0.3	1.22±0.08
	a_1	b_1 (eV)	c_1 (eV)	φ	C_{NR}
Gaussian	0.50±0.12	2.202±0.004	0.022±0.009	0	1.21±0.08

We can then plot each individual terms in the main text to different contributions to $\left|x_{eff}{}^{(2)}\right|^2$.

A.4 Spectral normalization

As indicated in Eq. A6, the measured homodyne ESFG signal is quadratically dependent on the second order susceptibility$x^{(2)}$, the amplitude of near IR (E_{NIR}) and 800nm (E_{800nm}) electric fields, and the reflectivity (*r*) of both beams. By taking the ratio between the ESFG of P3HT/Si and gold, we can take out the dependence on electric field amplitude, which can change as the near IR frequency is scanned. Assuming the reflectivity ratios between P3HT/Si and gold remain constant, this ratio corresponds to $x^{(2)}$.

$$S_{ESFG} = |E_{ESFG}|^2 \propto |x^{(2)} E_{NIR} E_{800nm} r_{NIR} r_{800nm}|^2 \tag{A6}$$

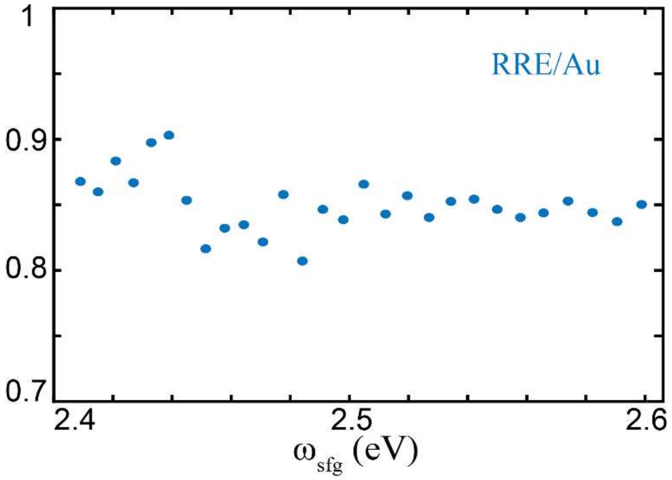

Figure A-1. Ratio between the ESFG signal of regioregular P3HT/Si interfaces and Au. The plot is nearly flat, which indicates non-resonant condition in this range.

Fig. A-1 shows the ESFG intensity ratio between P3HT/Si and Au between 2.4 to 2.6 eV. The ESFG intensity does not depend on the frequency of the ESFG signal, which indicates no resonant condition is satisfied.

Appendix B

B.1 UPS measurement

We performed ultraviolet photoelectron spectroscopy (UPS) measurement on bare gold and P3HT/Au samples to determine the band alignment at P3HT/Au interface. Using UPS, the relative positions between the highest occupied molecular orbital energy level (HOMO) of P3HT and the gold Fermi level (E_F) can be figured out. Fig. B-1a shows the photoemission spectrum of bare gold substrate and P3HT/Au interface at near gold Fermi level in linear scale. From Fig. B-1a, we determine the HOMO of P3HT 0.50 ± 0.05 eV lower than the gold Fermi level. Then, the position of the lowest unoccupied molecular orbital energy level (LUMO) can be inferred from the band gap of P3HT (2 eV). The vacuum level change is obtained from secondary-electron cutoff in the UPS data.[27] Based on Fig. B-1b, we measured the vacuum level of P3HT 0.60 ± 0.05 eV below the gold vacuum level. Thus, we determine the band alignment of the P3HT/Au interface, which is summarized in Fig. 4-1b.

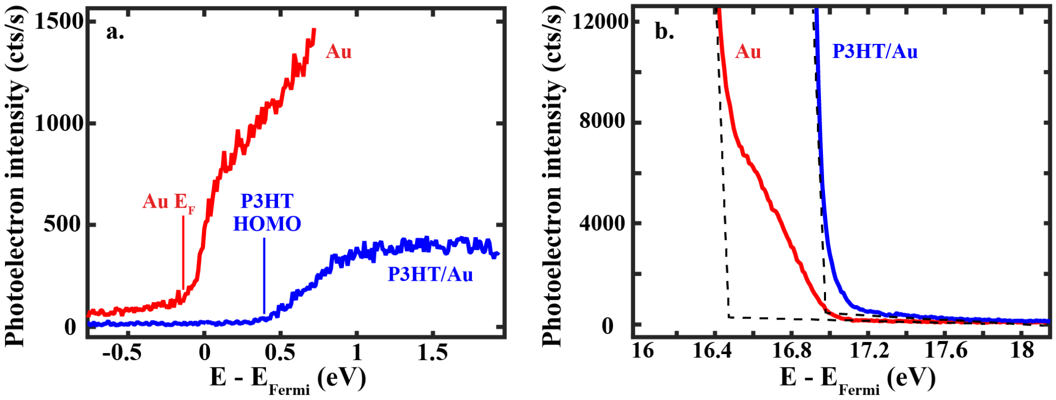

Figure B-10. Ultraviolet photoelectron spectroscopy on Bare gold and P3HT/Au interfaces. (a) UPS spectra in the gold Fermi level region (b) UPS spectra shows the secondary-electron cutoff. The P3HT VBM can be placed 0.5 eV below gold Fermi level. The secondary-electron cutoff difference can be determined to be 0.5 eV

B.2 Tr-VSFG data acquisition, analysis and calculations

B.2.1 Double interfaces simulation

There are two interfaces that could contribute to the VSFG signal of the P3HT/Au sample which are P3HT/Au (buried interface) and Air/P3HT interfaces (top interface). Since no charge transfer could happen across the air/P3HT interface, all the dynamic features observed in our experiment should be generated from the P3HT/Au interface. Nevertheless, it is necessary to learn the relative contribution of each interface to VSFG signals, which is important to understand the static and dynamic spectra. To do so, we run a simulation to decompose the SFG signal contribution from each interface. The procedure of this simulation follows the description of a publication by O'Brain and Massari[42], and the simulation code is based on a Matlab program provided by the Roberts group[152].

In the simulation, we input a series of experimentally measured VSFG spectra of P3HT/Au samples with different P3HT film thickness. The VSFG signal should be modulated by the film thickness, because of interferences between signals from the top and bottom interfaces. Thus, it is possible to determine the relative contribution of VSFG signals from each interface based on how VSFG signal is modulated as thickness is varied. The simulation results depend on many parameters, including film thickness, beam incidence angle, upconversion pulse FWHM, refractive indices and so on. A few important parameters and how they are obtained are provided here: Thicknesses of P3HT layer are characterized by profilometry. Incident angles of IR and upconversion beams are 62° and 63°, respectively. Our FWHM of upconversion beam is 9.5 cm^{-1}. The refractive indices of P3HT are approximately 2.2 within mid IR range[45] and 2.0 at 792 nm[264]. We refer to P.

Johnson and R. Christy's paper[265] to obtain the refractive indices of gold at different wavelength.

The fitting results and the relative contribution from top and bottom interfaces to the VSFG spectra are summarized in Fig. B-2. The fitted result (Fig. B-2b) qualitatively reproduced the trend of the experimental measurements (Fig. B-2a). The decomposed VSFG spectrum of each interface are shown in Fig. B-2c where most of the VSFG signal is generated from the P3HT/Au interface, whereas the top interface barely contributes. This suggests interference between the signal from each interface plays a minimal role in our study.

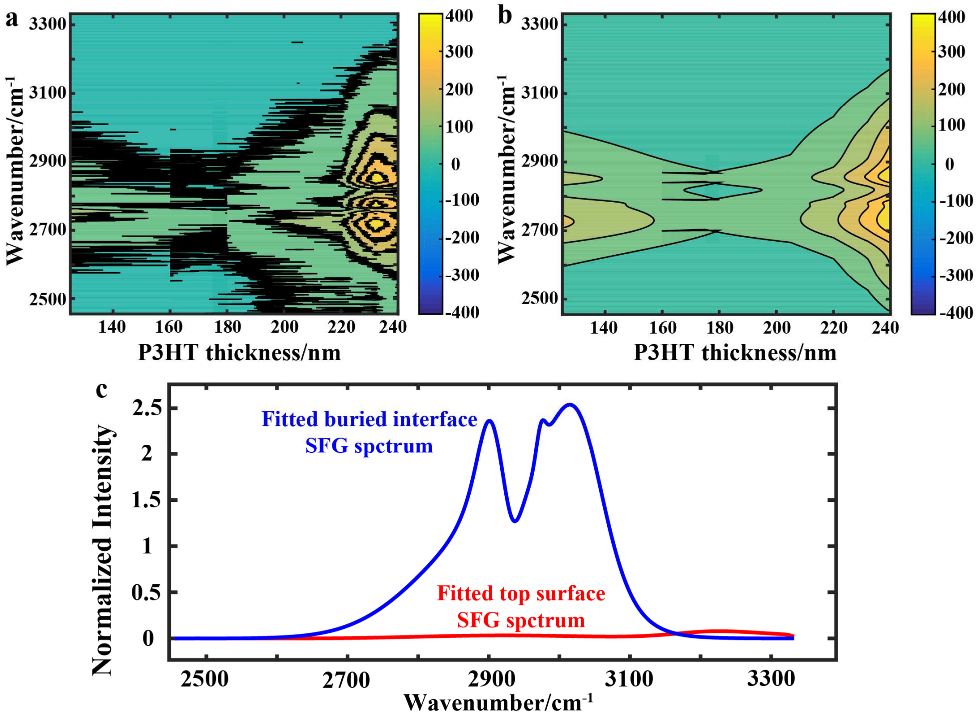

Figure B-2. Simulation results of the two interfaces model. (a) Experimental data shows the SFG spectrum of a series of P3HT/Au sample with different thickness (b) Simulation results that demonstrate VSFG signal intensity generated from different P3HT film thickness. (c) Simulated VSFG spectrum of the buried interface (blue) and the top interface (red). The simulation result agrees well with the experimental spectra. The top interface spectrum shows an almost flat line which suggests negligible amount of signal is generated at air/Au interface. Majority of VSFG signal is generated from the P3HT/Au interface that give rise to the dynamics.

B.2.2 Absorption cross section for Au

In the indirect charge transfer model, where hot electrons in Au are firstly excited by a 790 nm pump pulse and subsequently transfer to the P3HT layer, the amount of charge transferred should be directly related to the number of hot electrons, and therefore, related to the absorption cross section of gold. The absorption cross section of gold under different pump beam polarization are calculated based on Fresnel equations[153]. In this case, absorption cross-section σ_j of gold substrate is given by

$$\sigma_j \sim A_j \rho(\gamma). \tag{B.1}$$

Where j indicates polarization (p or s), $\rho(\gamma)$ is a function of the incident angle γ, and A_j is the absorption coefficient. Since $\rho(\gamma)$ only changes by about 10% as γ varies from 0° to 90°, A_j will be the key factor that determines the value of σ_j. The absorption cross-section A_j is related to the Fresnel coefficients of reflection at the interface as follow

$$A_j = 1 - \left|r_j\right|^2, \tag{B.2}$$

$$r_p = E_p^- / E_p^+ = \left[-n_1^2 cos\gamma + n_0\left(n_1^2 - n_0^2 sin^2\gamma\right)^{\frac{1}{2}}\right] \times \left[n_1^2 cos\gamma + n_0\left(n_1^2 - n_0^2 sin^2\gamma\right)^{\frac{1}{2}}\right]^{-1}, \tag{B.3}$$

$$r_s = E_s^- / E_s^+ = \left[n_0 cos\gamma - \left(n_1^2 - n_0^2 sin^2\gamma\right)^{\frac{1}{2}}\right] \times \left[n_0 cos\gamma + \left(n_1^2 - n_0^2 sin^2\gamma\right)^{\frac{1}{2}}\right]^{-1}, \tag{B.4}$$

where r_p and r_s are amplitude ratios of reflected electric field (E_p^-, E_s^-) to incident electric field (E_p^+, E_s^+), for p and s polarization, γ is the incident angle (~60°), n_0 ($n_0 = 1$) and n_1 ($n_1 = 0.15106\text{-}4.8412i$[265] are the refractive indices of vacuum and metal (Au) at 790 nm, respectively. Based on Eq. B.1-B.4 and the parameters stated above, the ratio of absorption cross-sections of gold substrate at p and s polarization is determined.

$$\frac{\sigma_p}{\sigma_s} \approx \frac{A_p}{A_s} = \frac{1-\left|r_p\right|^2}{1-\left|r_s\right|^2} = 3.7. \tag{B.5}$$

B.2.3 Global analysis methodology

Global analysis is performed using the glotaran software package. We first performed single value decomposition (SVD), and found two types of major dynamics: one dynamic signal that has a negative amplitude and relaxes fast while the other is a positive signal and relaxes slow. To quantify these two types of dynamics, we further carried out global analysis. Details of SVD and global analysis are provided below. In glotaran[194], the raw data matrix is decomposed by SVD method, described by Eq. B.6

$$\Psi(\mathrm{f,t}) = \sum_{i=1}^{n}[u_i(t) \cdot w_i(f) \cdot \sigma_i], \tag{B.6}$$

where Ψ (f, t) is the raw data matrix, $u_i(t)$ and $w_i(f)$ are functions of time(t) and frequency(f), and σ_i is the singular values. The result of singular values is shown below and the corresponding spectra of σ in time and frequency are presented in Fig. B-3.

$$\sigma_1 = 16.86 > \sigma_2 = 1.81 > \sigma_3 = 0.77 > \sigma_4 = 0.56 > \cdots$$

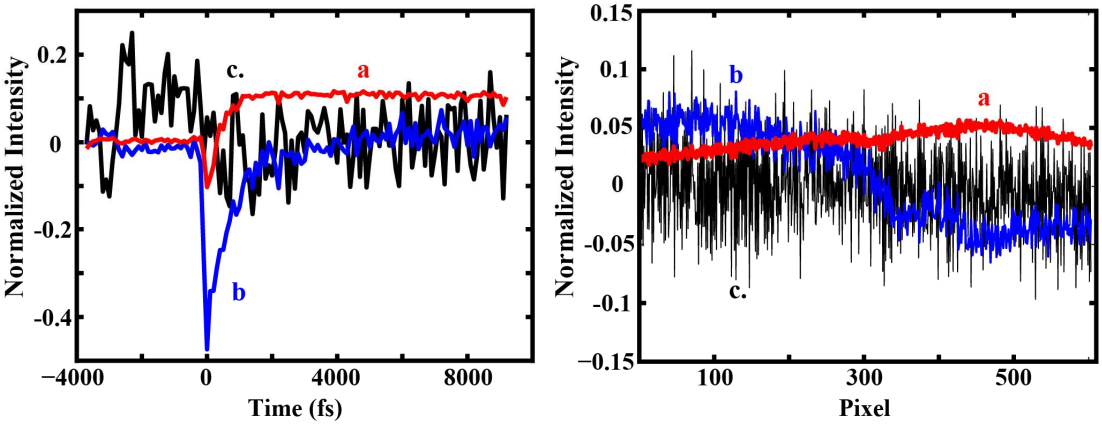

Figure B-3. σ_1, σ_2 and σ_3 correspond to singular values of component a (red), b (blue) and c (black).

From Fig. B-3, it is clear that component c mainly represents noises. Therefore, only two types of dynamic pattern have significant contributions to experimental measurements. Based on this result, the tr-VSFG dynamics are preset as two exponential terms

$$\Psi(f,t) = c_1(t) \cdot \epsilon_1(f) + c_2(t) \cdot \epsilon_2(f)\,, \tag{B.7}$$

where $c_i(t) = A_i\exp(-t/\tau_i)$ and τ_i are relaxation times, while $\varepsilon_i(f)$ are spectral components.

Then, global analysis schema is performed to optimize all the fitting parameters and hence extract two spectral components with their corresponding dynamic trends. The root mean square is minimized during the fitting process.

B.2.4 Absorption cross section and electric transition dipole

The physical cross section is calculated using the following equation[266]:

$$\sigma_{phy} = 1.091(\frac{M}{N_A\rho})^{\frac{2}{3}} = 1.94 \times 10^{-17}\ m^2, \tag{B.8}$$

where M is the molar mass of the P3HT molecule (60000 g/mol), ρ is the mass density (1.3×10^6 g/m^3), and N_A is the Avogadro number. From the calculation shown in last section, we know the photon-to-charge conversion efficiency η. Assuming that every absorbed photon injects an electron, we can estimate the absorption cross section:

$$\sigma_{abs} = \sigma_{phy} \times\ \eta = 4.85 \times 10^{-21} m^2. \tag{B.9}$$

Then, the electronic transition dipole μ is given by

$$\mu^2 = \frac{3\sigma_{abs}\varepsilon_0 hc}{2\pi^2 \upsilon g(\upsilon - \upsilon_0)}, \tag{B.10}$$

where ε_0 is vacuum permittivity, h is plank constant, c is the velocity of light, υ is the frequency of the incident beam, and $g(\upsilon - \upsilon_0)$ is the lineshape function. Then, we obtain the transition dipole moment to be about 5 Debye.

B.2.5 Frequency resolved spectra of tr-VSFG at on- and off- resonance conditions

Although the “integrated” tr-VSFG traces of on- and off-resonance conditions are similar, they are significant different when taking the frequency-resolved spectra into account. We performed SVD (Fig. B-4a, and b) on off-resonance data and found that only one spectral component is significant. This indicates that it is not possible to determine whether the observed dynamics is originated from a single charge dynamics or more than one by only analyzing off-resonance spectral resolved tr-VSFG. This result is further confirmed after performing global analysis on the off-resonance signal (Fig. B-4e and f). When we force the program to break the dynamics into two components, the results show that the two spectral components are nearly identical (Fig. B-4e). These results differ significantly from the global analysis results of on-resonance data. The on-resonance results (Fig. B-4c and d) show that two distinct spectral components exist with independent dynamical behavior, which we attribute to two different interfacial conformations. This insight is inaccessible by off-resonance experiments.

The difference between on-resonance and off-resonance signals is explained by considering that both conformations respond to photoexcitation and cause VSFG signal to change in on-resonance experiments. When the IR pulse resonantly probes vibrational modes of both conformations, the two conformations exhibit slightly different vibrational spectra responses due to their different structures. As a result, the charge dynamics in the two conformations can be directly traced back to the corresponding vibrational features, which thus make them distinguishable through subtle differences in the VSFG spectra. By contrast, when the IR pulse is off-resonant, vibrational modes are not probed by VSFG experiments, which instead only measure non-resonant electronic responses. This results in indistinguishable off-resonant spectra for the two conformations despite the fact the two conformations exhibit distinct charge dynamics. The comparison between on- and off-resonance signals demonstrates the importance of spectral- and time-resolved tr-VSFG, which is an essential tool to resolve the interfacial dynamics with molecular conformation specificity.

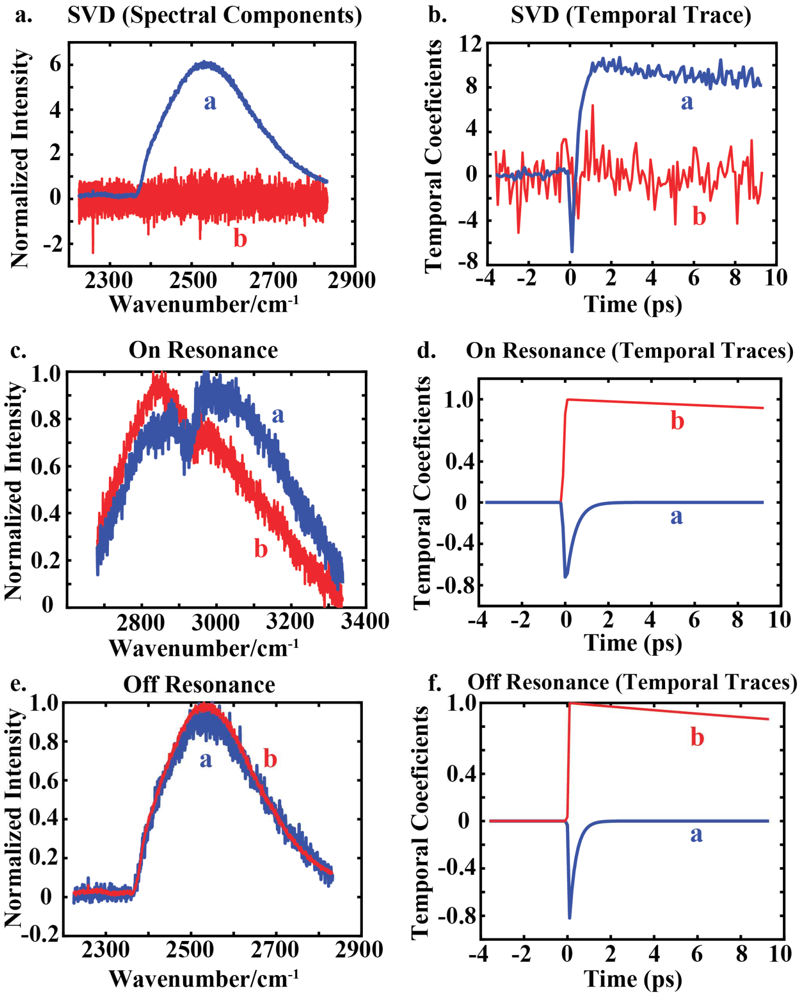

Figure B-4. (a). Spectral components of SVD; (b). Temporal traces of SVD; (c). Spectral components of global analysis results of on-resonance data matrix; (d). Time traces of global analysis results of on-resonance data matrix; (e). Spectral components of global analysis results of off-resonance data matrix; (f). Time traces of global analysis results of off-resonance data matrix.

B.3 Tr-VSFG supplemental figures

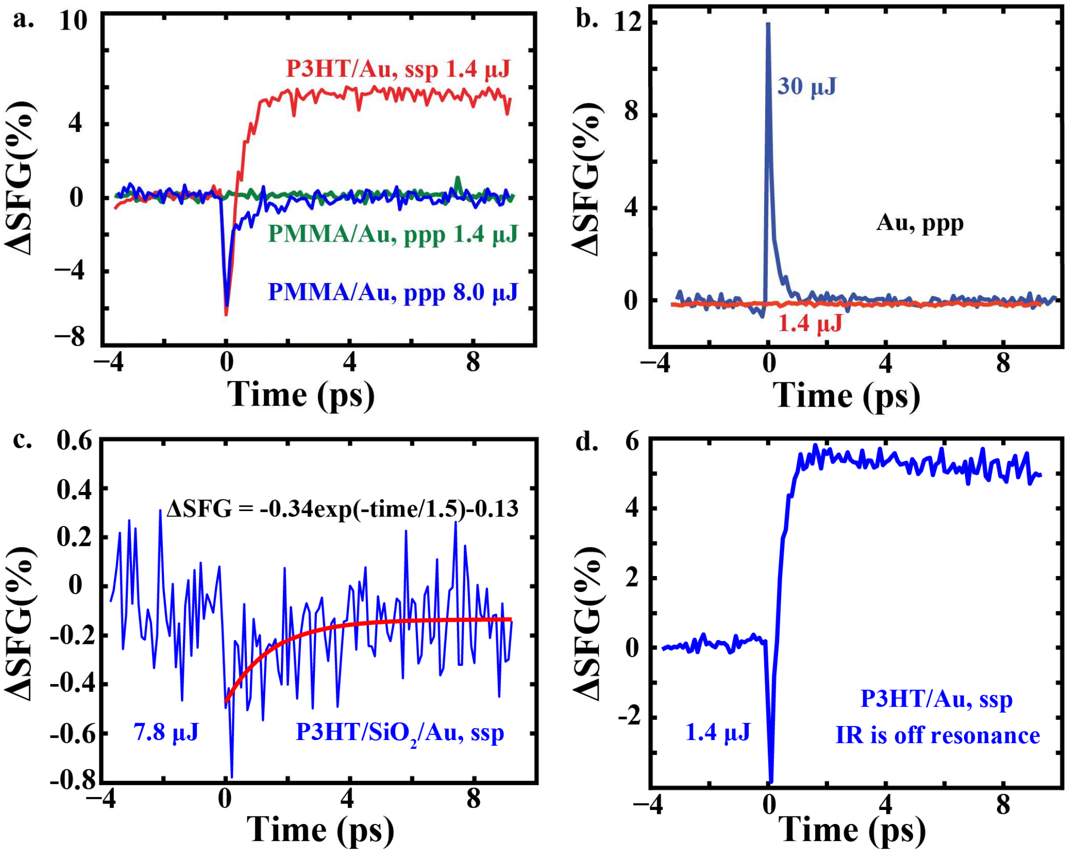

Figure B-5. tr-VSFG dynamics of the control experiments (a) No dynamics is observed at PMMA/Au interface (green) while under the same pump fluence (1.4 μJ) P3HT/Au interface (red) shows a feature dynamics. This result shows no thermal effect is modulating the absorption cross section that can generate a fake dynamic trace. (b) Bare gold surface shows a spike at time zero under high pump power (blue) which is assigned to coherent artifact, whereas no dynamics shows up under low pump power (red). The lifetime of coherent artifact is determined to be 150 fs. (c) P3HT/SiO2 interface gives rise to a slight negative dynamic trace under high pump power (7.8 μJ). This indicates the intrinsic transition of P3HT layer can be pumped through multiphoton absorption pathway under high pump power, while low pump power (1.4 μJ) isn't enough to enable this pathway. (d) tr-VSFG of P3HT/Au when IR center wavelength is tuned to 3.8 μm which is off resonance to the C-H vibrational modes in P3HT.

ΔSFG is calculated using the following equations:

$$I_{pumpon} = \left|\chi^{(2)} E_{IR} E_{vis} + \chi^{(3)} E_{IR} E_{vis} E_{DC}\right|^2. \tag{B.11}$$

$$I_{pumpoff} = \left|\chi^{(2)} E_{IR} E_{vis}\right|^2. \tag{B.12}$$

$$\Delta SFG(\%) = \frac{I_{pumpon} - I_{pumpoff}}{I_{pumpoff}} \sim \frac{2Real(\chi^{(3)} E_{IR} E_{vis} E_{DC})}{\chi^{(2)} E_{IR} E_{vis}}. \quad \text{(B.13)}$$

This interpretation that interfacial electric fields contribute to the tr-VSFG signal is supported by the fact that we observe the same tr-VSFG dynamics, independent of whether the IR pulse frequency is tuned on and off the vibrational resonance of P3HT. (Fig. B-5d) At off-resonance, VSFG is resulted from molecular electronic polarizations, and therefore is similar to second harmonic generation (SHG). Thus, the fact that similar dynamics is observed in tr-VSFG at off-resonance condition indicates tr-VSFG has the same physical origins as time resolved electric field induced second harmonic (tr-EFISH) experiment, which makes it sensitive to interfacial electric fields.

Appendix C

C.1 Preparation of Re(4,4′-dicyano-2,2′-bipyridine)$(CO)_3Cl$

The synthesis, characterization, and X-ray structure of Re(4,4′-dicyano-2,2′-bipyridine)$(CO)_3Cl$ was reported in a separate publication.[267] Optically flat Au substrates consist of a layer of Cr (1-4nm) and Au (200-300nm) evaporated onto borosilicate glass slides. For surface attachment of the catalysts, the gold coated slide was cleaned using a Bunsen Burner method[268] before being immediately submerged in a 1 mM solution of the complex in chloroform for three days in the dark. The sample was then washed with pentane and dried under a stream of nitrogen before use.

C.2 HD 2D SFG spectrometer

Heterodyne 2D Sum Frequency Generation (HD 2D SFG) spectrum[269] is collected using pump-probe geometry as shown in Fig. C-1, with additional narrow band (fwhm~1.5 nm) 800 nm pulse for the SFG process. In brief, three mid-IR pulses are sent to interact with the molecular sample, where three vibrational coherences are created during t_1, t_2, and t_3 period, and the picosecond 800 nm pulse is used to interact with the third vibrational coherence for sum frequency generation process.

To generate the pulse sequence, 800 nm laser pulses (~35 fs, ~6 W, 1 kHz) are generated by ultrafast Ti:Sapphire regenerative amplifier (Astrella, Coherent) . The 800nm is then converted into mid-IR pulses by optical parametric amplifier (TOPAS, Coherent) followed by a different frequency generation process using a Type II $AgGaS_2$ crystal (Eksma). The mid-IR pulse (50 μJ) is split into two by a CaF_2 beam-splitter. The majority (95%) is sent into a Ge-AOM based pulse shaper (QuickShape, PhaseTech[270,271]) to prepare the first two mid-IR pulses (served as pump pulses) in the pulse sequences, whereas 5% mid-IR served as the probe. The residue 800 nm beam after the OPA is narrowed to <1.5

nm by an interference-based notch filter. The pump pulse pair (4 μJ at the sample), the probe (1 μJ) and the 800 nm upconversion pulse (< 2 μJ) are all focused and spatially overlapped on the sample by a f = 10 cm parabolic mirror.

During the mid-IR pulse interactions, three vibrational coherences are generated during t_1, t_2, and t_3 periods, respectively. The first coherence is measured by scanning the t_1 time from 0 to 2500 fs in steps of 20 fs using the pulse shaper, where a rotating frame at f_0=1583 cm^{-1} is used to shift the oscillation period to 80 fs, so that the scanning step can meet with the Nyquist frequency requirement. To remove scatter and linear SFG signal, instead of taking the difference between pump on and off SFG spectra, the difference SFG spectra at the same t_1 but with different pump pulse phase are recorded, which is known as phase cycling.[270] The second vibrational coherence happens during t_2 which is the interstate vibrational coherence. The time delay between the pump pulses and the probe pulse is controlled by a computerized motor stage. The third coherence is upconverted to a virtue state by a picosecond 800 nm pulse and subsequently emits visible signals through sum frequency generation process. Since the 800 nm serves as a window function, the t_3 time delay are simultaneously covered by the upconversion process and the 800 nm pulse duration determines how long t_3 is “scanned”.[83,87] The SFG signals are heterodyned by the local oscillator from non-resonance signal from gold surface and experimentally Fourier transformed by a spectrograph and detected by a CCD camera (400×1,340, Andor). To get full 2D absorptive SFG spectra, the first vibrational coherence is numerical Fourier transformed into frequency domain.

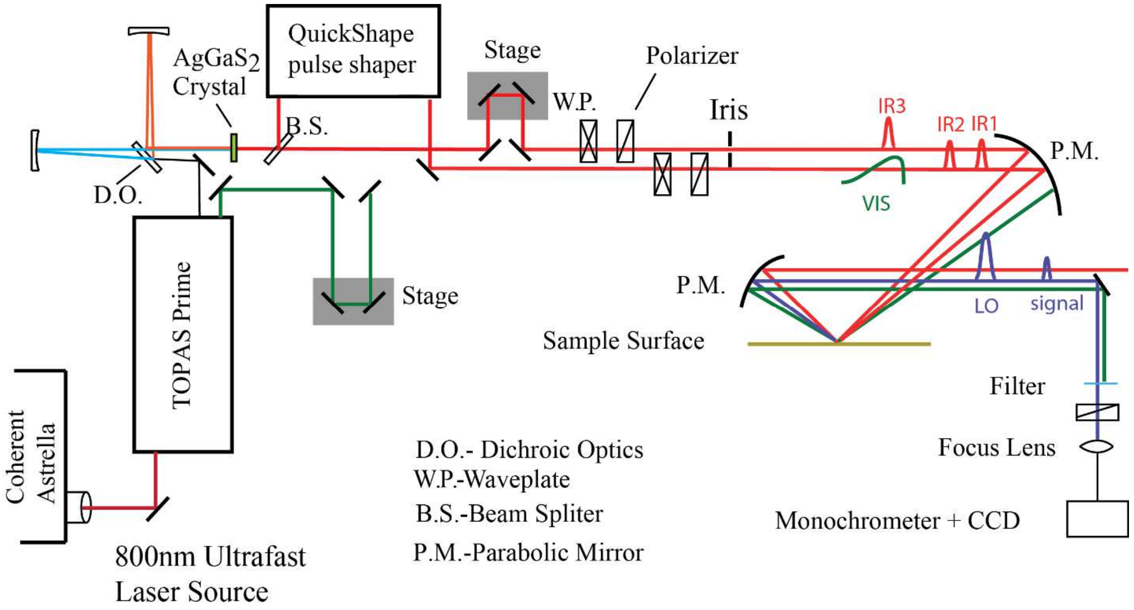

Figure C-1. Layout of HD 2D SFG spectrometer.

SFG of bare gold was also collected as the reference for phase calibrations, details can be found in the previous publication.[10] The HD 2D SFG signal is measured at ppppp polarization, where the polarizations of all pulses are set to be p (in plane with the surface normal-incidence beam plane) to the sample, by pairs of waveplates and polarizers, and only p polarized signal is detected. We note in both our experiment and many other SFG experiments gold surfaces are used as the substrate, which generate the non-resonance SFG signal. In both experiments, the gold SFG signal can interfere with the SFG signal of interests. Therefore, in principle, both experiments are self-heterodyned. The difference between our heterodyne detection scheme and the other SFG experiments, is that the measured self-heterodyne spectrum is further phase corrected by the reference SFG spectrum from bare gold, following the methods by Tahara.[11] In this way, we can extract both the real and imaginary part of the SFG spectra, whereas other experiments does not phase correct the spectrum and take advantage of this self-heterodyne scenario. The samples are constantly rastered between each scan (~10 mins) to avoid sample damaging.

To improve signal to noise ratio, multiple scans are averaged for each time step.

C.3 Illustration of the vibrational modes

The carbonyl vibrational modes we investigated are illustrated in Fig. C-2

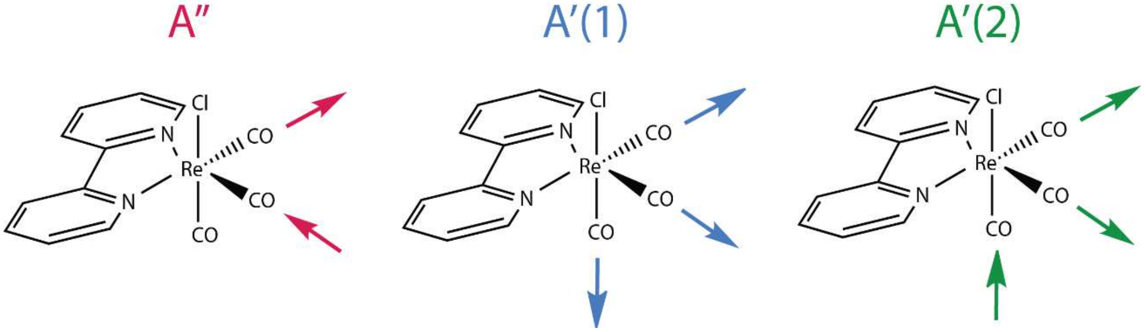

Figure C-2. The carbonyl vibrational modes in the Re-complex studied here. A" is the asymmetric vibrational modes, A'(1) is the symmetric mode and A'(2) is the out of phase symmetric mode

Appendix D

D.1 Sea salt composition

Table D-1. Sea salt composition

Composition	**Concentration**
Chloride (Cl)	19000 – 20000 mg/L
Sodium	10700 – 11000 mg/L
Sulfate	2660 mg/L
Potassium	300 – 400 mg/L
Calcium	400 mg/L
Carbonate	140 – 200 mg/L
Boron	5.6 mg/L
Magnesium	1320 mg/L
Strontium	8.8 mg/L
Insoluble Matter	≤ 0.05 %

D.2 Supporting figures for Chapter 7

VSFG spectrum of sea salt solution.

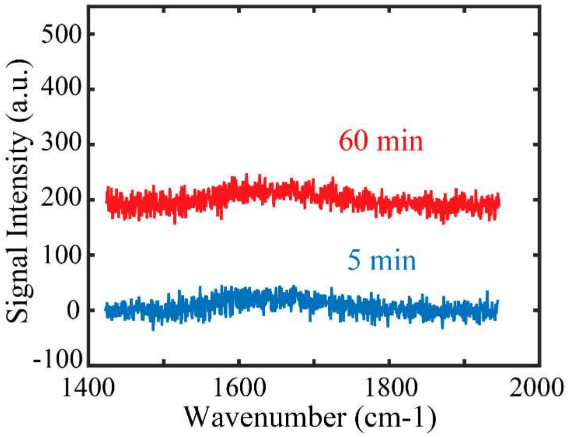

Figure D-11. VSFG spectra of air/salt water interface at different waiting times. Blue trace shows the SFG signal from salt water surface after 5 minutes while red trace displays the SFG signal after 60 minutes of waiting time. Both spectra contain a small bump, which is assigned to nonresonant signal of D_2O.

In order to make sure the air/salt water interface doesn't generate any dynamics, we performed a control experiment of salt water system. As shown in Fig. D-1, the VSFG spectra collected at the early waiting time (5 min) and the later waiting time (60 min) show no spectral difference. The small bump at around 1600 cm^{-1} is assigned to the nonresonant signal of D_2O. The integrated VSFG signal of air/salt water interface shows no change over

60 minutes (Fig. D-2) which indicates salt water solution won't generate artifacts in the protein adsorption kinetics. Another control experiment we performed is to test the VSFG kinetics of BSA in pure water (D_2O). From Fig. D-3, we learned that VSFG signal at the air/ pure water interface remain the same in 60 minutes which suggests no ordered BSA molecules on the surface. This also confirms that the adsorption kinetics we observed in BSA salt solution is induced by the addition of sea salt.

VSFG kinetics of sea salt solution.

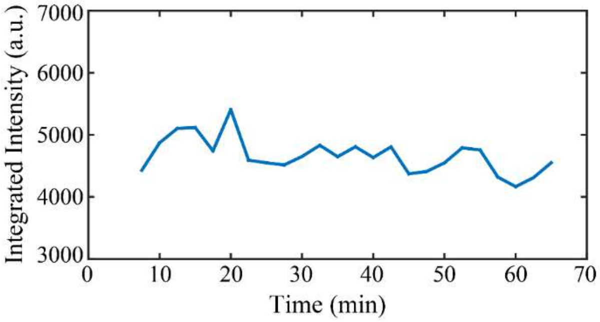

Figure D-2. Dynamic study of VSFG signal at the air/salt water interface. Over the measurement course of > 60 minutes, no SFG signal change is observed.

VSFG kinetics of BSA in pure water (D_2O)

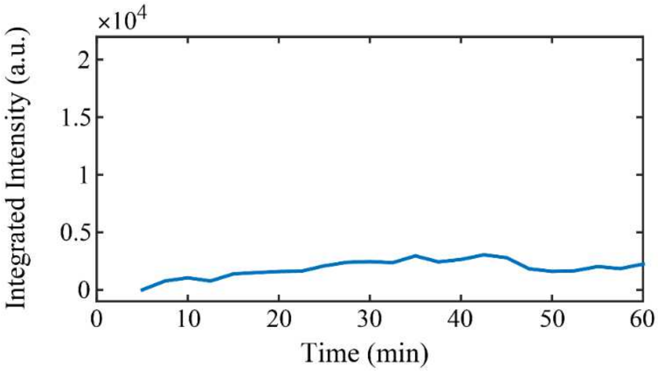

Figure D-3. Dynamic study of VSFG signal at the air/ pure water interface. No SFG signal from BSA is observed within 60 minutes, indicating no ordered BSA molecules on the surface within this time period.

Surface pressure of BSA in pure water (H_2O).

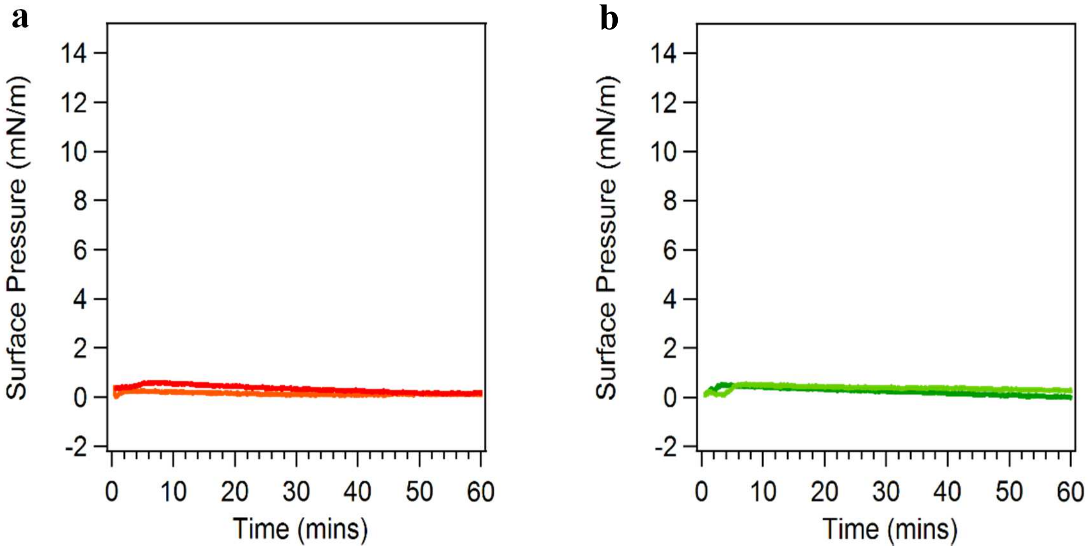

Figure D-4. Surface pressure of BSA pure water solution of different concentrations: (a) 2 ppm, (b) 5 ppm. Both concentration show no surface pressure change for 60 minutes, which suggests there are no more BSA molecules accumulating on the surface.

We measured the surface pressure of BSA pure water solution at two different concentrations: 2 ppm and 5 ppm (Fig. D-4). Both concentrations show no surface pressure change for 60 minutes, which suggests there are no more BSA molecules accumulating on the surface. This observation is in sharp contrast to the adsorption kinetics in salt solution and show the essential role played by the salt ions. The dynamic light scattering measurement result shows no aggregation forming in the BSA salt water solutions at even higher salt concentration (1000 ppm), which indicates the “salting up” effect is different from “salting out”.

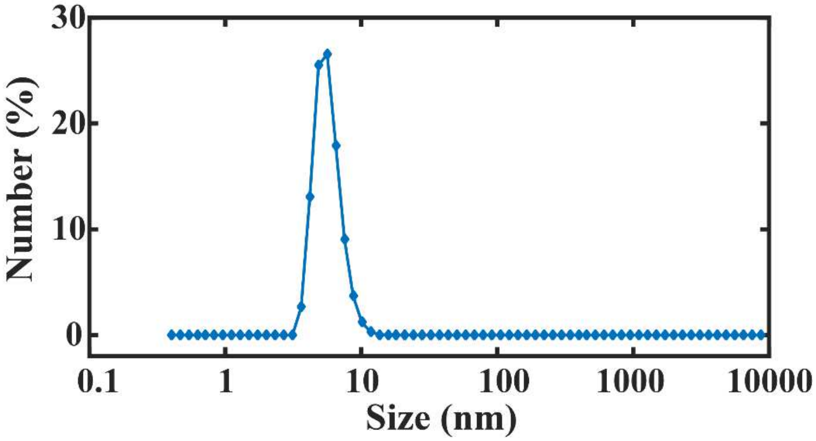

Figure D-5. Dynamic light scattering result (particle size reported as diameter). DLS result shows no aggregation forming in the BSA salt water solutions. BSA concentration: 1000 ppm

Dynamic light scattering of BSA in salt water.

A method to calculate BSA surface coverage based on data from Ref 255

The surface coverage is determined based on Fig. D-6 (from Ref 255). Based on Figure 7-2.b – d in the main manuscript, we can find the surface pressure ratio between the bending point and the equilibrium state for 3, 4, and 5 ppm BSA solutions, which are 0.556, 0.560 and 0.545 (0.554 in average). We find the surface pressure that matches this ratio in the lower panel of Fig. D-6, and identify the corresponding timing for 2 and 5 ppm. Then, the surface concentration at these timings can be identified in the upper panel, and it is found to be 0.82 mg/m^2 for both 2 and 5 ppm. (see blue dashed lines) The equilibrium surface concentration is determined to be 0.92 mg/m^2. (red solid line). Therefore, the

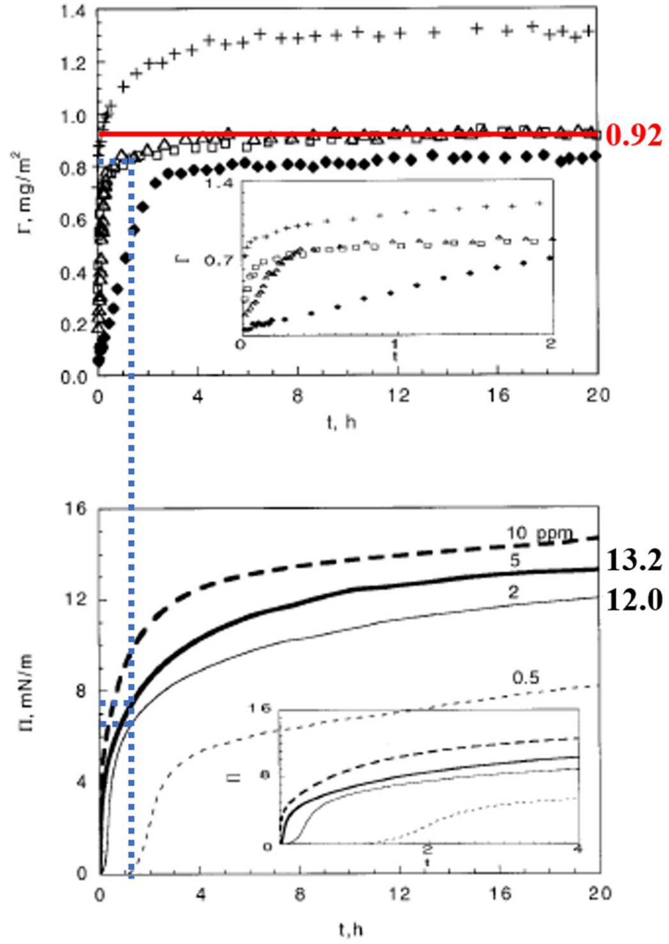

Figure D-6. Reprint from Ref. 255. The red solid line indicates the equilibrium surface coverage of 2ppm and 5 ppm BSA solutions. The blue dashed lines show how we determine the surface coverage of BSA solutions at bending point.

surface coverage of 2 and 5 ppm BSA solutions at the bending in the curve is estimated to be 90% ± 2%.

Surface pressure of lysozyme and lipase in NaCl solution.

Two more proteins, lysozyme and lipase, are studied using surface pressure measurement to see if "salting up" is a general effect to all proteins. The results are summarized in Fig. D-7 where both proteins show no surface pressure change after 60 minutes. The surface pressure difference between the protein water solutions and its salt solutions is induced by the electrostatic interactions between salt ions and water molecules. The surface pressure increases more with higher salt concentration.

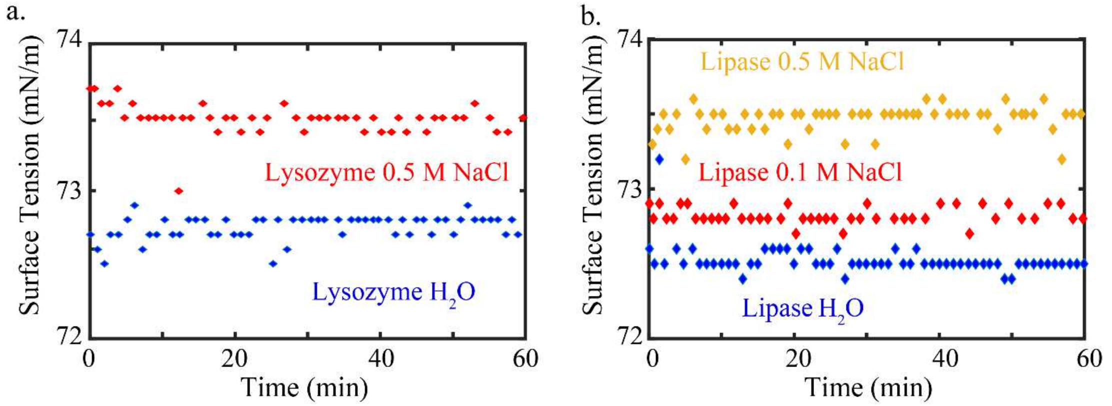

Figure D-7. Surface pressure of (a) lysozyme NaCl solution and (b) lipase NaCl solution. The two proteins have the same molarity as 5 ppm BSA solution. Both proteins show no surface pressure change for 60 minutes in either NaCl solution or water solution, which suggests there is no protein molecules accumulating on the surface.

Surface pressure of BSA in NaCl solution (pH=3).

The electrostatic point of BSA is about pH = 4.7, which means the BSA molecules are negatively charged when the pH value is about 8.5. On the other hand, the electrostatic point of lysozyme and lipase is higher than 8.5 which means they're positively charged. To check the role of charge type, we tune the pH of BSA NaCl solution (salt concentration = 0.5 M) to be 3 where the BSA molecules would be positively charged. As shown in Fig. D-8, the increasing surface pressure indicates BSA molecules appear at surface when positively charged. Therefore, "salting up" effect isn't induced by the type of charge of protein molecules.

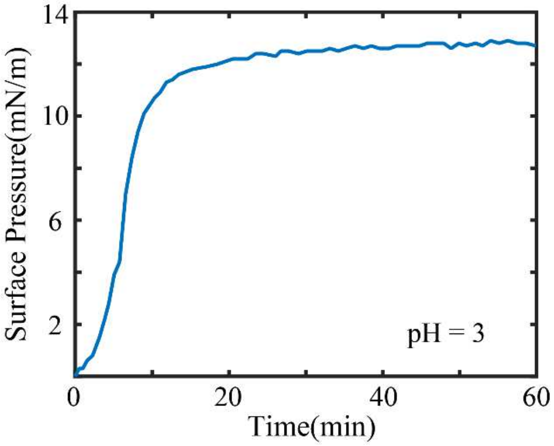

Figure D-8. Surface pressure of BSA NaCl solution at low pH value (pH=3). At pH=3 which is below the isoelectric point of BSA, the protein molecules are positively charge. The surface pressure result shows that BSA molecules appear at surface and reach to equilibrium in 20 min. This indicates the "salting up" effect of BSA doesn't depend on the charge type of proteins.

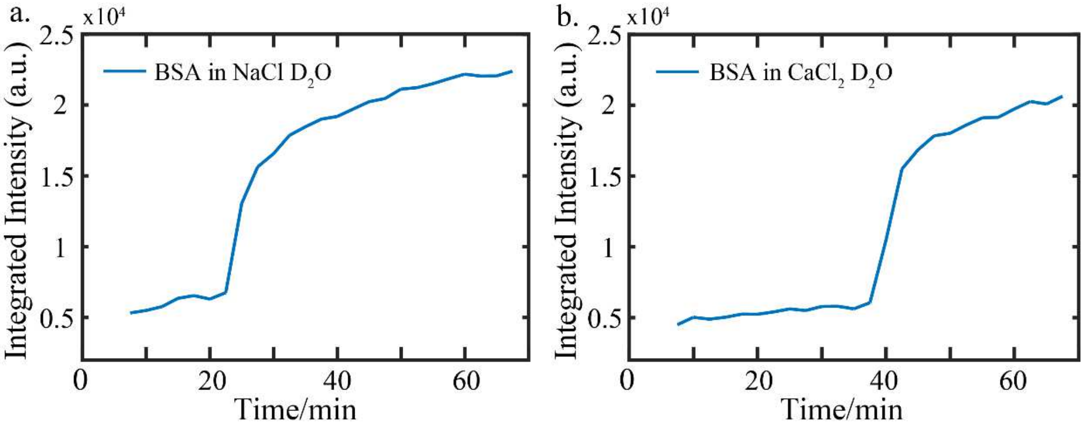

Figure D-9. Dynamic study of VSFG signal at (a) air/NaCl solution interface and (b) air/$CaCl_2$ solution interface. Both systems show a steep increase of VSFG signal, which indicates both salts can induce the "salting up" effect of BSA molecules.

VSFG kinetics of different salt solutions

To test if "salting up" effect is induced by specific type of ions in sea salt. We performed an ion specific experiment where we prepared 3 ppm BSA in two different salt solutions: NaCl and $CaCl_2$, where the salt concentrations are the same as in sea salt. The results shown in Fig. D-9 indicate both type of salts could induce the "salting up" phenomenon of BSA molecules.

References

(1) Kroemer, H. Nobel Lecture : Quasielectric Fields and Band Offsets : Teaching Electrons New Tricks *. *Rev. Mod. Phys.* **2001**, *73* (July), 783–793.

(2) Luo, Y.; Collier, C. P.; Jeppesen, J. O.; Nielsen, K. A.; Deionno, E.; Ho, G.; Perkins, J.; Tseng, H.; Yamamoto, T.; Stoddart, J. F.; et al. Two-Dimensional Molecular Electronics Circuits. *CHEMPHYSCHEM* **2002**, *3*, 519–525.

(3) Tour, J. M. Molecular Electronics . Synthesis and Testing of Components. *Acc. Chem. Res.* **2000**, *33* (11), 791–804.

(4) Sharma, S.; Jain, K. K.; Sharma, A. Solar Cells : In Research and Applications — A Review. *Mater. Sci. Appl.* **2015**, *6* (December), 1145–1155.

(5) Wang, J.; Clark, M. L.; Li, Y.; Kaslan, C. L.; Kubiak, C. P.; Xiong, W. Short-Range Catalyst-Surface Interactions Revealed by Heterodyne Two-Dimensional Sum Frequency Generation Spectroscopy. *J. Phys. Chem. Lett.* **2015**, *6* (21), 4204–4209.

(6) Li, Y.; Wang, J.; Clark, M. L.; Kubiak, C. P.; Xiong, W. Characterizing Interstate Vibrational Coherent Dynamics of Surface Adsorbed Catalysts by Fourth-Order 3D SFG Spectroscopy. *Chem. Phys. Lett.* **2016**, *650*, 1–6.

(7) Snodgrass, J. M.; Pantelidis, D.; Jenkins, M. L.; Bravman, J. C.; Dauskardt, R. H. Subcritical Debonding of Polymer/Silica Interfaces under Monotonic and Cyclic Loading. *Acta Mater.* **2002**, *50*, 2395–2411.

(8) Wang, J.; Chen, X.; Clarke, M. L.; Chen, Z. Detection of Chiral Sum Frequency Generation Vibrational Spectra of Proteins and Peptides at Interfaces in Situ. *Proc. Natl. Acad. Sci. U.S.A.* **2005**, *102* (14), 4978–4983.

(9) Umbach, E.; Glockler, K.; Sokolowski, M. Surface '"Architecture"' with Large Organic Molecules: Interface Order and Epitaxy. *Surf. Sci.* **1998**, *404*, 20–31.

(10) Ershov, D.; Sprakel, J.; Appel, J.; Stuart, M. A. C.; Gucht, J. Van Der. Capillarity-Induced Ordering of Spherical Colloids on an Interface with Anisotropic Curvature. *Proc. Natl. Acad. Sci.* **2013**, *110* (23), 9220–9224.

(11) Gozar, A.; Logvenov, G.; Kourkoutis, L. F.; Bollinger, A. T.; Giannuzzi, L. A.; Muller, D. A.; Bozovic, I. High-Temperature Interface Superconductivity between Metallic and Insulating Copper Oxides. *Nature* **2008**, *455* (7214), 782–785.

(12) Ohtomo, A.; Hwang, H. Y. A High-Mobility Electron Gas at the LaAlO 3 / SrTiO 3 Heterointerface. *Nature* **2004**, *427* (January), 423–427.

(13) Caviglia, A. D.; Gabay, M.; Gariglio, S.; Reyren, N.; Cancellieri, C.; Triscone, J.-M. Tunable Rashba Spin-Orbit Interaction at Oxide Interfaces. *Phys. Rev. Lett.* **2010**, *104* (12), 126803.

(14) Ghaemi, H. F.; Thio, T. Extraordinary Optical Transmission through Sub-Wavelength

Hole Arrays. *Nature* **1998**, *391* (February), 667–669.

(15) Bhattacharya, A.; May, S. J.; Te Velthuis, S. G. E.; Warusawithana, M.; Zhai, X.; Jiang, B.; Zuo, J. M.; Fitzsimmons, M. R.; Bader, S. D.; Eckstein, J. N. Metal-Insulator Transition and Its Relation to Magnetic Structure in (LaMnO3)2n/(SrMnO3)n Superlattices. *Phys. Rev. Lett.* **2008**, *100* (25), 1–4.

(16) Yamada, H.; Kawasaki, M.; Lottermoser, T.; Arima, T.; Tokura, Y. LaMnO3/SrMnO3 Interfaces with Coupled Charge-Spin-Orbital Modulation. *Appl. Phys. Lett.* **2006**, *89* (5), 4–7.

(17) Hosono, H. Recent Progress in Transparent Oxide Semiconductors : Materials and Device Application. *Thin Solid Films* **2007**, *515*, 6000–6014.

(18) Li, M.-Y.; Shi, Y.; Cheng, C.-C.; Lu, L.-S.; Lin, Y.-C.; Tang, H.-L.; Tsai, M.-L.; Chu, C.-W.; Wei, K.; He, J.-H.; et al. Epitaxial Growth Ofa Monolayer WSe2-MoS2 Lateral p-n Junction with an Atomically Sharp Interface. *Science (80-.).* **2015**, *349* (6247), 524–528.

(19) Avouris, P. Molecular Electronics with Carbon Nanotubes. *Acc. Chem. Res.* **2002**, *35* (12), 1026–1034.

(20) Heimel, G.; Romaner, L.; Zojer, E.; Bre, J. Toward Control of the Metal − Organic Interfacial Electronic Structure in Molecular Electronics : A First-Principles Study on Self-Assembled Monolayers of π -Conjugated Molecules on Noble Metals. *Nano Lett.* **2007**, *7* (4), 932–940.

(21) Andrews, D. Q.; Duyne, R. P. Van; Ratner, M. A. Stochastic Modulation in Molecular Electronic Transport Junctions : Molecular Dynamics Coupled with Charge Transport Calculations 2008. *Nano Lett.* **2008**, *8* (4), 1120–1126.

(22) Meyer, G.; Amer, N. M. Novel Optical Approach to Atomic Force Microscopy. *Appl. Phys. Lett.* **1998**, *53* (12), 1045–1047.

(23) Giessibl, F. J. Advances in Atomic Force Microscopy. *Rev. Mod. Phys.* **2003**, *75* (3), 949–983.

(24) Tromp, R. M.; Hamers, R. J.; Demuth, J. E. Si(001) Dimer Structure Observed with Scanning Tunneling Microscopy. *Phys. Rev. Lett.* **1985**, *55* (12), 1303–1307.

(25) Binning, G.; Rohrer, H.; Gerber, C.; Weibel, E. Surface Studies by Scanning Tunneling Microscopy. *Phys. Rev. Lett.* **1982**, *49* (1), 57–61.

(26) Scanlon, D. O.; Dunnill, C. W.; Buckeridge, J.; Shevlin, S. A.; Logsdail, A. J.; Woodley, S. M.; Catlow, C. R. A.; Powell, M. J.; Palgrave, R. G.; Parkin, I. P.; et al. Band Alignment of Rutile and Anatase TiO 2. *Nat. Mater.* **2013**, *12*, 798–801.

(27) Braun, S.; Salaneck, W. R.; Fahlman, M. Energy-Level Alignment at Organic/Metal and Organic/Organic Interfaces. *Adv. Mater.* **2009**, *21* (14–15), 1450–1472.

(28) Chuang, C. M.; Brown, P. R.; Bulović, V.; Bawendi, M. G. Improved Performance and

Stability in Quantum Dot Solar Cells through Band Alignment Engineering. *Nat. Mater.* **2014**, *13* (796–801).

(29) Stamenkovic, V. R.; Mun, B. S.; Mayrhofer, K. J. J.; Ross, P. N.; Markovic, N. M. Effect of Surface Composition on Electronic Structure , Stability , and Electrocatalytic Properties of Pt-Transition Metal Alloys : Pt-Skin versus Pt-Skeleton Surfaces. *J. Am. Chem. Soc.* **2006**, *128* (5), 8813–8819.

(30) Shen, Y. R. Surface Properties Probed by Second-Harmonic and Sum-Frequency Generation. *Nature* **1989**, *337*, 519–525.

(31) Corn, R. M.; Higgins, D. A. Optical Second Harmonic Generation as a Probe of Surface Chemistry. *Chem. Rev.* **1994**, *94*, 107–125.

(32) Tisdale, W. A.; Williams, K. J.; Timp, B. A.; Norris, D. J.; Aydil, E. S.; Zhu, X.-Y. Hot-Electron Transfer from Semiconductor Nanocrystals. *Science (80-.).* **2010**, *328*, 1543–1548.

(33) Miller, R. C.; Miller, R. C. OPTICAL SECOND HARMONIC GENERATION IN PIEZOELECTRIC. *Appl. Phys. Lett.* **1964**, *5* (1), 17–19.

(34) Xiong, W.; Laaser, J. E.; Mehlenbacher, R. D.; Zanni, M. T. Adding a Dimension to the Infrared Spectra of Interfaces Using Heterodyne Detected 2D Sum-Frequency Generation (HD 2D SFG) Spectroscopy. *Proc. Natl. Acad. Sci. U. S. A.* **2011**, *108* (52), 20902–20907.

(35) Fu, L.; Liu, J.; Yan, E. C. Y. Chiral Sum Frequency Generation Spectroscopy for Characterizing Protein Secondary Structures at Interfaces. *J. Am. Chem. Soc.* **2011**, *133*, 8094–8097.

(36) Chen, X.; Hua, W.; Huang, Z.; Allen, H. C. Interfacial Water Structure Associated with Phospholipid Membranes Studied by Phase-Sensitive Vibrational Sum Frequency Generation Spectroscopy. *J. Am. Chem. Soc.* **2010**, *132*, 11336–11342.

(37) Nihonyanagi, S.; Mondal, J. a; Yamaguchi, S.; Tahara, T. Structure and Dynamics of Interfacial Water Studied by Heterodyne-Detected Vibrational Sum-Frequency Generation. *Annu. Rev. Phys. Chem.* **2013**, *64*, 579.

(38) Mondal, J. A.; Nihonyanagi, S.; Yamaguchi, S.; Tahara, T. Structure and Orientation of Water at Charged Lipid Monolayer / Water Interfaces Probed by Heterodyne-Detected Vibrational Sum Frequency. *J. Am. Chem. Soc.* **2010**, *132*, 10656–10657.

(39) Mondal, J. A.; Nihonyanagi, S.; Yamaguchi, S.; Tahara, T. Three Distinct Water Structures at a Zwitterionic Lipid/Water Interface Revealed by Heterodyne-Detected Vibrational Sum Frequency Generation. *J. Am. Chem. Soc.* **2012**, *134*, 7842–7850.

(40) Chou, K. C.; Westerberg, S.; Shen, Y. R.; Ross, P. N.; Somorjai, G. A. Probing the Charge-Transfer State of CO on Pt (111) by Two-Dimensional Infrared-Visible Sum Frequency Generation Spectroscopy. *Phys. Rev. B* **2004**, *69*, 153413.

(41) Tisdale, W. A.; Williams, K. J.; Timp, B. A.; Norris, D. J.; Aydil, E. S.; Zhu, X. Hot-

Electron Transfer from Semiconductor Nanocrystals. *Science (80-.).* **2010**, *328*, 1543–1548.

(42) Anglin, T. C.; O'Brien, D. B.; Massari, A. M. Monitoring the Charge Accumulation Process in Polymeric Field-Effect Transistors via in Situ Sum Frequency Generation Timothy. *J. Phys. Chem. C* **2010**, *114*, 17629–17637.

(43) Anglin, T. C.; Speros, J. C.; Massari, A. M. Interfacial Ring Orientation in Polythiophene Field-Effect Transistors on Functionalized Dielectrics. *J. Phys. Chem. C* **2011**, *115* (32), 16027–16036.

(44) Veinot, J. G. C.; Marks, T. J. Toward the Ideal Organic Light-Emitting Diode. The Versatility and Utility of Interfacial Tailoring by Cross-Linked Siloxane Interlayers. *Accounts of Chemical Research*. 2005, pp 632–643.

(45) Dhar, P.; Khlyabich, P. P.; Burkhart, B.; Roberts, S. T.; Malyk, S.; Thompson, B. C.; Benderskii, A. V. Annealing-Induced Changes in the Molecular Orientation of Poly-3-Hexylthiophene at Buried Interfaces. *J. Phys. Chem. C* **2013**, *117* (29), 15213–15220.

(46) O'Brien, D. B.; Massari, A. M. Experimental Evidence for an Optical Interference Model for Vibrational Sum Frequency Generation on Multilayer Organic Thin Film Systems. II. Consideration for Higher Order Terms. *J. Chem. Phys.* **2015**, *142* (2), 024704.

(47) Bakulin, A. a; Rao, A.; Pavelyev, V. G.; van Loosdrecht, P. H. M.; Pshenichnikov, M. S.; Niedzialek, D.; Cornil, J.; Beljonne, D.; Friend, R. H. The Role of Driving Energy and Delocalized States for Charge Separation in Organic Semiconductors. *Science (80-.).* **2012**, *335* (6074), 1340–1344.

(48) Jailaubekov, A. E.; Willard, A. P.; Tritsch, J. R.; Chan, W. L.; Sai, N.; Gearba, R.; Kaake, L. G.; Williams, K. J.; Leung, K.; Rossky, P. J.; et al. Hot Charge-Transfer Excitons Set the Time Limit for Charge Separation at Donor/Acceptor Interfaces in Organic Photovoltaics. *Nat. Mater.* **2013**, *12* (1), 66–73.

(49) Zhu, X.-Y.; Monahan, N. R.; Gong, Z.; Zhu, H.; Williams, K.; Nelson, C. a. Charge Transfer Excitons at van Der Waals Interfaces. *J. Am. Chem. Soc.* **2015**, *137*, 8313–8320.

(50) Jackson, N. E.; Kohlstedt, K. L.; Savoie, B. M.; Olvera de la Cruz, M.; Schatz, G. C.; Chen, L. X.; Ratner, M. a. Conformational Order in Aggregates of Conjugated Polymers. *J. Am. Chem. Soc.* **2015**, *137*, 6254–6262.

(51) Ishii, H.; Hayashi, N.; Ito, E.; Washizu, Y.; Sugi, K.; Kimura, Y.; Niwano, M.; Ouchi, Y.; Seki, K. Kelvin Probe Study of Band Bending at Organic Semiconductor/Metal Interfaces: Examination of Fermi Level Alignment. *Phys. Status Solidi Appl. Res.* **2004**, *201* (6), 1075–1094.

(52) Wang, H.; Amsalem, P.; Heimel, G.; Salzmann, I.; Koch, N.; Oehzelt, M. Band-Bending in Organic Semiconductors: The Role of Alkali-Halide Interlayers. *Adv. Mater.* **2014**, *26* (6), 925–930.

(53) Ishii K Ito, E Seki, K, H. S. Energy Level Alignment and Interfacial Electronic Structures

at Organic Metal and Organic Organic Interfaces. *Adv. Mater.* **1999**, *11* (8), 605–625.

(54) Paasch, G.; Peisert, H.; Knupfer, M.; Fink, J.; Scheinert, S. Mixing of Interface Dipole and Band Bending at Organic/Metal Interfaces in the Case of Exponentially Distributed Transport States. *J. Appl. Phys.* **2003**, *93* (10 1), 6084–6089.

(55) Osikowicz, W.; de Jong, M. P.; Salaneck, W. R. Formation of the Interfacial Dipole at Organic-Organic Interfaces: C60/Polymer Interfaces. *Adv. Mater.* **2007**, *19* (23), 4213–4217.

(56) Bell, L. D.; Kaiser, W. J. Observation of Interface Band Structure by Ballistic-Electron-Emission Microscopy. *Phys. Rev. Lett.* **1988**, *61* (20), 2368.

(57) Pacchioni, G.; Giordano, L.; Baistrocchi, M. Charging of Metal Atoms on Ultrathin MgO/Mo(100) Films. *Phys. Rev. Lett.* **2005**, *94*, 226104.

(58) Freund, H.-J.; Pacchioni, G. Oxide Ultra-Thin Films on Metals: New Materials for the Design of Supported Metal Catalysts. *Chem. Soc. Rev.* **2008**, *37* (10), 2224–2242.

(59) Eren, B.; Heine, C.; Bluhm, H.; Somorjai, G. a.; Salmeron, M. Catalyst Chemical State during CO Oxidation Reaction on Cu(111) Studied with Ambient Pressure XPS and NEXAFS. *J. Am. Chem. Soc.* **2015**, *137* (34), 11186–11190.

(60) Lim, K.-H.; Kim, K.; Kim, S.; Park, S. Y.; Kim, H.; Kim, Y. S. UV-Visible Spectroscopic Analysis of Electrical Properties in Alkali Metal-Doped Amorphous Zinc Tin Oxide Thin-Film Transistors. *Adv. Mater.* **2013**, 2994–3000.

(61) Mohanty, P.; Rath, C.; Mallick, P.; Biswal, R.; Mishra, N. C. UV-Visible Studies of Nickel Oxide Thin Film Grown by Thermal Oxidation of Nickel. *Phys. B Condens. Matter* **2010**, *405* (12), 2711–2714.

(62) Greiner, M. T.; Lu, Z.-H. Thin-Film Metal Oxides in Organic Semiconductor Devices: Their Electronic Structures, Work Functions and Interfaces. *NPG Asia Mater.* **2013**, *5* (7), e55.

(63) Gearba, R. I.; Mills, T.; Morris, J.; Pindak, R.; Black, C. T.; Zhu, X. Quantifying Interfacial Electric Fields and Local Crystallinity in Polymer-Fullerene Bulk-Heterojunction Solar Cells. *Adv. Funct. Mater.* **2011**, *21* (14), 2666–2673.

(64) Mondal, S. K.; Yamaguchi, S.; Tahara, T. Molecules at the Air/Water Interface Experience a More Inhomogeneous Solvation Environment than in Bulk Solvents: A Quantitative Band Shape Analysis of Interfacial Electronic Spectra Obtained by HD-ESFG. *J. Phys. Chem. C* **2011**, *115* (7), 3083–3089.

(65) Yamaguchi, S.; Tahara, T. Precise Electronic ??(2) Spectra of Molecules Adsorbed at an Interface Measured by Multiplex Sum Frequency Generation. *J. Phys. Chem. B* **2004**, *108* (50), 19079–19082.

(66) Yamaguchi, S.; Tahara, T. Heterodyne-Detected Electronic Sum Frequency Generation: “Up” versus “down” Alignment of Interfacial Molecules. *J. Chem. Phys.* **2008**, *129* (10),

1–4.

(67) Sekiguchi, K.; Yamaguchi, S.; Tahara, T. Femtosecond Time-Resolved Electronic Sum-Frequency Generation Spectroscopy: A New Method to Investigate Ultrafast Dynamics at Liquid Interfaces. *J. Chem. Phys.* **2008**, *128* (11), 114715.

(68) Han, S.; Ji, N.; Belkin, M.; Shen, Y. Sum-Frequency Spectroscopy of Electronic Resonances on a Chiral Surface Monolayer of Bi-Naphthol. *Phys. Rev. B* **2002**, *66* (16), 1–6.

(69) Doughty, B.; Ma, Y.-Z.; Shaw, R. W. Probing Interfacial Electronic States in CdSe Quantum Dots Using Second Harmonic Generation Spectroscopy. *J. Phys. Chem. C* **2015**, *119*, 2752–2760.

(70) Hintz, H.; Egelhaaf, H.-J.; Lüer, L.; Hauch, J.; Peisert, H.; Chassé, T. Photodegradation of P3HT−A Systematic Study of Environmental Factors. *Chem. Mater.* **2011**, *23* (2), 145–154.

(71) Belkin, M. A.; Shen, Y. R.; Flytzanis, C. Coupled-Oscillator Model for Nonlinear Optical Activity. *Chem. Phys. Lett.* **2002**, *363* (September), 479–485.

(72) Lin, C. K.; Hayashi, M.; Lin, S. H. Theoretical Formulation and Simulation of Electronic Sum-Frequency Generation Spectroscopy. *J. Phys. Chem. C* **2013**, *117* (45), 23797–23805.

(73) Fischer, P.; Beckwitt, K.; Wise, F. W.; Albrecht, A. C. The Chiral Specificity of Sum-Frequency Generation in Solutions. *Chem. Phys. Lett.* **2002**, *352* (February), 463–468.

(74) Champagne, B.; Fischer, P.; Buckingham, A. D. Ab Initio Investigation of the Sum-Frequency Hyperpolarizability of Small Chiral Molecules. *Chem. Phys. Lett.* **2000**, *331* (1), 83–88.

(75) Fischer, P.; Buckingham, a.; Albrecht, a. Isotropic Second-Order Nonlinear Optical Susceptibilities. *Phys. Rev. A* **2001**, *64* (5), 053816.

(76) Belkin, M. a.; Kulakov, T. a.; Ernst, K. H.; Yan, L.; Shen, Y. R. Sum-Frequency Vibrational Spectroscopy on Chiral Liquids: A Novel Technique to Probe Molecular Chirality. *Phys. Rev. Lett.* **2000**, *85* (21), 4474–4477.

(77) Belkin, M. a; Han, S. H.; Wei, X.; Shen, Y. R. Sum-Frequency Generation in Chiral Liquids near Electronic Resonance. *Phys. Rev. Lett.* **2001**, *87* (11), 113001.

(78) Fischer, P.; Wiersma, D. S.; Righini, R.; Champagne, B.; Buckingham, a. D. Three-Wave Mixing in Chiral Liquids. *Phys. Rev. Lett.* **2000**, *85* (20), 4253–4256.

(79) Moad, a J.; Simpson, G. J. A Unified Treatment of Symmetry Relations and Selection Rules in Sum-Frequency and Second Harmonic Spectroscopies. *J. Phys. Chem. B* **2004**, *108* (11), 3548–3562.

(80) Auer, B. M.; Skinner, J. L. Vibrational Sum-Frequency Spectroscopy of the Liquid/Vapor

Interface for Dilute HOD in D2O. *J. Chem. Phys.* **2008**, *129* (21).

(81) Wang, H.-F.; Gan, W.; Lu, R.; Rao, Y.; Wu, B.-H. Quantitative Spectral and Orientational Analysis in Surface Sum Frequency Generation Vibrational Spectroscopy (SFG-VS). *International Reviews in Physical Chemistry*. 2005, pp 191–256.

(82) Buchbinder, A. M.; Weitz, E.; Geiger, F. M. Pentane, Hexane, Cyclopentane, Cyclohexane, 1-Hexene, 1-Pentene, Cis-2-Pentene, Cyclohexene, and Cyclopentene at Vapor/α-Alumina and Liquid/α-Alumina Interfaces Studied by Broadband Sum Frequency Generation. *J. Phys. Chem. C* **2010**, *114* (1), 554–566.

(83) Laaser, J. E.; Xiong, W.; Zanni, M. T. Time-Domain SFG Spectroscopy Using Mid-IR Pulse Shaping : Practical and Intrinsic Advantages. *J. Phys. Chem. B* **2011**, *115*, 2536–2546.

(84) Kett, P. J. N.; Casford, M. T. L.; Davies, P. B. Sum Frequency Generation (SFG) Vibrational Spectroscopy of Planar Phosphatidylethanolamine Hybrid Bilayer Membranes under Water. *Langmuir* **2010**, *26* (12), 9710–9719.

(85) Lu, G. Q.; Lagutchev, A.; Dlott, D. D.; Wieckowski, A. Quantitative Vibrational Sum-Frequency Generation Spectroscopy of Thin Layer Electrochemistry: CO on a Pt Electrode. *Surf. Sci.* **2005**, *585* (1–2), 3–16.

(86) Stiopkin, I. V.; Jayathilake, H. D.; Bordenyuk, A. N.; Benderskii, A. V. Heterodyne-Detected Vibrational Sum Frequency Generation Spectroscopy. *J. Am. Chem. Soc.* **2008**, *130*, 2271–2275.

(87) Hommel, E. L.; Allen, H. C. Broadband Sum Frequency Generation with Two Regenerative Amplifiers: Temporal Overlap of Femtosecond and Picosecond Light Pulses. *Anal. Sci.* **2001**, *17* (1), 137–139.

(88) Chen, Z. Investigating Buried Polymer Interfaces Using Sum Frequency Generation Vibrational Spectroscopy. *Prog. Polym. Sci.* **2010**, *35* (11), 1376–1402.

(89) Eisenthal, K. B. Equilibrium and Dynamic Processes At Interfaces By Second Harmonic and Sum Frequency Generation. *Ann. Rev. Phys. Chem.* **1992**, *43*, 627.

(90) Shen, Y. R. Basic Theory of Surface Sum-Frequency Generation. *J. Phys. Chem. C* **2012**, *116* (29), 15505–15509.

(91) Herrmann, D.; Niesar, S.; Scharsich, C.; Köhler, A.; Stutzmann, M.; Riedle, E. Role of Structural Order and Excess Energy on Ultrafast Free Charge Generation in Hybrid Polythiophene/Si Photovoltaics Probed in Real Time by near-Infrared Broadband Transient Absorption. *J. Am. Chem. Soc.* **2011**, *133* (45), 18220–18233.

(92) Morgenstern, F. S. F.; Rao, A.; Böhm, M. L.; Kist, R. J. P.; Vaynzof, Y.; Greenham, N. C. Ultrafast Charge- and Energy-Transfer Dynamics in Conjugated Polymer: Cadmium Selenide Nanocrystal Blends. *ACS Nano* **2014**, *8* (2), 1647–1654.

(93) Song, Y.; Clafton, S. N.; Pensack, R. D.; Kee, T. W.; Scholes, G. D. Vibrational

Coherence Probes the Mechanism of Ultrafast Electron Transfer in Polymer-Fullerene Blends. *Nat. Commun.* **2014**, *5*, 4933.

(94) Park, H.; Gutierrez, M.; Wu, X.; Kim, W.; Zhu, X.-Y. Optical Probe of Charge Separation at Organic/Inorganic Semiconductor Interfaces. *J. Phys. Chem. C* **2013**, *117* (21), 10974–10979.

(95) Khalil, M.; Demirdöven, N.; Tokmakoff, A. Vibrational Coherence Transfer Characterized with Fourier-Transform 2D IR Spectroscopy. *J. Chem. Phys.* **2004**, *121* (1), 362–373.

(96) Dawlaty, J. M.; Bennett, D. I. G.; Huxter, V. M.; Fleming, G. R. Mapping the Spatial Overlap of Excitons in a Photosynthetic Complex via Coherent Nonlinear Frequency Generation. *J. Chem. Phys.* **2011**, *135* (4), 044201.

(97) Nee, M. J.; Baiz, C. R.; Anna, J. M.; McCanne, R.; Kubarych, K. J. Multilevel Vibrational Coherence Transfer and Wavepacket Dynamics Probed with Multidimensional IR Spectroscopy. *J. Chem. Phys.* **2008**, *129* (8), 084503.

(98) Shibata, Y.; Nakao, M.; Manaka, T.; Lim, E.; Iwamoto, M. Probing Electric Field Distribution in Underlayer of an Organic Double-Layer System by Optical Second-Harmonic Generation Measurement. *Jpn. J. Appl. Phys.* **2009**, *48* (2), 021504.

(99) Maia, F. C. B.; Miranda, P. B. Molecular Ordering of Conjugated Polymers at Metallic Interfaces Probed by SFG Vibrational Spectroscopy. *J. Phys. Chem. C* **2015**, 150320144559007.

(100) O'Brien, D. B.; Massari, A. M. Simulated Vibrational Sum Frequency Generation from a Multilayer Thin Film System with Two Active Interfaces. *J. Chem. Phys.* **2013**, *138* (5), 154708.

(101) Clark, J.; Silva, C.; Friend, R. H.; Spano, F. C. Role of Intermolecular Coupling in the Photophysics of Disordered Organic Semiconductors: Aggregate Emission in Regioregular Polythiophene. *Phys. Rev. Lett.* **2007**, *98* (20), 1–4.

(102) Brown, P.; Thomas, D.; Köhler, A.; Wilson, J.; Kim, J.-S.; Ramsdale, C.; Sirringhaus, H.; Friend, R. Effect of Interchain Interactions on the Absorption and Emission of Poly(3-Hexylthiophene). *Phys. Rev. B* **2003**, *67* (6), 1–16.

(103) Sirringhaus, H.; Brown, P. J.; Friend, R. H.; Nielsen, M. M.; Bechgaard, K.; Langeveld-Voss, B. M. W.; Spiering, a. J. H.; Janssen, R. a. J.; Meijer, E. W.; Herwig, P.; et al. Two-Dimensional Charge Transport in Self-Organized, High-Mobility Conjugated Polymers. *Nature* **1999**, *401* (6754), 685–688.

(104) Huang, Y.; Westenhoff, S.; Avilov, I.; Sreearunothai, P.; Hodgkiss, J. M.; Deleener, C.; Friend, R. H.; Beljonne, D. Electronic Structures of Interfacial States Formed at Polymeric Semiconductor Heterojunctions. *Nat. Mater.* **2008**, *7* (6), 483–489.

(105) Rao, A.; Chow, P. C. Y.; Gélinas, S.; Schlenker, C. W.; Li, C.-Z.; Yip, H.-L.; Jen, A. K.-Y.; Ginger, D. S.; Friend, R. H. The Role of Spin in the Kinetic Control of Recombination

in Organic Photovoltaics. *Nature* **2013**, *500* (7463), 435–439.

(106) Lakhwani, G.; Rao, A.; Friend, R. H. Bimolecular Recombination in Organic Photovoltaics. *Annu. Rev. Phys. Chem.* **2014**, *65*, 557–581.

(107) Giuliano Nicolau, B.; Garcia-Rey, N.; Dryzhakov, B.; Dlott, D. D. Interfacial Processes of a Model Lithium Ion Battery Anode Observed,\n in Situ\n , with Vibrational Sum-Frequency Generation Spectroscopy. *J. Phys. Chem. C* **2015**, 150416133018008.

(108) Raschke, M. B.; Hayashi, M.; Lin, S. H.; Shen, Y. R. Doubly-Resonant Sum-Frequency Generation Spectroscopy for Surface Studies. *Chem. Phys. Lett.* **2002**, *359* (5–6), 367–372.

(109) Ellis, J. L.; Hickstein, D. D.; Schnitzenbaumer, K. J.; Wilker, M. B.; Palm, B. B.; Jimenez, J. L.; Dukovic, G.; Kapteyn, H. C.; Murnane, M. M.; Xiong, W. Solvents Effects on Charge Transfer from Quantum Dots. *J. Am. Chem. Soc.* **2015**, *137*, 3759.

(110) Herrmann, D.; Niesar, S.; Scharsich, C.; Köhler, A.; Stutzmann, M.; Riedle, E. Role of Structural Order and Excess Energy on Ultrafast Free Charge Generation in Hybrid Polythiophene/Si Photovoltaics Probed in Real Time by Near-Infrared Broadband Transient Absorption. *J. Am. Chem. Soc.* **2011**, *133* (45), 18220–18233.

(111) Long, R.; Prezhdo, O. V. Instantaneous Generation of Charge-Separated State on TiO2 Surface Sensitized with Plasmonic Nanoparticles. *J. Am. Chem. Soc.* **2014**, *136* (11), 4343–4354.

(112) Changdeuck Bae, Thi Anh Ho, Hyunchul Kim, Seonhee Lee, Seulky Lim, Myungjun Kim, Hyunjun Yoo, Josep M. Montero-Moreno, J. H. P. and H. S. Bulk Layered Heterojunction as an Efficient Electrocatalyst for Hydrogen Evolution. *Sci. Adv.* **2017**, *3*, e1602215.

(113) Pensack, R. D.; Asbury, J. B. Beyond the Adiabatic Limit: Charge Photogeneration in Organic Photovoltaic Materials. *J. Phys. Chem. Lett.* **2010**, *1* (15), 2255–2263.

(114) Grancini, G.; Biasiucci, M.; Mastria, R.; Scotognella, F.; Tassone, F.; Polli, D.; Gigli, G.; Lanzani, G. Dynamic Microscopy Study of Ultrafast Charge Transfer in a Hybrid P3HT/Hyperbranched CdSe Nanoparticle Blend for Photovoltaics. *J. Phys. Chem. Lett.* **2012**, *3* (4), 517–523.

(115) Tseng, H.-W.; Wilker, M. B.; Damrauer, N. H.; Dukovic, G. Charge Transfer Dynamics between Photoexcited CdS Nanorods and Mononuclear Ru Water-Oxidation Catalysts. *J. Am. Chem. Soc.* **2013**, *135* (9), 3383–3386.

(116) Wu, K.; Chen, J.; Mcbride, J. R.; Lian, T. Efficient Hot-Electron Transfer by a Plasmon-Induced Interfacial Charge-Transfer Transition. *Sceince* **2015**, *3588* (2003), 3584–3588.

(117) Falke, S. M.; Rozzi, C. A.; Brida, D.; Maiuri, M.; Amato, M.; Sommer, E.; De Sio, A.; Rubio, A.; Cerullo, G.; Molinari, E.; et al. Coherent Ultrafast Charge Transfer in an Organic Photovoltaic Blend. *Science* **2014**, *344* (6187), 1001–1005.

(118) Vandewal, K.; Albrecht, S.; Hoke, E. T.; Graham, K. R.; Widmer, J.; Douglas, J. D.; Schubert, M.; Mateker, W. R.; Bloking, J. T.; Burkhard, G. F.; et al. Efficient Charge Generation by Relaxed Charge-Transfer States at Organic Interfaces. *Nat. Mater.* **2014**, *13* (1), 63–68.

(119) Xiong, W.; Laaser, J. E.; Paoprasert, P.; Franking, R. A.; Hamers, R. J.; Gopalan, P.; Zanni, M. T. Transient 2D IR Spectroscopy of Charge Injection in Dye-Sensitized Nanocrystalline Thin Films. *J. Am. Chem. Soc.* **2009**, *131*, 18040–18041.

(120) Huang, K.; Leung, L.; Lim, T.; Ning, Z.; Polanyi, J. C. Single-Electron Induces Double-Reaction by Charge Delocalization. *J. Am. Chem. Soc.* **2013**, *135* (16), 6220–6225.

(121) Zhu, H.; Song, N.; Lian, T. Wave Function Engineering for Ultrafast Charge Separation and Slow Charge Recombination in Type II Core/Shell Quantum Dots. *J. Am. Chem. Soc.* **2011**, *133* (22), 8762–8771.

(122) D.M.Kolk; Przasnyski, M.; Gerischer, H. Optical Interfacial Electron Transfer between Metal Adatoms and a Semiconductor Electrode. *Zeitschrift für Phys. Chemie Neue Folge* **1974**, *93*, 1–14.

(123) Wolf, M.; Hotzel, A.; Knoesel, E.; Velic, D. Direct and Indirect Excitation Mechanisms in Two-Photon Photoemission Spectroscopy of Cu(111) and CO/Cu (111). *Phys. Rev. B* **1999**, *59* (8), 5926–5935.

(124) Petek, H.; Petek, H. Photoexcitation of Adsorbates on Metal Surfaces : One-Step or Three-Step. *J. Chem. Phys.* **2012**, *137* (9), 091704.

(125) Han, Y.; Micha, D. A.; Kilin, D. S. Ab Initio Study of the Photocurrent at the Au/Si Metal-Semiconductor Nanointerface. *Mol. Phys.* **2015**, *113* (3–4), 327–335.

(126) Kale, M. J.; Avanesian, T.; Xin, H.; Yan, J.; Christopher, P. Controlling Catalytic Selectivity on Metal Nanoparticles by Direct Photoexcitation of Adsorbate − Metal Bonds. *Nano Lett.* **2014**, *14*, 5405.

(127) Mukherjee, S.; Libisch, F.; Large, N.; Neumann, O.; Brown, L. V.; Cheng, J.; Lassiter, J. B.; Carter, E. A.; Nordlander, P.; Halas, N. J. Hot Electrons Do the Impossible: Plasmon-Induced Dissociation of H2 on Au. *Nano Lett.* **2013**, *13* (1), 240–247.

(128) Pensack, R. D.; Banyas, K. M.; Barbour, L. W.; Hegadorn, M.; Asbury, J. B. Ultrafast Vibrational Spectroscopy of Charge-Carrier Dynamics in Organic Photovoltaic Materials. *Phys. Chem. Chem. Phys.* **2009**, *11*, 2575–2591.

(129) Nardes, A. M.; Ayzner, A. L.; Hammond, S. R.; Ferguson, A. J.; Schwartz, B. J.; Kopidakis, N. Photoinduced Charge Carrier Generation and Decay in Sequentially Deposited Polymer / Fullerene Layers : Bulk Heterojunction vs Planar Interface. *J. Phys. Chem. C* **2012**, *116*, 7293.

(130) Vilan, A.; Cahen, D.; Case, M. Chemical Modification of Semiconductor Surfaces for Molecular Electronics. *Chem. Rev.* **2017**, *117* (5), 4624.

(131) Anderson, N. A.; Lian, T. Ultrafast Electron Transfer at the Molecule-Semiconductor Nanoparticle Interface. *Annu. Rev. Phys. Chem.* **2005**, *56* (78), 491–519.

(132) Lindstrom, C. D.; Zhu, X. Photoinduced Electron Transfer at Molecule − Metal Interfaces. *Chem. Rev.* **2006**, *106*, 4281–4300.

(133) Dutton, G.; Zhu, X. Electronic Band Formation at Organic - Metal Interfaces : Role of Adsorbate - Surface Interaction. *J. Phys. Chem. B* **2001**, *105*, 10912–10917.

(134) Arnolds, H.; Bonn, M. Surface Science Reports Ultrafast Surface Vibrational Dynamics. *Surf. Sci. Rep.* **2010**, *65* (2), 45–66.

(135) Wan, Q.; Galli, G. First-Principles Framework to Compute Sum-Frequency Generation Vibrational Spectra of Semiconductors and Insulators. *Phys. Rev. Lett.* **2015**, *115* (24), 246404.

(136) Hains, A. W.; Liang, Z.; Woodhouse, M. a; Gregg, B. a. Molecular Semiconductors in Organic Photovoltaic Cells. *Chem. Rev.* **2010**, *110* (11), 6689–6735.

(137) Bhargava, K.; Singh, V. Investigation of Gold and Poly (3-Alkylthiophene) Interface in Top and Bottom Contact Structures. *Synth. Met.* **2016**, *211*, 49–57.

(138) Osikowicz, W.; de Jong, M. P.; Salaneck, W. R. Formation of the Interfacial Dipole at Organic-Organic Interfaces: C60/Polymer Interfaces. *Adv. Mater.* **2007**, *19* (23), 4213–4217.

(139) Hamadani, B. H.; Ding, H.; Gao, Y.; Natelson, D. Doping Dependent Charge Injection and Band Alignment in Organic Field-Effect Transistors. *Phys. Rev. B* **2005**, *72*, arXiv:cond-mat/0512318v1.

(140) Fahlman, M.; Crispin, A.; Crispin, X.; Henze, S. K. M.; Jong, M. P. de; Osikowicz, W.; Tengstedt, C.; Salaneck, W. R. Electronic Structure of Hybrid Interfaces for Polymer-Based Electronics. *J. Phys. Condens. Matter* **2007**, *19* (18), 183202.

(141) Tengstedt, C.; Osikowicz, W.; Salaneck, W. R.; Parker, I. D.; Hsu, C.; Fahlman, M.; Parker, I. D. Fermi-Level Pinning at Conjugated Polymer Interfaces Fermi-Level Pinning at Conjugated Polymer Interfaces. *Appl. Phys. Lett.* **2016**, *053502* (2006), 18–21.

(142) Anglin, T. C.; Sohrabpour, Z.; Massari, A. M. Nonlinear Spectroscopic Markers of Structural Change during Charge Accumulation in Organic Field-Effect Transistors. *J. Phys. Chem. C* **2011**, *115* (41), 20258–20266.

(143) Maia, F. C. B.; Miranda, P. B. Molecular Ordering of Conjugated Polymers at Metallic Interfaces Probed by SFG Vibrational Spectroscopy. *J. Phys. Chem. C* **2015**, *119*, 7386–7399.

(144) Ye, H.; Huang, J.; Park, J.-R.; Katz, H. E.; Gracias, D. H. Correlations between SFG Spectra and Electrical Properties of Organic Field Effect Transistors. *J. Phys. Chem. C* **2007**, *111* (35), 13250–13255.

(145) Miyamae, T.; Takada, N.; Tsutsui, T. Probing Buried Organic Layers in Organic Light-Emitting Diodes under Operation by Electric-Field-Induced Doubly Resonant Sum-Frequency Generation Spectroscopy. *Appl. Phys. Lett.* **2012**, *101*, 073304.

(146) Wu, X.; Park, H.; Zhu, X. Probing Transient Electric Fields in Photoexcited Organic Semiconductor Thin Films and Interfaces by Time-Resolved Second Harmonic Generation. *J. Phys. Chem. C* **2014**, *118*, 10670.

(147) Wilcox, D. E.; Sykes, M. E.; Niedringhaus, A.; Shtein, M.; Ogilvie, J. P. Heterodyne-Detected and Ultrafast Time-Resolved Second-Harmonic Generation for Sensitive Measurements of Charge Transfer. *Opt. Lett.* **2014**, *39* (14), 4274–4277.

(148) Lee, C. H.; Chang, R. K.; Bloembergen, N. Nonlinear Electroreflectance in Silicon and Silver. *Phys. Rev. Lett.* **1967**, *18* (5), 167–170.

(149) Wang, H.; Wang, H.; Gao, B.; Wang, L.; Yang, Z.; Du, X.; Chen, Q. Nanoscale Exciton Diffusion and Charge Transfer Dynamics in Nano Phase-Separated. *Nanoscale* **2011**, No. 10, 2280–2285.

(150) Shaw, P. E.; Ruseckas, A.; Samuel, I. D. Exciton Diffusion Measurements in Poly (3-Hexylthiophene). *Adv. Mater.* **2008**, *20*, 3516–3520.

(151) Goodman, A. J.; Tisdale, W. A. Enhancement of Second-Order Nonlinear-Optical Signals by Optical Stimulation. *Phys. Rev. Lett.* **2015**, *114* (18), 183902.

(152) Pandey, R.; Moon, A. P.; Bender, J. A.; Roberts, S. T. Extracting the Density of States of Copper Phthalocyanine at the SiO 2 Interface with Electronic Sum Frequency Generation. *J. Phys. Chem. Lett.* **2016**, *7*, 1060–1066.

(153) Zhu, X. Y.; White, J. M.; Wolf, M.; Hasselbrink, E.; Ertl, G. Polarization Probe of Excitation Mechanisms in Surface Photochemistry. *Chem. Phys. Lett.* **1991**, *176* (5), 459–466.

(154) Lebedev, M. V.; Misochko, O. V.; Dekorsy, T.; Georgiev, N. On the Nature of " Coherent Artifact ." *J. Exp. Theor. Phys.* **2005**, *100* (2), 272–282.

(155) Sun, C.; Vallee, F.; Acioli, L. H.; Ippen, E. P.; Fujimoto, J. G. Femtosecond-Tunable Measurement of Electron Thermalization in Gold. *Phys. Rev. B* **1994**, *50* (20), 15337.

(156) Ayzner, A. L.; Doan, S. C.; Villers, B. T. De; Schwartz, B. J. Ultrafast Studies of Exciton Migration and Polaron Formation in Sequentially Solution-Processed Conjugated Polymer/Fullerene Quasi-Bilayer Photovoltaics. *J. Phys. Chem. Lett.* **2012**, *3*, 2281.

(157) Yang, Y.; Gu, J.; Young, J. L.; Miller, E. M.; Turner, J. A.; Neale, N. R.; Beard, M. C. Semiconductor Interfacial Carrier Dynamics via Photoinduced Electric Fields. *Science (80-.).* **2015**, *350*, 6442–6447.

(158) Chung, P.; Tregidgo, C.; Suhling, K. Determining a Fluorophore's Transition Dipole Moment from Fluorescence Lifetime Measurements in Solvents of Varying Refractive Index. *Methods Appl. Fluoresc.* **2016**, *4*, 045001.

(159) Stiopkin, I. V; Jayathilake, H. D.; Bordenyuk, A. N.; Benderskii, A. V. Heterodyne-Detected Vibrational Sum Frequency Generation Spectroscopy. *J. Am. Chem. Soc.* **2008**, *130* (2), 2271–2275.

(160) Singh, P. C.; Nihonyanagi, S.; Yamaguchi, S.; Tahara, T. Ultrafast Vibrational Dynamics of Water at a Charged Interface Revealed by Two-Dimensional Heterodyne-Detected Vibrational Sum Frequency Generation. *J. Chem. Phys.* **2012**, *137* (9), 094706.

(161) Pool, R. E.; Versluis, J.; Backus, E. H. G.; Bonn, M. Comparative Study of Direct and Phase-Specific Vibrational Sum-Frequency Generation Spectroscopy: Advantages and Limitations. *J. Phys. Chem. B* **2011**, *115* (51), 15362–15369.

(162) Ji, N.; Ostroverkhov, V.; Chen, C. Y.; Shen, Y. R. Phase-Sensitive Sum-Frequency Vibrational Spectroscopy and Its Application to Studies of Interfacial Alkyl Chains. *J. Am. Chem. Soc.* **2007**, *129* (33), 10056–10057.

(163) King, E. M.; Clark, S. J.; Verdozzi, C. F.; Ackland, G. J. Interaction between Metallic p Orbitals and the π Orbitals of Organic Molecules : The Binding between Ethylene and Aluminum. *J. Phys. Chem. B* **2001**, *105* (3), 641–645.

(164) Innes, R. A.; Sambles, J. R. Optical Characterisation of Gold Using Surface Plasmon-Polaritons. *J. Phys. F Met. Phys.* **1987**, *17* (1), 277.

(165) Wang, Q.; Zakeeruddin, S. M.; Nazeeruddin, M. K.; Humphry-Baker, R.; Grätzel, M. Molecular Wiring of Nanocrystals: NCS-Enhanced Cross-Surface Charge Transfer in Self-Assembled Ru-Complex Monolayer on Mesoscopic Oxide Films. *J. Am. Chem. Soc.* **2006**, *128* (13), 4446–4452.

(166) Lee, K. J.; Xiao, Y.; Woo, J. H.; Kim, E.; Kreher, D.; Attias, A.-J.; Mathevet, F.; Ribierre, J.-C.; Wu, J. W.; André, P. Charge-Transfer Dynamics and Nonlocal Dielectric Permittivity Tuned with Metamaterial Structures as Solvent Analogues. *Nat. Mater.* **2017**.

(167) Bakulin, A. A.; Zapunidy, S. A.; Pshenichnikov, M. S.; van Loosdrecht, P. H. M.; Paraschuk, D. Y. Efficient Two-Step Photogeneration of Long-Lived Charges in Ground-State Charge-Transfer Complexes of Conjugated Polymer Doped with Fullerene. *Phys. Chem. Chem. Phys.* **2009**, *11* (33), 7324.

(168) Bakulin, A. A.; Martyanov, D. S.; Paraschuk, D. Y.; Pshenichnikov, M. S.; van Loosdrecht, P. H. Ultrafast Charge Photogeneration Dynamics in Ground-State Charge-Transfer Complexes Based on Conjugated Polymers. *J. Phys. Chem. B* **2008**, *112* (44), 13730–13737.

(169) Wu, K.; Chen, J.; McBride, J. R.; Lian, T. Efficient Hot-Electron Transfer by a Plasmon-Induced Interfacial Charge-Transfer Transition. *Science (80-.).* **2015**, *349* (6248), 632–635.

(170) Falke, S. M.; Rozzi, C. A.; Brida, D.; Maiuri, M.; Amato, M.; Sommer, E.; De Sio, A.; Rubio, A.; Cerullo, G.; Molinari, E.; et al. Coherent Ultrafast Charge Transfer in an Organic Photovoltaic Blend. *Science (80-.).* **2014**, *344* (6187), 1001–1005.

(171) Zhu, H.; Wang, J.; Gong, Z.; Kim, Y. D.; Hone, J.; Zhu, X. Y. Interfacial Charge Transfer Circumventing Momentum Mismatch at Two-Dimensional van Der Waals Heterojunctions. *Nano Lett.* **2017**, *17* (6), 3591–3598.

(172) Li, Y.; Wang, J.; Xiong, W. Probing Electronic Structures of Organic Semiconductors at Buried Interfaces by Electronic Sum Frequency Generation Spectroscopy. *J. Phys. Chem. C* **2015**, *119* (50), 28083–28089.

(173) Yagi, I.; Inokuma, K.; Kimijima, K.; Notsu, H. Molecular Structure of Buried Perfluorosulfonated Ionomer/Pt Interface Probed by Vibrational Sum Frequency Generation Spectroscopy. *J. Phys. Chem. C* **2014**, *118* (45), 26182–26190.

(174) Vanselous, H.; Petersen, P. B. Extending the Capabilities of Heterodyne-Detected Sum-Frequency Generation Spectroscopy: Probing Any Interface in Any Polarization Combination. *J. Phys. Chem. C* **2016**, *120* (15), 8175–8184.

(175) Xiang, B.; Li, Y.; Pham, C. H.; Paesani, F.; Xiong, W. Ultrafast Direct Electron Transfer at Organic Semiconductor and Metal Interfaces. *Sci. Adv.* **2017**, *3*, e1701508.

(176) Gragson, D. E.; McCarty, B. M.; Richmond, G. L. Ordering of Interfacial Water Molecules at the Charged Air/Water Interface Observed by Vibrational Sum Frequency Generation. *J. Am. Chem. Soc.* **1997**, *119* (26), 6144–6152.

(177) Nihonyanagi, S.; Ishiyama, T.; Lee, T.; Yamaguchi, S.; Bonn, M.; Morita, A.; Tahara, T. Unified Molecular View of the Air / Water Interface Based on Experimental and Theoretical χ (2) Spectra of an Isotopically Diluted Water Surface. *J. Am. Chem. Soc.* **2011**, *133* (2), 16875–16880.

(178) Chen, X.; Hua, W.; Huang, Z.; Allen, H. C. Interfacial Water Structure Associated with Phospholipid Membranes Studied by Phase-Sensitive Vibrational Sum Frequency Generation Spectroscopy. *J. Am. Chem. Soc.* **2010**, *132* (17), 11336–11342.

(179) Darlington, A. M.; Jarisz, T. A.; Dewalt-Kerian, E. L.; Roy, S.; Kim, S.; Azam, M. S.; Hore, D. K.; Gibbs, J. M. Separating the PH-Dependent Behavior of Water in the Stern and Diffuse Layers with Varying Salt Concentration. *J. Phys. Chem. C* **2017**, *121* (37), 20229–20241.

(180) Wen, Y.-C.; Zha, S.; Liu, X.; Yang, S.; Guo, P.; Shi, G.; Fang, H.; Shen, Y. R.; Tian, C. Unveiling Microscopic Structures of Charged Water Interfaces by Surface-Specific Vibrational Spectroscopy. *Phys. Rev. Lett.* **2016**, *116* (1), 016101.

(181) Doğangün, M.; Ohno, P. E.; Liang, D.; McGeachy, A. C.; Bé, A. G.; Dalchand, N.; Li, T.; Cui, Q.; Geiger, F. M. Hydrogen-Bond Networks near Supported Lipid Bilayers from Vibrational Sum Frequency Generation Experiments and Atomistic Simulations. *J. Phys. Chem. B* **2018**, *122* (18), 4870–4879.

(182) Ohno, P. E.; Wang, H. F.; Paesani, F.; Skinner, J. L.; Geiger, F. M. Second-Order Vibrational Lineshapes from the Air/Water Interface. *J. Phys. Chem. A* **2018**, *122* (18), 4457–4464.

(183) Reddy, S. K.; Thiraux, R.; Wellen Rudd, B. A.; Lin, L.; Adel, T.; Joutsuka, T.; Geiger, F. M.; Allen, H. C.; Morita, A.; Paesani, F. Bulk Contributions Modulate the Sum-Frequency Generation Spectra of Water on Model Sea-Spray Aerosols. *Chem* **2018**, *4* (7), 1629–1644.

(184) Roy, S.; Beutier, C.; Hore, D. K. Combined IR-Raman vs Vibrational Sum-Frequency Heterospectral Correlation Spectroscopy. *J. Mol. Struct.* **2018**, *1161*, 403–411.

(185) Pezzotti, S.; Galimberti, D. R.; Shen, Y. R.; Gaigeot, M. P. Structural Definition of the BIL and DL: A New Universal Methodology to Rationalize Non-Linear χ(2)(ω) SFG Signals at Charged Interfaces, Including χ(3)(ω) Contributions. *Phys. Chem. Chem. Phys.* **2018**, *20*, 5190–5199.

(186) Joutsuka, T.; Morita, A. Electrolyte and Temperature Effects on Third-Order Susceptibility in Sum Frequency Generation Spectroscopy of Aqueous Salt Solutions. *J. Phys. Chem. C* **2018**, *122* (2), 11407–11413.

(187) Nihonyanagi, S.; Singh, P. C.; Yamaguchi, S.; Tahara, T. Ultrafast Vibrational Dynamics of a Charged Aqueous Interface by Femtosecond Time-Resolved Heterodyne-Detected Vibrational Sum Frequency Generation. *Bull. Chem. Soc. Jpn.* **2012**, *85* (7), 758–760.

(188) Matsuzaki, K.; Kusaka, R.; Nihonyanagi, S.; Yamaguchi, S.; Nagata, T.; Tahara, T. Partially Hydrated Electrons at the Air/Water Interface Observed by UV-Excited Time-Resolved Heterodyne-Detected Vibrational Sum Frequency Generation Spectroscopy. *J. Am. Chem. Soc.* **2016**, *138* (24), 7551–7557.

(189) Rich, C. C.; Lindberg, K. A.; Krummel, A. T. Phase Acrobatics: The Influence of Excitonic Resonance and Gold Nonresonant Background on Heterodyne-Detected Vibrational Sum Frequency Generation Emission. *J. Phys. Chem. Lett.* **2017**, *8* (7), 1331–1337.

(190) Wang, H.; Gao, T.; Xiong, W. Self-Phase-Stabilized Heterodyne Vibrational Sum Frequency Generation Microscopy. *ACS Photonics* **2017**, *4*, 1839–1845.

(191) Kannurpatti, A. R.; Anseth, J. W.; Bowman, C. N. A Study of the Evolution of Mechanical Properties and Structural Heterogeneity of Polymer Networks Formed by Photopolymerizations of Multifunctional (Meth)Acrylates. *Polymer (Guildf).* **1998**, *39* (12), 2507–2513.

(192) Pingel, P.; Zen, A.; Abellón, R. D.; Grozema, F. C.; Siebbeles, L. D. A.; Neher, D. Temperature-Resolved Local and Macroscopic Charge Carrier Transport in Thin P3HT Layers. *Adv. Funct. Mater.* **2010**, *20* (14), 2286–2295.

(193) Yang, W.; Hore, D. K. Determining the Orientation of Chemical Functional Groups on Metal Surfaces by a Combination of Homodyne and Heterodyne Nonlinear Vibrational Spectroscopy. *J. Phys. Chem. C* **2017**, *121* (50), 28043–28050.

(194) Snellenburg, J. J.; Laptenok, S. P.; Seger, R.; Mullen, K. M.; Stokkum, I. H. M. van. Glotaran : A Java -Based Graphical User Interface for the R Package TIMP. *J. Stat. Softw.* **2012**, *49* (3), 1–22.

(195) Hamm, P.; Zanni, M. *Concepts and Methods of 2D Infrared Spectroscopy*; Cambridge University Press: Cambridge, U.K., 2011.

(196) Anna, J. M.; Kubarych, K. J. Watching Solvent Friction Impede Ultrafast Barrier Crossings: A Direct Test of Kramers Theory. *J. Chem. Phys.* **2010**, *133* (17).

(197) Kumar, B.; Llorente, M.; Froehlich, J.; Dang, T.; Sathrum, A.; Kubiak, C. P. Photochemical and Photoelectrochemical Reduction of CO2. *Annu. Rev. Phys. Chem.* **2012**, *63*, 541–569.

(198) Galperin, M.; Nitzan, A. Molecular Optoelectronics: The Interaction of Molecular Conduction Junctions with Light. *Phys. Chem. Chem. Phys.* 2012, pp 9421–9438.

(199) Millan, K. M.; Mikkelsen, S. R. Sequence-Selective Biosensor for DNA Based on Electroactive Hybridization Indicators. *Anal. Chem.* **1993**, *65* (17), 2317–2323.

(200) Laaser, J. E.; Skoff, D. R.; Ho, J. J.; Joo, Y.; Serrano, A. L.; Steinkruger, J. D.; Gopalan, P.; Gellman, S. H.; Zanni, M. T. Two-Dimensional Sum-Frequency Generation Reveals Structure and Dynamics of a Surface-Bound Peptide. *J. Am. Chem. Soc.* **2014**, *136*, 956–962.

(201) Zhang, Z.; Piatkowski, L.; Bakker, H. J.; Bonn, M. Communication: Interfacial Water Structure Revealed by Ultrafast Two-Dimensional Surface Vibrational Spectroscopy. *J. Chem. Phys.* **2011**, *135*, 021101.

(202) Clark, M. L.; Rudshteyn, B.; Ge, A.; Chabolla, S. A.; Machan, C. W.; Psciuk, B. T.; Song, J.; Canzi, G.; Lian, T.; Batista, V. S.; et al. Orientation of Cyano-Substituted Bipyridine Re(I) Fac -Tricarbonyl Electrocatalysts Bound to Conducting Au Surfaces. *J. Phys. Chem. C* **2016**, acs.jpcc.5b10912.

(203) Wolfseder, B.; Seidner, L.; Domcke, W.; Stock, G.; Seel, M.; Engleitner, S.; Zinth, W. Vibrational Coherence in Ultrafast Electron-Transfer Dynamics of Oxazine 1 in N,N-Dimethylaniline: Simulation of a Femtosecond Pump-Probe Experiment. *Chem. Phys.* **1998**, *233* (2–3), 323–334.

(204) Chudoba, C.; Riedle, E.; Pfeiffer, M.; Elsaesser, T. Vibrational Coherence in Ultrafast Excited State Proton Transfer. *Chem. Phys. Lett.* **1996**, *263* (5), 622–628.

(205) Kiefer, L. M.; King, J. T.; Kubarych, K. J. Dynamics of Rhenium Photocatalysts Revealed through Ultrafast Multidimensional Spectroscopy. *Acc. Chem. Res.* **2015**, *48* (4), 1123–1130.

(206) Bredenbeck, J.; Helbing, J.; Hamm, P. Labeling Vibrations by Light: Ultrafast Transient 2D-IR Spectroscopy Tracks Vibrational Modes during Photoinduced Charge Transfer. *J. Am. Chem. Soc.* **2004**, *126* (4), 990–991.

(207) Ricks, A. M.; Anfuso, C. L.; Rodríguez-Córdoba, W.; Lian, T. Vibrational Relaxation Dynamics of Catalysts on TiO2 Rutile (110) Single Crystal Surfaces and Anatase Nanoporous Thin Films. *Chem. Phys.* **2013**, *422*, 264–271.

(208) Rosenfeld, D. E.; Gengeliczki, Z.; Smith, B. J.; Stack, T. D. P.; Fayer, M. D. Structural Dynamics of a Catalytic Monolayer Probed by Ultrafast 2D IR Vibrational Echoes. *Science (80-.).* **2011**, *334*, 634–639.

(209) Li, H.; Bristow, A. D.; Siemens, M. E.; Moody, G.; Cundiff, S. T. Unraveling Quantum Pathways Using Optical 3D Fourier-Transform Spectroscopy. *Nat. Commun.* **2013**, *4*, 1390.

(210) Ding, F.; Zanni, M. T. Heterodyned 3D IR Spectroscopy. *Chem. Phys.* **2007**, *341* (1–3), 95–105.

(211) Fulmer, E. C.; Mukherjee, P.; Krummel, A. T.; Zanni, M. T. A Pulse Sequence for Directly Measuring the Anharmonicities of Coupled Vibrations: Two-Quantum Two-Dimensional Infrared Spectroscopy. *J. Chem. Phys.* **2004**, *120* (17), 8067–8078.

(212) Garrett-Roe, S.; Perakis, F.; Rao, F.; Hamm, P. Three-Dimensional Infrared Spectroscopy of Isotope-Substituted Liquid Water Reveals Heterogeneous Dynamics. *J. Phys. Chem. B* **2011**, *115* (21), 6976–6984.

(213) Turner, D. B.; Stone, K. W.; Gundogdu, K.; Nelson, K. A. Three-Dimensional Electronic Spectroscopy of Excitons in GaAs Quantum Wells. *J. Chem. Phys.* **2009**, *131* (14).

(214) Garrett-Roe, S.; Hamm, P. Purely Absorptive Three-Dimensional Infrared Spectroscopy. *J. Chem. Phys.* **2009**, *130* (16).

(215) Wong, C. Y.; Scholes, G. D. Biexcitonic Fine Structure of CdSe Nanocrystals Probed by Polarization-Dependent Two-Dimensional Photon Echo Spectroscopy. *J. Phys. Chem. A* **2011**, *115* (16), 3797–3806.

(216) Cheng, Y.-C.; Fleming, G. R. Coherence Quantum Beats in Two-Dimensional Electronic Spectroscopy. *J. Phys. Chem. A* **2008**, *112* (18), 4254–4260.

(217) Tokmakoff, A. Two-Dimensional Line Shapes Derived from Coherent Third-Order Nonlinear Spectroscopy. *J. Phys. Chem. A* **2000**, *104* (18), 4247–4255.

(218) Persson, B. N. J. Damping of Excited Molecules Located Above A Metal Surface. *Solid State Commun.* **1978**, *27*, 417–421.

(219) Roeterdink, W. G.; Berg, O.; Bonn, M. Frequency-and Time-Domain Femtosecond Vibrational Sum Frequency Generation from CO Adsorbed on Pt(111). *J. Chem. Phys.* **2004**, *121* (20), 10174–10180.

(220) Ueba, H. Vibrational RELAXATION AND PUMP-PROBE SPECTROSCOPIES OF ADSORBATES ON SOLID SURFACES. *Prog. Surf. Sci.* **1997**, *55* (2), 115–179.

(221) Tully, J. C. Chemical Dynamics at Metal Surfaces. *Annu. Rev. Phys. Chem.* **2000**, *51*, 153–178.

(222) Rosenfeld, D. E.; Nishida, J.; Yan, C.; Gengeliczki, Z.; Smith, B. J.; Fayer, M. D. Dynamics of Functionalized Surface Molecular Monolayers Studied with Ultrafast

Infrared Vibrational Spectroscopy. *J. Phys. Chem. C* **2012**, *116* (44), 23428–23440.

(223) Ueba, H. Vibrational Lineshapes of Adsorbates on Solid Surfaces. *Prog. Surf. Sci.* **1986**, *22* (3), 181–321.

(224) Cochran, R. E.; Ryder, O. S.; Grassian, V. H.; Prather, K. A. Sea Spray Aerosol: The Chemical Link between the Oceans, Atmosphere, and Climate. *Acc. Chem. Res.* **2017**, *50* (3), 599–604.

(225) Estillore, A. D.; Trueblood, J. V.; Grassian, V. H. Atmospheric Chemistry of Bioaerosols: Heterogeneous and Multiphase Reactions with Atmospheric Oxidants and Other Trace Gases. *Chem. Sci.* **2016**, *7* (11), 6604–6616.

(226) Hawkins, L. N.; Russell, L. M. Polysaccharides, Proteins, and Phytoplankton Fragments: Four Chemically Distinct Types of Marine Primary Organic Aerosol Classified by Single Particle Spectromicroscopy. *Adv. Meteorol.* **2010**, *2010*.

(227) Quinn, P. K.; Collins, D. B.; Grassian, V. H.; Prather, K. A.; Bates, T. S. Chemistry and Related Properties of Freshly Emitted Sea Spray Aerosol. *Chem. Rev.* **2015**, *115* (10), 4383–4399.

(228) Schiffer, J. M.; Luo, M.; Dommer, A. C.; Thoron, G.; Pendergraft, M.; Santander, M. V.; Lucero, D.; Pecora De Barros, E.; Prather, K. A.; Grassian, V. H.; et al. Impacts of Lipase Enzyme on the Surface Properties of Marine Aerosols. *J. Phys. Chem. Lett.* **2018**, *9* (14), 3839–3849.

(229) Lee, C.; Sultana, C. M.; Collins, D. B.; Santander, M. V.; Axson, J. L.; Malfatti, F.; Cornwell, G. C.; Grandquist, J. R.; Deane, G. B.; Stokes, M. D.; et al. Advancing Model Systems for Fundamental Laboratory Studies of Sea Spray Aerosol Using the Microbial Loop. *J. Phys. Chem. A* **2015**, *119* (33), 8860–8870.

(230) Engelhardt, K.; Rumpel, A.; Walter, J.; Dombrowski, J.; Kulozik, U.; Braunschweig, B.; Peukert, W. Protein Adsorption at the Electrified Air-Water Interface: Implications on Foam Stability. *Langmuir* **2012**, *28* (20), 7780–7787.

(231) Jiang, Q.; Chiew, Y. C. Dynamics of Adsorption and Desorption of Proteins at an Air/Water Interface. *Colloids Surfaces B Biointerfaces* **2001**, *20* (4), 303–308.

(232) Xu, L.-C.; Bauer, J. W.; Siedlecki, C. A. Proteins, Platelets, and Blood Coagulation at Biomaterial Interfaces. *Colloids Surfaces B Biointerfaces* **2014**, *124*, 49–68.

(233) Kuznetsova, M.; Lee, C. Dissolved Free and Combined Amino Acids in Nearshore Seawater, Sea Surface Microlayers and Foams: Influence of Extracellular Hydrolysis. *Aquat. Sci.* **2002**, *64* (3), 252–268.

(234) Graham, D. E.; Phillips, M. C. Proteins at Liquid Interfaces II. Adsorption Isotherms. *J. Colloid Interface Sci.* **1979**, *70* (3), 415–426.

(235) Cunliffe, M.; Engel, A.; Frka, S.; Gašparović, B. Ž.; Guitart, C.; Murrell, J. C.; Salter, M.; Stolle, C.; Upstill-Goddard, R.; Wurl, O. Sea Surface Microlayers: A Unified

Physicochemical and Biological Perspective of the Air-Ocean Interface. *Prog. Oceanogr.* **2013**, *109*, 104–116.

(236) van Pinxteren, M.; Müller, C.; Iinuma, Y.; Stolle, C.; Herrmann, H. Chemical Characterization of Dissolved Organic Compounds from Coastal Sea Surface Microlayers (Baltic Sea, Germany). *Environ. Sci. Technol.* **2012**, *46* (19), 10455–10462.

(237) Wang, J.; Buck, S. M.; Chen, Z. Sum Frequency Generation Vibrational Spectroscopy Studies on Protein Adsorption. *J. Phys. Chem. B* **2002**, *106* (44), 11666–11672.

(238) Wang, J.; Buck, S. M.; Chen, Z. The Effect of Surface Coverage on Conformation Changes of Bovine Serum Albumin Molecules at the Air-Solution Interface Detected by Sum Frequency Generation Vibrational Spectroscopy. *Analyst* **2003**, *128*, 773–778.

(239) Wang, J.; Even, M. A.; Chen, X.; Schmaier, A. H.; Waite, J. H.; Chen, Z. Detection of Amide I Signals of Interfacial Proteins in Situ Using SFG. **2003**, 9914–9915.

(240) Yan, E. C. Y.; Fu, L.; Wang, Z.; Liu, W. Biological Macromolecules at Interfaces Probed by Chiral Vibrational Sum Frequency Generation Spectroscopy. *Chem. Rev.* **2014**, *114*, 8471–8498.

(241) Zhang, Y.; Cremer, P. S. Chemistry of Hofmeister Anions and Osmolytes. *Annu. Rev. Phys. Chem.* **2010**, *61*, 63–83.

(242) Baldwin, R. L. How Hofmeister Ion Interactions Affect Protein Stability. *Biophys. J.* **1996**, *71* (4), 2056–2063.

(243) Zhang, Y.; Cremer, P. S. The Inverse and Direct Hofmeister Series for Lysozyme. *Proc. Natl. Acad. Sci.* **2009**, *106* (36), 15249–15253.

(244) Gurau, M. C.; Lim, S. M.; Castellana, E. T.; Albertorio, F.; Kataoka, S.; Cremer, P. S. On the Mechanism of the Hofmeister Effect. *J. Am. Chem. Soc.* **2004**, *126* (34), 10522–10523.

(245) Chi, E. Y.; Krishnan, S.; Randolph, T. W.; Carpenter, J. F. Physical Stability of Proteins in Aqueous Solution: Mechanism and Driving Forces in Nonnative Protein Aggregation. *Pharmaceutical Research*. 2003, pp 1325–1336.

(246) Doyle, A. W.; Fick, J.; Himmelhaus, M.; Eck, W.; Graziani, I.; Prudovsky, I.; Grunze, M.; Maciag, T.; Neivandt, D. J. Protein Deformation of Lipid Hybrid Bilayer Membranes Studied by Sum Frequency Generation Vibrational Spectroscopy. *Langmuir* **2004**, *20* (21), 8961–8965.

(247) Shrestha, M.; Luo, M.; Li, Y.; Xiang, B.; Xiong, W.; Grassian, V. H. Let There Be Light: Stability of Palmitic Acid Monolayers at the Air/Salt Water Interface in the Presence and Absence of Simulated Solar Light and a Photosensitizer†. *Chem. Sci.* **2018**, *9*, 5716–5723.

(248) Maruyama, T.; Katoh, S.; Nakajima, M.; Nabetani, H.; Abbott, T. P.; Shono, A.; Satoh, K. FT-IR Analysis of BSA Fouled on Ultrafiltration and Microfiltration Membranes. *J. Memb. Sci.* **2001**, *192*, 201–207.

(249) Servagent-Noinville, S.; Revault, M.; Quiquampoix, H.; Baron, M. H. Conformational Changes of Bovine Serum Albumin Induced by Adsorption on Different Clay Surfaces: FTIR Analysis. *J. Colloid Interface Sci.* **2000**, *221* (2), 273–283.

(250) Urashima, S.; Myalitsin, A.; Nihonyanagi, S.; Tahara, T. The Topmost Water Structure at a Charged Silica/Aqueous Interface Revealed by Heterodyne-Detected Vibrational Sum Frequency Generation Spectroscopy. *J. Phys. Chem. Lett.* **2018**, *9*, 4109–4114.

(251) Joutsuka, T.; Hirano, T.; Sprik, M.; Morita, A. Effects of Third-Order Susceptibility in Sum Frequency Generation Spectra: A Molecular Dynamics Study in Liquid Water. *Phys. Chem. Chem. Phys.* **2018**, *20* (5), 3040–3053.

(252) DeWalt-Kerian, E. L.; Kim, S.; Azam, M. S.; Zeng, H.; Liu, Q.; Gibbs, J. M. PH-Dependent Inversion of Hofmeister Trends in the Water Structure of the Electrical Double Layer. *J. Phys. Chem. Lett.* **2017**, *8* (13), 2855–2861.

(253) Nihonyanagi, S.; Yamaguchi, S.; Tahara, T. Ultrafast Dynamics at Water Interfaces Studied by Vibrational Sum Frequency Generation Spectroscopy. *Chem. Rev.* **2017**, *117* (16), 10665–10693.

(254) Wang, Y.; Du, X.; Guo, L.; Liu, H. Chain Orientation and Headgroup Structure in Langmuir Monolayers of Stearic Acid and Metal Stearate (Ag, Co, Zn, and Pb) Studied by Infrared Reflection-Absorption Spectroscopy. *J. Chem. Phys.* **2006**, *124* (13), 134706.

(255) Cho, D.; Narsimhan, G.; Franses, E. I. Adsorption Dynamics of Native and Pentylated Bovine Serum Albumin at Air – Water Interfaces : Surface Concentration / Surface Pressure Measurements. *J. Colloid Interface Sci.* **1997**, *191*, 312–325.

(256) Tripp, B. C.; Magda, J. J.; Andrade, J. D. Adsorption of Globular Proteins at the Air/Water Interface as Measured via Dynamic Surface Tension: Concentration Dependence, Mass-Transfer Considerations, and Adsorption Kinetics. *J. Colloid Interface Sci.* **1995**, *173*, 16–27.

(257) Arakawa, T.; Timasheff, S. N. Mechanism of Protein Salting In and Salting Out by Divalent Cation Salts: Balance between Hydration and Salt Binding. *Biochemistry* **1984**, *23* (25), 5912–5923.

(258) Zangi, R. Can Salting-In / Salting-Out Ions Be Classified as Chaotropes / Kosmotropes ? *J. Phys. Chem. B* **2010**, *114*, 643–650.

(259) Hyde, A. M.; Zultanski, S. L.; Waldman, J. H.; Zhong, Y. L.; Shevlin, M.; Peng, F. General Principles and Strategies for Salting-Out Informed by the Hofmeister Series. *Org. Process Res. Dev.* **2017**, *21* (9), 1355–1370.

(260) Yano, Y. F. Kinetics of Protein Unfolding at Interfaces. *J. Phys. Condens. Matter* **2012**, *24*, 503101.

(261) Zheng, D.; Lu, L.; Li, Y.; Kelly, K. F.; Baldelli, S. Compressive Broad-Band Hyperspectral Sum Frequency Generation Microscopy to Study Functionalized Surfaces. *J. Phys. Chem. Lett.* **2016**, *7*, 1781–1787.

(262) Jang, J. H.; Jacob, J.; Santos, G.; Lee, T. R.; Baldelli, S. Image Contrast in Sum Frequency Generation Microscopy Based on Monolayer Order and Coverage. *J. Phys. Chem. C* **2013**, *117*, 15192–15202.

(263) Hirakis, S. P.; Malmstrom, R. D.; Amaro, R. E. Molecular Simulations Reveal an Unresolved Conformation of the Type IA Protein Kinase A Regulatory Subunit and Suggest Its Role in the CAMP Regulatory Mechanism. *Biochemistry* **2017**, *56* (30), 3885–3888.

(264) Chuang, S.-Y.; Chen, H.-L.; Lee, W.-H.; Huang, Y.-C.; Su, W.-F.; Jen, W.-M.; Chen, C.-W. Regioregularity Effects in the Chain Orientation and Optical Anisotropy of Composite Polymer/Fullerene Films for High-Efficiency, Large-Area Organic Solar Cells. *J. Mater. Chem.* **2009**, *19* (31), 5554.

(265) Johnson, P. B.; Christy, R. W. Optical Constants of the Noble Metals. *Phys. Rev. B* **1972**, *6* (12), 4370–4379.

(266) Mark, J. E. *Physical Properties of Polymers Handbook*; 2007; Vol. 51.

(267) Clark, M. L.; Rudshtegyn, B.; Ge, A.; Chabolla, S. A.; Machan, C. W.; Psciuk, B. T.; Song, J.; Canzi, G.; Lian, T.; Batista, V. S.; et al. Surface Orientation of Immobilized Cyano-Substituted Bipyridine Re(I) Fac -Tricarbonyl Electrocatalysts on Au Surfaces.

(268) Nogues, C.; Wanunu, M. A Rapid Approach to Reproducible, Atomically Flat Gold Films on Mica. *Surf. Sci.* **2004**, *573* (3).

(269) Xiong, W.; Laaser, J. E.; Mehlenbacher, R. D.; Zanni, M. T. Adding a Dimension to the Infrared Spectra of Interfaces Using Heterodyne Detected 2D Sum- Frequency Generation (HD 2D SFG) Spectroscopy. **2011**.

(270) Shim, S.-H.; Zanni, M. T. How to Turn Your Pump-Probe Instrument into a Multidimensional Spectrometer: 2D IR and Vis Spectroscopies via Pulse Shaping. *Phys. Chem. Chem. Phys.* **2009**, *11*, 748–761.

(271) Shim, S.-H.; Strasfeld, D. B.; Fulmer, E. C.; Zanni, M. T. Femtosecond Pulse Shaping Directly in the Mid-IR Using Acousto-Optic Modulation. *Opt. Lett.* **2006**, *31* (6), 838.